Dynamics, Acoustics and Control of Cloud Cavitation on Hydrofoils

Thesis by

Garrett E. Reisman

In Partial Fulfillment of the Requirements

for the Degree of

Doctor of Philosophy

California Institute of Technology

Pasadena, California

1997

(Submitted September 24, 1996)

Dedication

This work is dedicated to Christopher Brennen and Gerard VanderVoort, the two best teachers I have ever known.

Acknowledgements

"From time to time little men will come along to find fault with what you have done...they will go down the stream like bubbles, they will vanish; but the work you have done will remain for the ages."
Theodore Roosevelt, addressing the engineers who built the Panama Canal

This work would not have been possible without the support of a large number of people. First and foremost, I wish to thank my advisor, Dr. Brennen, for teaching me not only everything I know about cavitation, but also for teaching me a great deal about life in general. I will continue to cherish his friendship and guidance as we press on toward new adventures.

I am very grateful for the assistance of those graduate students who contributed to this work. My experiments were made possible by Doug Hart and Beth McKenney who paved the way. The numerical work performed by Jack Wang provided a very welcome complement to my experiments, and I am very appreciative of his efforts. Mark Duttweiler was essential to the completion of the air injection experiments. Fabrizio d'Auria, Roberto Zenit, Tricia Waniewski and Frank Liu all volunteered their time selflessly during critical phases of my experiments. Sudipto Sur, Michiel VanNieuwstadt and Bob Behnken also displayed tremendous patience while providing technical help. The assistance provided by undergraduates Don Kwak, Amy Herr and Amir Alagheband is also appreciated.

A debt is owed to many for their technical and administrative support, especially John Van Deusen and Rodney Rojas who were essential to the fabrication of the NACA 0021 foil. I would also like to thank Hai Vu, Joe Fontana, Rich Eastvedt, Cecilia Lin, Jackie Beard, and Dana Young.

The support of Dr. Rood and the Office of Naval Research under grant number N00014-91-J-1295, is also greatly appreciated. I would also like to thank the members of my thesis committee, Dr. Gharib, Dr. Colonius and especially Dr. Acosta for whom I have a great deal of respect and admiration.

I am very grateful to Robert, Sheila and Lainie Reisman for being such an extremely supportive family. Carl Fischer, a valued friend and mentor, deserves recognition for convincing me to pursue graduate engineering studies. Carl Wassgren also deserves special recognition for helping me survive the candidacy examination process. Finally, although all the friends who made my stay at Caltech so enjoyable and fulfilling are too numerous to list here, I would especially like to thank Kevin Condroski, Yan Kuhn de Chizelle and Simone Francis.

Abstract

Cloud cavitation, often formed by the breakdown and collapse of a sheet or vortex cavity, is responsible for severe cavitation noise and erosion damage. This thesis describes an experimental investigation of the dynamics and acoustics of cloud cavitation on a three dimensional hydrofoil and examines the injection of air as a means of noise suppression.

Part one of this work examines the large amplitude impulsive pressures which were measured on the suction surface of an oscillating hydrofoil experiencing cloud cavitation, and these pressure pulses are correlated with the observation of shock waves propagating through the bubbly mixture. Recess mounted transducers were used to measure unsteady pressures at four locations along the chord of the suction surface of a hydrofoil. By examining the transducer output, two distinct types of pressure pulses were identified. *Local* pulses occurred at a single transducer location and were randomly distributed in position and time. Conversely, *global* pulses were registered by all the transducers almost simultaneously. The location of the global pulses relative to the foil oscillation was quite repeatable and these events produced substantial far-field noise. Correlation of the transducer output with high speed movies of the cavitation revealed that the global pulses were produced by a large scale collapse of the bubble cloud. Conversely, local pulses were generated by local disturbances in the bubbly mixture characterized by large changes in void fraction.

The large pressure pulse associated with the local and global cavitation structures, the geometric coherence of their boundaries and the nearly discrete change in void fraction across the boundaries of these structures indicate that these structures consist of bubbly shock waves. Qualitative and quantitative comparisons between the current

experiments and the numerical, analytic and experimental bubbly shock wave analysis of other investigators support this conclusion.

Part two of this work examines the dramatic reduction in cloud cavitation noise due to both continuous and pulsed injection of air into the cavitating region of the foil. At sufficient air flow rates, the radiated noise could be reduced by a factor greater than 200 relative to the noise produced without air injection. Unsteady surface pressure measurements also showed a reduction in the acoustic impulse with air injection by a factor of up to two orders of magnitude. An explanation for this noise reduction can be found by examining the high speed motion pictures. The presence of the non-condensible gas in the cavitation cloud is shown to prevent any rapid or coherent collapse process. Although the formation of local structures is still observed, the presence of air in the bubbles diminishes both the magnitude and the frequency of occurrence of local pressure pulses. Finally, pulsed air injection results in a lower acoustic impulse than the impulse obtained by injecting the same mass of air continuously over the entire oscillation cycle.

Contents

List of Figures

Nomenclature

A	Radius of the bubble cloud
A_0	Initial radius of the bubble cloud
c	Chord length of foil, m
C_p	Pressure coefficient, $(p - p_0)/\frac{1}{2}\rho U^2$
$C_{p\infty}$	Pressure coefficient at infinity, $(p_\infty - p_0)/\frac{1}{2}\rho U^2$
C_{pmin}	Minimum pressure coefficient at infinity
D	Reference body size
I	Acoustic impulse, $kPa \cdot s$
I^*	Dimensionless acoustic impulse
k	Reduced frequency, $\omega c/2U$
p	Test section absolute pressure, Pa
p_0	Upstream reference pressure, Pa
p_a	Radiated acoustic pressure, Pa
p_A	Acoustic pressure intensity, Pa
p_v	Vapor pressure of water, Pa
p_∞	Pressure at infinity, Pa
q	Normalized air flow rate $= Q/Ucs$
Q	Volume flow rate of air at test section pressure and temperature, m^3/sec
$\mathcal{R}$	Distance between noise source and sensor location, m
r	Dimensionless Eulerian radial coordinate
R	Bubble radius
R_0	Initial radius of the bubble or cavitation nucleus
s	Span of foil, m

S	Surface tension of the liquid
t	Time, s
t^*	Dimensionless time
t_p	Duration of low pressure perturbation
t_r	Running time of air injection experiments, s
T	Period of foil oscillation, s
u	Dimensionless radial velocity of fluid
U	Tunnel test section velocity, m/s
V	Volume of cavitation bubble or cloud, m^3
V_{bmax}	Maximum total volume of bubbles in the cloud
x	Dimensionless axial coordinate, X/R_0
α	Void fraction of the bubbly mixture
α_0	Initial void fraction of the bubbly mixture
α_f	Instantaneous angle of attack of foil, deg
$\overline{\alpha_f}$	Mean angle of attack of foil, deg
β	Cloud interaction parameter, $\alpha_0(1-\alpha_0)A_0^2/R_0^2$
ρ	Fluid density, kg/m^3
σ	Cavitation number, $(p-p_v)/\frac{1}{2}\rho U^2$
κ	Polytropic index for gas in bubble
μ_e	Effective dynamic viscosity of the liquid
ν	Kinematic viscosity of the liquid
ω	Foil oscillation frequency, rad/s
ω_n	Natural frequency of single bubbles
ω_r	Helmholtz resonant frequency, rad/s

Part I

Dynamics and Acoustics of Cloud Cavitation on Hydrofoils

Chapter 1 Introduction

Cavitation refers to a phase change from liquid to vapor which occurs when the local pressure in a liquid flow falls below the vapor pressure of the liquid. Often cavitation inception occurs when a microbubble is convected into a low pressure region. The bubble expands rather gradually in the low pressure region and continues to grow as it passes out of the region and the pressure recovers. The bubble then suddenly collapses in an extremely violent process. This collapse produces very large pressures and temperatures at the center of the bubble. Noise is radiated into the surrounding liquid, and if the bubble collapses near a solid surface, that surface can sustain erosion damage. The details of the dynamics and acoustics of single bubble cavitation are described by Brennen (1995).

The most severe cavitation noise and erosion are produced when many bubbles collapse in close proximity to each other. This type of cavitation is commonly referred to as cloud cavitation. The very destructive effects which are observed to occur when such clouds form and collapse in a flow have been documented by, for example, Knapp (1955), Bark and van Berlekom (1978) and Soyama *et al.* (1992). The generation of cavitation clouds may occur naturally as a result of the shedding of bubble-filled vortices, or it may be the response to a periodic disturbance imposed on the flow. Common examples of imposed fluctuations are the interaction between rotor and stator blades in a pump or turbine and the interaction between a ship's propeller and the non-uniform wake created by the hull.

The angle of attack of a propeller blade can be determined by the superposition of the rotational motion of the propeller and the axial flow due to the ship's motion. The axial flow upstream of the propeller in most marine applications is highly non-uniform

due to the complicated wake flow behind the ship. The effect of such a non-uniform axial flow on cavitation observed on a ship propeller has been investigated by Sharma *et al.* (1990). This flow is generally characterized by an increasing velocity defect as the blade approaches the top position and a decreasing velocity defect as the blade approaches the bottom position. The resulting variation in angle of attack is periodic. A similar unsteady flow can be generated by oscillating a hydrofoil about its pitch axis, and this is the strategy employed in the current work.

Numerous investigators (Wade and Acosta 1966, Bark and van Berlekom 1978 Shen and Peterson 1978, 1980, Blake *et al.* 1977, Bark 1985, Franc and Michel 1988, Hart *et al.* 1990, Kubota *et al.* 1989, 1992, Le *et al.* 1993, de Lange *et al.* 1994) have studied the complicated flow patterns involved in the production and collapse of cloud cavitation on a hydrofoil. The radiated noise produced by cloud cavitation is characterized by pressure pulses of very short duration and large magnitude. These pressure pulses were measured in the work of Bark (1985), Bark and van Berlekom (1978), Le *et al.* (1993), and Shen and Peterson (1978, 1980). Recently, McKenney and Brennen (1994) qualitatively related the acoustic signature of a cavitating cloud to the dynamics of the unsteady cavitation on an oscillating hydrofoil.

Analytical studies of the dynamics of cavitation clouds can be traced to the early work of van Wijngaarden (1964) who modeled the behavior of a collapsing layer of bubbly fluid next to a solid wall. Later investigators explored numerical methods which incorporate the individual bubbles (Chahine (1982)) and continuum models which, for example, analyzed the behavior of shock waves in a bubbly liquid (Noordzij and van Wijngaarden 1974, Kameda and Matsumoto 1995) and identified the natural frequencies of spherical cloud of bubbles (d'Agostino and Brennen (1983))). Indeed the literature on the linearized dynamics of clouds of bubbles has grown rapidly (see, for example, Omta (1987), d'Agostino and Brennen (1988, 1989), Prosperetti (1988)). However, apart from the weakly non-linear analyses of Kumar and Brennen (1991,

1992, 1993), only a few papers have addressed the highly non-linear processes involved during the collapse of a cloud of bubbles. Chahine and Duraiswami (1992) have conducted numerical simulations using a number of discrete bubbles and demonstrated how the bubbles on the periphery of the cloud develop inwardly directed re-entrant jets. However, most clouds contain many thousands of bubbles and it therefore is advantageous to examine the non-linear behavior of continuum models.

Another perspective on the subject of collapsing clouds was that introduced by Mørch (1980, 1981) and Hanson, Kedrinskii and Mørch (1981). They speculated that the collapse of a cloud of bubbles involves the formation and inward propagation of a shock wave and that the geometric focusing of this shock at the center of cloud creates the enhancement of the noise and damage potential associated with cloud collapse. It should also be noted that Jakobsen (1964) suggested that a static bubbly condensation shock occurs in the closure region of a large attached and bubbly cavity and provides the basic mechanism for cavity closure. Recently Wang and Brennen (1994) have used the mixture models employed earlier by d'Agostino and Brennen (1983, 1988, 1989) to study the non-linear growth and collapse of a spherical cloud of bubbles. A finite cloud of nuclei is subjected to a temporary decrease in the ambient pressure which causes the cloud to cavitate and then collapse. Their calculations confirm the view of cloud collapse put forward by Mørch, Kedrinskii and their co-workers.

The main objective of the current experiments was to identify the physical processes responsible for the dynamics and acoustics of cloud cavitation on a three dimensional hydrofoil and relate these observations to the analytical and experimental investigations mentioned above.

Chapter 2 Experimental Facilities and Techniques

2.1 Low Turbulence Water Tunnel and Related Instrumentation

The Caltech Low Turbulence Water Tunnel (LTWT) is a closed-circuit facility, with a $30.5cm$ by $30.5cm$ by $2.5m$ test section and a $16:1$ contraction ratio. A schematic of the facility is shown in Figure 2.1. The LTWT is equipped with a vacuum pump so that the static pressure can be varied without changing the tunnel velocity. The total air content of the water in the tunnel can be reduced to as low as $3ppm$ by using the vacuum deaeration system which consists of a large pressure vessel with spray nozzles at the top, drain and fill pumps which are controlled by float valves and the vacuum pump. The LTWT is capable of free stream velocities up to $10m/s$ and can support pressures down to $20kPa$. A complete description of this facility may be found in Gates (1977).

The LTWT test section has been instrumented with a number of sensors for measuring the free stream velocity, absolute pressure and the radiated acoustic pressure. Figure 2.2 illustrates the layout of the test section along with some of the instrumentation. In particular, the radiated unsteady pressures generated by the cavitation on the hydrofoil were measured by piezoelectric transducers. Two PCB model HS113A21 pressure transducers (bandwidth $100kHz$) were mounted flush with the floor and ceiling of the test section, approximately $5cm$ downstream of the trailing edge of the foil.

During some preliminary studies, radiated acoustic pressure measurements were made using a B&K model 8103 hydrophone (bandwidth $100kHz$) installed in a Lucite box filled with water and affixed tightly to the outside of the test section. As demonstrated by Bark and van Berlekom (1978), mounting a hydrophone externally in this way significantly degrades the signal. Comparing simultaneous measurements from the B&K hydrophone and the PCB transducer (figure 2.3), it is clear that the transducer yields a much cleaner signal. Acoustic pressure intensities calculated using the output from the hydrophone in the box were significantly smaller in magnitude than those derived from the flush-mounted transducer for the same event. This indicates that the presence of the walls of the test section and the lucite box has a significant attenuating effect on the measured signal. The signal for the external hydrophone was significantly adulterated by resonances within the box. The raw signal from the B&K hydrophone contained a large sinusoidal component at $150Hz$ which corresponds to the first resonant frequency of the box. This artifact of the box is not evident in figure 2.3 only because the B&K hydrophone signal was high pass filtered at $500Hz$ prior to generating this plot. Although the PCB transducer lacks the omnidirectional capability of the B&K hydrophone, the transducer was mounted directly beneath the cloud collapse region and thus the radiated acoustic pressure impinges with nearly normal incidence. The PCB transducer produced results with greater scatter, but better signal to noise ratio. These conclusions are very similar to those reached by Bark and van Berlekom (1978), and led to the decision to focus on the results obtained with the PCB (flush-mounted) transducer.

2.2 Oscillating Foil Mechanism and NACA 64A309 Hydrofoil

The current experiments were performed using two different hydrofoils which were connected, in turn, to the same oscillation apparatus. This mechanism was designed by Hart (1993) and consists of a $750Watt$ DC motor connected to a four-bar linkage such that the foil oscillates nearly sinusoidally in pitch about a point near the center of pressure, $0.38c$ from the leading edge. This apparatus is depicted along with the rest of the LTWT test section in figure 2.2. The mean angle of attack can be adjusted continuously by using a collet connecting the oscillation linkage to a coupling shaft. The oscillation amplitude can also be adjusted by changing the pivot point of the oscillation linkage connection to the motor spindle, although the maximum allowable amplitude of $\pm 5°$ was used in all of the current experiments. The frequency of oscillation can be continuously varied from 0 to $50Hz$. The shaft, which is connected to the foil, has a hole bored through its center allowing wiring for instrumentation to be passed out of the test section as well as allowing a passageway for air to be injected into the test section. Both foils mount to their own circular plates which are bolted to this shaft. An optical shaft encoder mounted to the DC motor provides a digital signal (1024 pulses per revolution) which was used to synchronize acoustic measurements with the phase of the foil.

The early experiments presented here, including the parametric study of the acoustic impulse (see chapter 3) were performed using a NACA 64A309 asymmetric hydrofoil which was reflection-plane mounted in the test section using the oscillation mechanism described above and shown in figure 2.2. The foil cross-section is depicted graphically in figure 2.4. This hydrofoil has a rectangular planform with a chord of $15.2cm$ and a span of $17.5cm$; it is made of stainless steel and polished to a smooth finish. A further discussion of the NACA 64A309 foil and the oscillation

mechanism can be found in Hart (1993) which also contains detailed schematics of these devices.

2.3 Modified NACA 0021 Hydrofoil and Related Instrumentation

To obtain measurements of unsteady surface pressures, a modified NACA 0021 hydrofoil with increased thickness between the mid-chord and the trailing edge was fabricated. The increased thickness was intended to accommodate pressure sensing instrumentation. Figure 2.5 provides a graphical representation of the cross-section. A symmetric hydrofoil was chosen to facilitate the machining which was performed using the CNC machine in the Caltech Mechanical Engineering Shop. The hydrofoil has a rectangular planform with a chord of $15.2cm$ and a span of $17.5cm$, the same values used in the design of the NACA 64A309 foil. The NACA 0021 foil is made of brass for corrosion and machining considerations and is polished to a smooth finish. The foil is reflection-plane mounted in the test section and connected to the same oscillation mechanism described in section 2.2. The pivot point of oscillation remains the same as that used for the previous foil, $x/c = 0.38$.

Several different methods were explored in an effort to instrument the foil for the measurement of unsteady pressures on the suction surface. Ultimately, the most successful method was the installation of four PCB model 105B02 pressure transducers (bandwidth 50 kHz) inside the foil. The locations of the transducers are shown in figure 2.6. The transducer sensing regions were located at approximately 26% span from the foil root and 30%, 50%, 70% and 90% chord from the leading edge. The longitudinal axis of the transducers was installed in the spanwise direction, and a shaft was drilled normal to the foil surface extending beyond the sensing region of the transducer. The diameter of the sensing region of the PCB 105B02 transducer is

$0.99in$. The four wires were routed through channels cut in the bottom cross-section of the foil and passed out of the tunnel test section through the oscillation mechanism coupling shaft. The wire channels and transducer mounting shafts were sealed using epoxy and O-rings.

One concern arising from the recess mounting of the transducers was the limitations imposed on the effective bandwidth of the instrumentation due to the corrupting effect of the recess cavity frequency characteristics. For this reason, the depth of the recess was chosen to be the minimum allowable by the machining requirements of the transducer mounting. The Helmholtz resonant frequencies, ω_r, are given by the solutions to the equation:

$$\cos\left(\frac{\omega_r l}{c}\right) = 0,$$

where c is taken to be the speed of sound in water, $1460m/s$, and l is the depth of the recess, $\frac{3}{8}in$. Using these values, the first resonant mode occurs at $\omega_r = 2.41(10)^5 rad/s$, or at a frequency of $38.3kHz$.

This theoretical value was confirmed empirically by performing an in-situ impulse response test of the instrumentation. An electronic circuit was built to supply an impulsive voltage to a B&K 8103 hydrophone. This hydrophone was placed in the test section approximately $2in$ from the suction surface of the hydrofoil at approximately 40% of the chord from the leading edge. The hydrophone spanwise position was at the level of the transducer recess locations. A sample result from these tests can be seen in figure 2.7 which depicts the output of each of the four transducers to the impulse pressure excitation. A clear resonance is evident in the time domain and after performing a Fast Fourier Transform on the signals, resonant peaks were easily detected in the frequency domain. The locations of these resonant peaks were $32kHz$, $36kHz$, $30kHz$ and $32kHz$ for transducers #1, #2, #3 and #4, numbered from the leading edge, respectively. Subsequently, all data taken by the foil transducers was digitally low pass filtered at $20kHz$ to avoid any corrupting effect of cavity resonance.

It was also acknowledged that the presence of an air bubble in the recess would result in a major reduction in the frequency response. Great care was taken to avoid trapping air inside the recesses while filling the tunnel test section with water. Set-screws could be removed from the pressure side of the foil to create a passageway from the recess bottom through the entire foil cross-section. Air bubbles were removed by forcing water through the recesses using a squeeze-bottle and hypodermic needles and by running the tunnel at high speeds with the foil placed at a 90° angle of attack. Eventually it was determined that forcing water into the recesses using the bottle and needle without removing the set-screws was sufficient to flush out any air bubbles.

The presence of an air bubble in a recess was easily detected during the determination of the frequency response of the transducers. When air bubbles were intentionally placed inside a recess during an impulsive pressure excitation, a severe attenuation of the time domain signal was observed and the resonant peak in the frequency domain was no longer readily detected. Figure 2.8 depicts the time domain response of the four recess mounted transducers with an air bubble intentionally placed in the recess for transducer number 2. By using this method prior to running the current experiments, the absence of air bubbles inside the transducer recesses could be confirmed.

The sensitivity (conversion from voltage to pressure) of each transducer as supplied by the manufacturer was confirmed by an in-situ calibration procedure. This procedure consisted of driving an ITC 1042 hydrophone placed in the LTWT test section with a sinusoidal voltage signal and comparing the measured sinusoidal pressure amplitude registered by each transducer with that measured by the B&K 8103 hydrophone. The input voltage signal was provided by a Invertron Model 161A AC Power Supply manufactured by Behlman-Invar Electronics. This power supply is capable of generating sinusoidal voltage signals of up to $5kHz$ at up to $100V_{rms}$. The ITC hydrophone was placed approximately $9\frac{1}{4}in$ from the suction surface of the hydro-

foil at approximately 40% of the chord from the leading edge. The ITC hydrophone spanwise position was $4in$ from the root of the hydrofoil. The B&K hydrophone, with a known sensitivity, was placed sequentially in front of each transducer recess to provide a reference value. Several frequencies, ranging from 3 to 5 kHz, were used for the input signal to the ITC hydrophone. The results of these tests are shown in figure 2.9 which plots the ratio of the amplitude of the acoustic field measured by each transducer to the amplitude measured by the B&K hydrophone for five different input frequencies. This ratio varies from 0.5 to 2 for the majority of the data points, although some outlying points have values as high as 4 and as low as 0.3. In general, the frequencies which produced ratios that were the furthest from unity also produced the least spatially uniform acoustic fields. Thus, the discrepancies noted in the data can be attributed to the complex acoustic environment inside the LTWT test section which is expected to generate standing waves and pressure nodes and antinodes.

As mentioned previously, several attempts were made to instrument the NACA 0021 hydrofoil for surface unsteady pressure measurement before selecting the recess mounted PCB 105B02 transducers. Two such attempts failed due to the extremely adverse environment created by the cloud cavitation process, the full extent of which was not fully appreciated until after obtaining successful measurements using the recess mounted transducers. The NACA 0021 foil was originally designed to accommodate a new experimental microtransducer from PCB, model number V132A32. These transducers were only $\frac{1}{8}in$ in diameter and $0.3in$ long which allowed them to be flush mounted in the foil. Four transducers were mounted in the foil by clamping them between semi-cylindrical depressions drilled into each of the two sections of the NACA 0021 foil. Indeed, the NACA 0021 foil was machined as two pieces precisely for this reason. These transducers were not designed for pressure pulses as large as those which were eventually found on the suction side of the oscillating foil, and they failed after less than one hour of operation.

Another attempt was then made using a piezo polyvinylidene fluoride (PVDF) sensor manufactured by AMP, Inc. This PVDF sensor consists of a piezoelectric polymer film upon which a layer of metal is deposited in the desired pressure sensing region. The particular sensor that was used had four such sensing elements spaced just under $1cm$ apart on the same PVDF film. A charge amplifier circuit was built and the effective sensitivities of the four sensing regions were determined by comparing the output from the AMP sensor with the output from an operational PCB V132A32 transducer while generating a sinusoidal acoustic field using the ITC 1042 hydrophone. The AMP sensor exhibited two problems. The first difficulty was the limited spatial resolution afforded by the PVDF sensor. A large impulsive pressure applied at a certain point on the film would induce a stress throughout the polymer and register on all four sensing regions simultaneously. This difficulty could have been overcome by using four separate PVDF film elements with a single metalization region on each. A more severe problem was posed by the installation of the sensor on the foil. The sensor was applied to a depression machined into the foil's surface using epoxy. This method proved to be insufficiently robust since within a few minutes of cloud cavitation inception the sensor detached from the foil surface and was destroyed.

2.4 Data Acquisition Techniques

The output from the various acoustic sensors and the timing information from the hydrofoil shaft encoder were recorded using a PC based data acquisition system. The core of this system consisted of a R.C. Electronics ISC-16 digital data acquisition card. This card is capable of recording up to 16 input channels at an aggregate sampling rate of up to $1MHz$. The system can store up to 64k words of data in memory each time it is triggered and the card has a 12 bit accuracy over a ± 10 volt input range. The RC card was periodically calibrated using a Tektronix 2213A $60MHz$

oscilloscope.

A sampling rate of approximately $143kHz$ was used for the experiments with the NACA 64A309 foil and a rate of $100kHz$ was used with the NACA 0021 foil due to the increased number of acoustic sensors. The transducer output was low pass filtered prior to A/D conversion using Krohn-Hite Model 3202 analog filters. The cutoff frequency was set just below the Nyquist frequency to prevent aliasing. A value of $70kHz$ was used for the NACA 64A309 experiments and $45kHz$ for the NACA 0021 experiments.

All of the PCB transducers were connected to PCB model 482A05 power supplies. In addition, several amplifiers including a Stanford Research Systems model SR560, and a Princeton Applied Research model 113 were used in conjunction with the PCB HS114A21 transducers. The PCB 105B02 transducer output did not require amplification during the cloud cavitation experiments.

2.5 High Speed Motion Picture and Still Photography Techniques

High speed movies were taken of the hydrofoil cavitation using a Locam II model 50-0003 $16mm$ motion picture camera manufactured by the Redlake Corporation. These movies were shot at 500 frames per second using Kodak EXR 7298 ASA 500 Tungsten color negative film. (Some of the early experiments used Kodak 7250 ASA 400 Tungsten color reversal film.) Up to three halogen lamps were used to provide illumination. Both 1000 Watt and 500 Watt lamps were used at various times. One lamp was placed directly above the hydrofoil and shone through a porthole in the test section ceiling. Another lamp was placed upstream of the foil and illuminated the foil through the test section side window at an angle of incidence of approximately 30°. At times, a third lamp was placed downstream of the foil shining through the

side window at an incidence of approximately 20°.

The high speed motion pictures provide a visual record of the cavitation structures and events which were present at the time the acoustic measurements were made. Two different techniques were used to synchronize the motion picture frames with the acoustic data. Both of these techniques rely upon an electronic pulse which is generated by the foil motor control unit (Hart (1993)) at a particular position in the foil's oscillation. In the case of the NACA 64A309 hydrofoil, this pulse corresponded to the minimum angle of attack of the foil. For the NACA 0021 foil, the pulse corresponded to the maximum angle of attack.

The early experiments with the NACA 64A309 foil utilized an LED inside the camera which was designed to place a mark on the edge of the film when it is triggered by an external signal. This signal was generated by a circuit which supplied the signal to the LED upon receiving the synchronization pulse from the foil motor control unit. When the user pressed a switch, the circuit would not trigger the LED upon receiving the next synchronization pulse; rather the circuit would instead initiate data acquisition upon detecting the pulse. Thus, by searching for the missing LED mark on the film, the time of data acquisition initiation could be determined. This method is described in greater detail in McKenney (1995). This method had an error of $\pm 2 frames$ due to uncertainties in the measurement of the number of frames between the LED location and the camera aperture and the estimation of the missing pulse location. In addition, the procedure required to find the missing LED mark proved to be both time-consuming and inconvenient.

The method used for the NACA 0021 foil experiments consisted of placing a LED in the frame of view of the camera. The circuit designed by McKenney (1995) was used to initiate data acquisition upon detection of the synchronization pulse from the foil motor control unit, but the LED affixed to the test section wall would illuminate simultaneously. By noting the frame in which the LED illuminated, the accuracy was

improved to a 2 frame interval.

In addition to the high speed motion pictures, still photographs were also taken of various stages of the cavitation process by using the foil motor control unit timing to trigger an EG&G Model 549-11 Microflash strobe lamp at the desired phase of the foil oscillation cycle. This strobe lamp has a flash duration of $0.5\mu sec$ and a peak output of $50(10)^6$ candlepower.

2.6 Total Air Content Determination

The total air content (TAC) of the LTWT working fluid was measured before and after each experiment using a Model 2975-A10 Thomas-Van Slyke Magnematic Blood Gas Apparatus manufactured by the Arthur H. Thomas Company. This apparatus separates the air from the water sample by vigorously stirring the liquid while under a vacuum. By measuring the height of a mercury manometer before and after expelling the separated air and correcting for the ambient temperature, the TAC is calculated. This method has the advantage of measuring the total air content, both due to dissolved gas and due to microbubbles, rather than measuring only the dissolved gas. However, the apparatus demands a high degree of manual dexterity on the part of the operator to achieve accuracies on the order of $\pm 0.5ppm$ and the device also requires periodic maintenance.

2.7 Data Analysis Techniques

The current experiments will demonstrate that the acoustics of cloud cavitation are predominated by large amplitude high frequency impulse pressures. Thus, cloud cavitation acoustics are similar to the smaller amplitude radiated acoustic pressures generated by single bubble cavitation (see, for example, Fitzpatrick and Strasberg

(1956), Blake (1986), Ceccio and Brennen (1991), Hamilton *et al.* (1982), Kuhn *et al.* (1992), Kumar and Brennen (1993), etc.) and a similar data processing method can be applied.

Although some cavitation researchers have used the peak radiated acoustic pressure (e.g. Van der Meulen(1989), Bark (1985), etc.) and the sound power spectral density (e.g. Arndt *et al.* (1993), Blake *et al.* (1977), etc.), in the current work the magnitude of the cavitation noise will be characterized by the acoustic impulse, I. This method was first used by Ceccio and Brennen (1991) to quantify single traveling bubble acoustics. The acoustic impulse is defined as the area under the acoustic pulse or

$$I = \int_{t_1}^{t_2} p_a dt,$$

where t_1 and t_2 are chosen in a systematic manner to identify the beginning and end of the pulse. This method isolates the radiated acoustic pressure generated by a specific event while neglecting low-frequency variations in pressure as well as low-amplitude high-frequency noise. The acoustic impulse is directly related to the acoustic energy released during a single bubble collapse and has been correlated with the maximum bubble volume (Ceccio (1990)).

It was also useful in the analysis of the far-field acoustic data to define a dimensionless impulse, I^*, as

$$I^* = \frac{16\pi I\mathcal{R}}{\rho U L^2},$$

where $\mathcal{R}$ is the distance from the cavitation event to the point of noise measurement and L is the typical dimension of the flow, taken in the present work to be the chord of the foil. This normalization was not employed in the analysis of the unsteady surface pressure measurements due to the difficulty in determining a proper value of $\mathcal{R}$ in this case.

In practice, algorithms written using MATLAB software (MATLAB Reference Guide (1992)) were used to calculate the acoustic impulse for a given data file. The

methodology was fundamentally similar to that used by Kumar (1991) and Ceccio (1990). After loading one 64k buffer from the RC card into MATLAB, the algorithm would truncate the signal so that only a single oscillation cycle would be present. At high oscillation frequencies, two complete oscillation cycles could be captured in one buffer and both would be used. Since only unsteady pressures were measured by the transducers and digital filtering was to be employed, the mean was subtracted from the signal. The voltage signal was then converted to pressure using the manufacturer's sensitivities and any gains used for amplification were accounted for. When data from the recessed PCB 105B02 transducers was being analyzed the signals would be low-pass filtered with a cut-off frequency of $20kHz$ to avoid spurious effects of cavity resonance. In preparation for the impulse calculation, the data would be high-pass filtered. The source code for the impulse calculation algorithms can be found in appendix B.

Choosing the limits of integration for the acoustic impulse calculations proved to be a non-trivial procedure; if the limits are poorly chosen the results may depend heavily on irrelevant artifacts in the data. In practice, the values of t_1 and t_2 were determined by a threshold crossing method which in turn depended on the choice of the high-pass filtering cut-off frequency and the choice of the threshold level itself. The cut-off frequency was chosen to be high enough to prevent low frequency pressure fluctuations caused by the foil motion from producing a spurious threshold crossing but low enough to prevent degradation of the high frequency impulse signals. In this manner, a cut-off frequency of $50Hz$ for the floor and ceiling transducers and $600Hz$ for the foil surface transducers was chosen.

After selecting the optimal cut-off frequency, a threshold level was set just above the very high frequency electrical noise level present in the signals. When the calculated impulse is plotted as a function of threshold level, a large increase in impulse can be seen as the threshold level drops below a certain value corresponding to the

high frequency noise amplitude. In this manner, a threshold of $20kPa$ was selected for the floor and ceiling data and a threshold of $200kPa$ was chosen for the foil surface transducers.

Significant cycle-to-cycle variation was present in the acoustic impulse so about 40 data files were collected at each operating condition. The average impulse value for 40 samples was found to be very repeatable where a single sample is defined by either one oscillation cycle or a $0.066sec$ time period in the case of the static foil experiments. The $0.066sec$ time period corresponded to the length of the data acquisition hardware memory buffer.

During the acoustic impulse parametric study which is described in chapter 3, the spectra of the radiated acoustic signals measured by the floor transducer were compared under the different flow conditions. To allow for statistically significant results, average spectra from approximately 40 individual (unfiltered) cycles were acquired. First the spectrum from each raw signal was normalized by the area under that spectrum following the method described in Kumar (1991); then the normalized magnitudes at each frequency were averaged over all the cycles. The source code used for this analysis can be found in appendix B with a filename of spec2.m.

A modification to the acoustic impulse algorithm was introduced for the experiments involving unsteady surface pressure measurements. The data would be displayed on the screen and the user would be prompted to input the portion of the oscillation cycle which corresponded to the global event. (For a definition of global and local events, see chapter 5.) This information would allow the algorithm to distinguish between the contribution of the local and the global events to the total acoustic impulse. The source code for this calculation can be found under filename shockimp.m in appendix B.

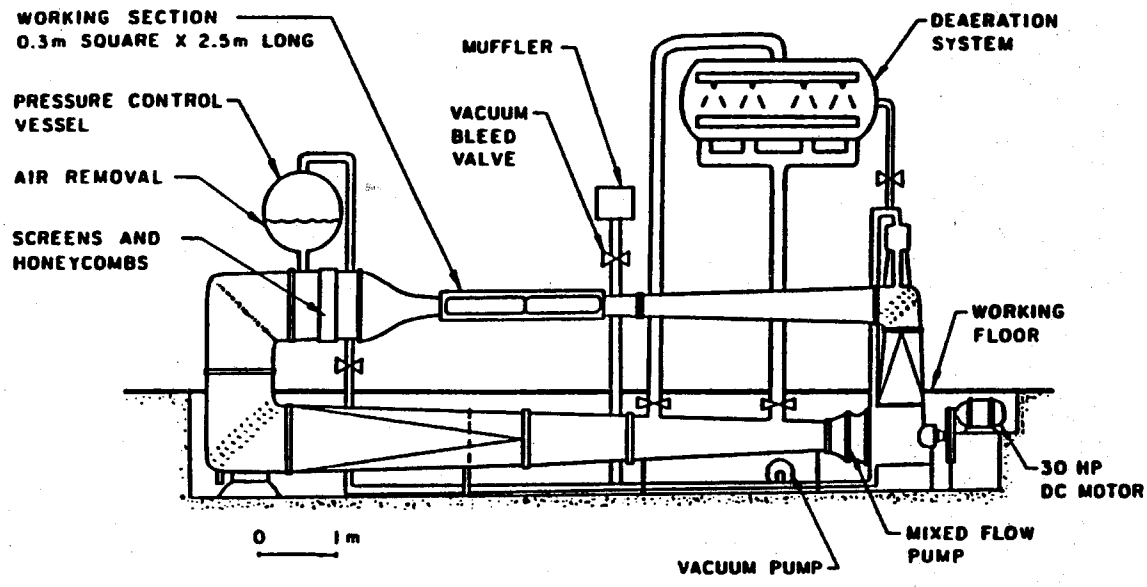

Figure 2.1: Caltech Low Turbulence Water Tunnel

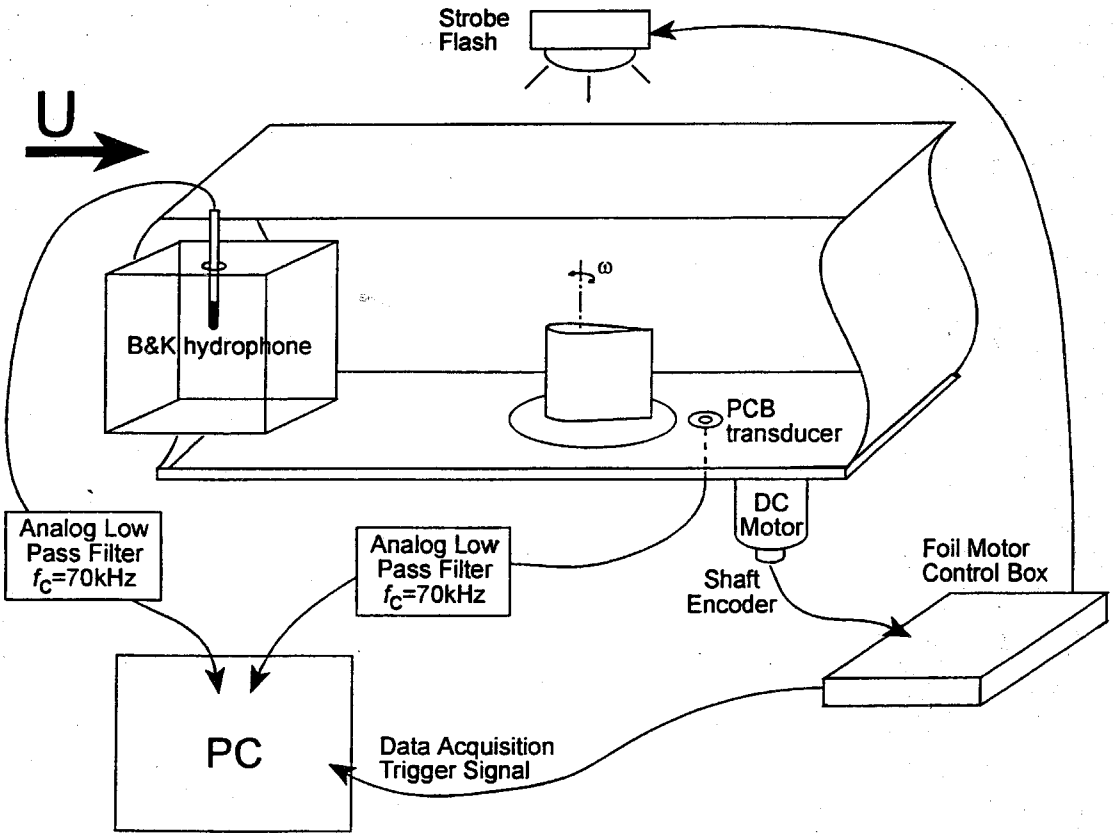

Figure 2.2: Caltech Low Turbulence Water Tunnel test section

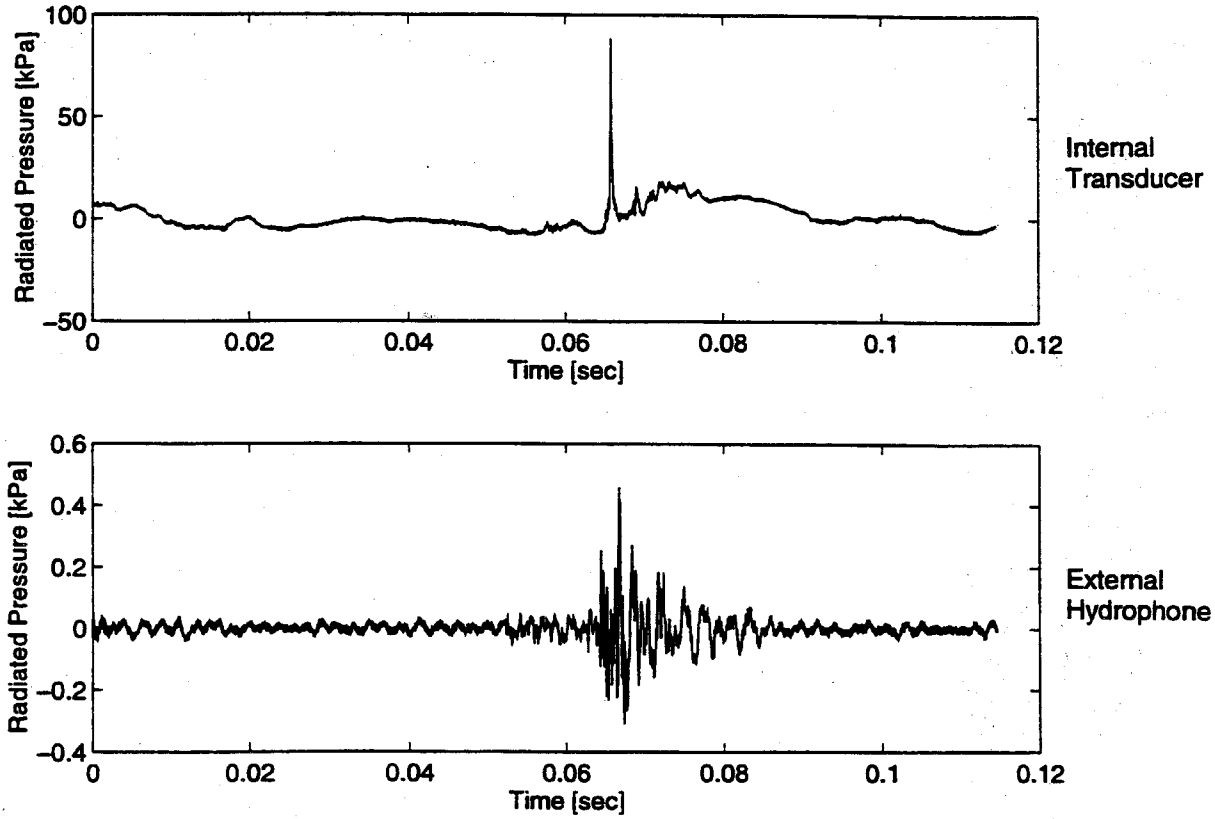

Figure 2.3: Comparison of simultaneous radiated acoustic signals using two different methods. The top signal was produced by the PCB transducer and the bottom signal was produced by the B&K hydrophone enclosed in the lucite box. McKenney (1995)

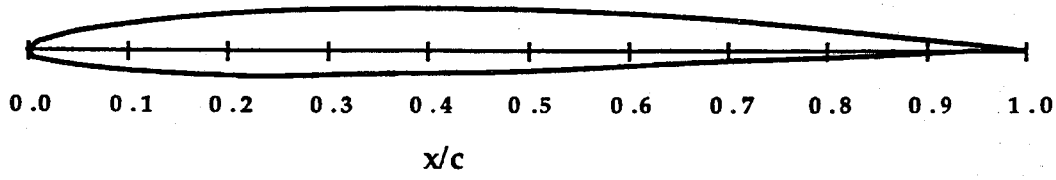

Figure 2.4: NACA 64A309 hydrofoil cross-section. The foil has a chord length of 15.2cm and a span of 17.5cm. (Hart 1993)

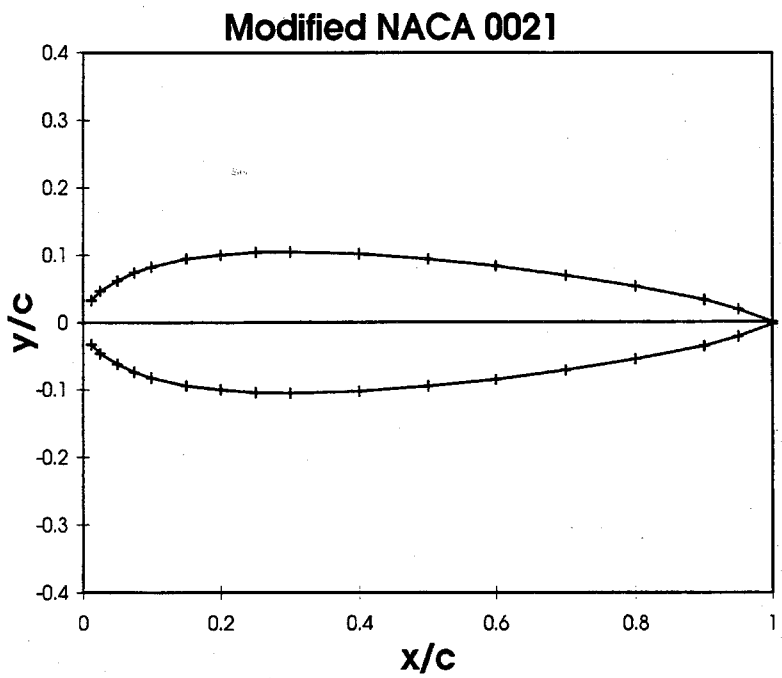

Figure 2.5: NACA 0021 hydrofoil cross-section. The foil has a chord length of 15.2cm and a span of 17.5cm.

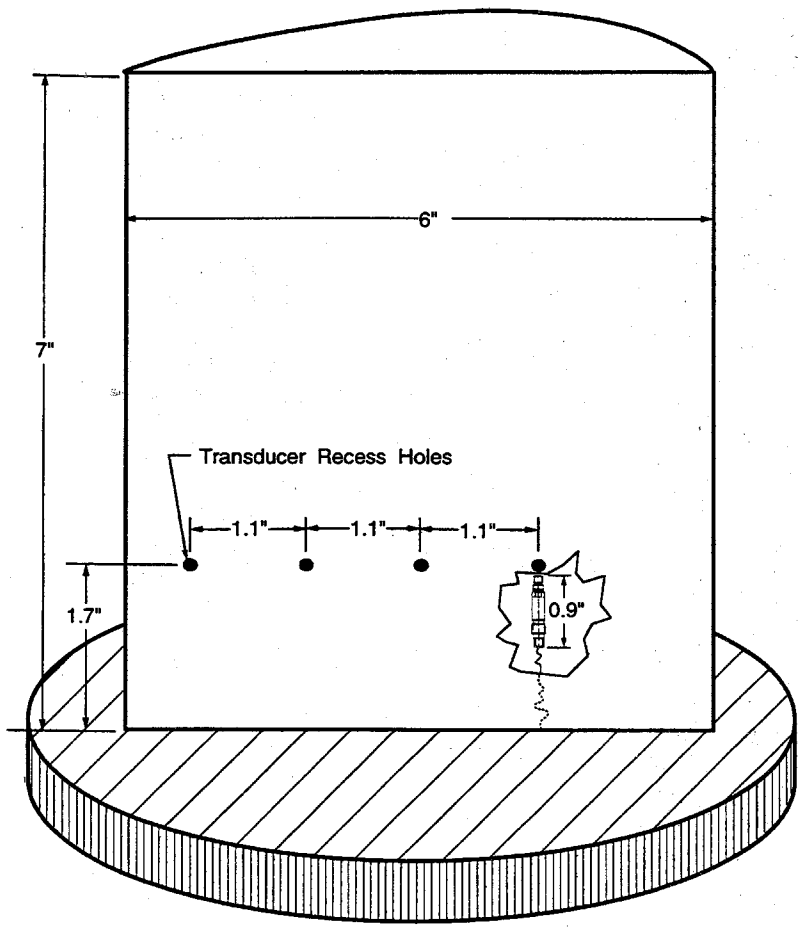

Figure 2.6: NACA 0021 hydrofoil with PCB 105B02 transducer installations. The foil has a chord length of 15.2cm and a span of 17.5cm.

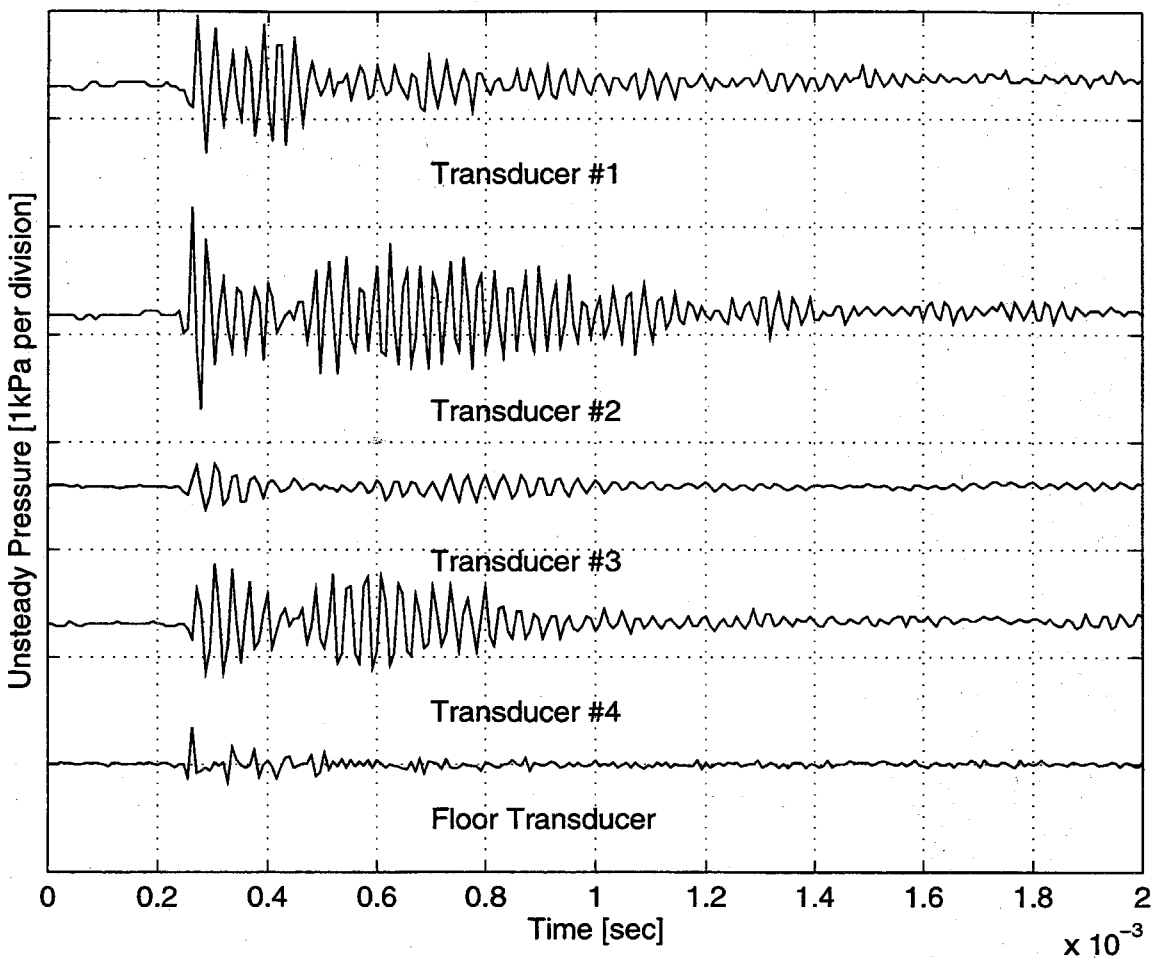

Figure 2.7: Response of the four recess mounted transducers under an impulsive excitation. The transducers are numbered from the leading edge.

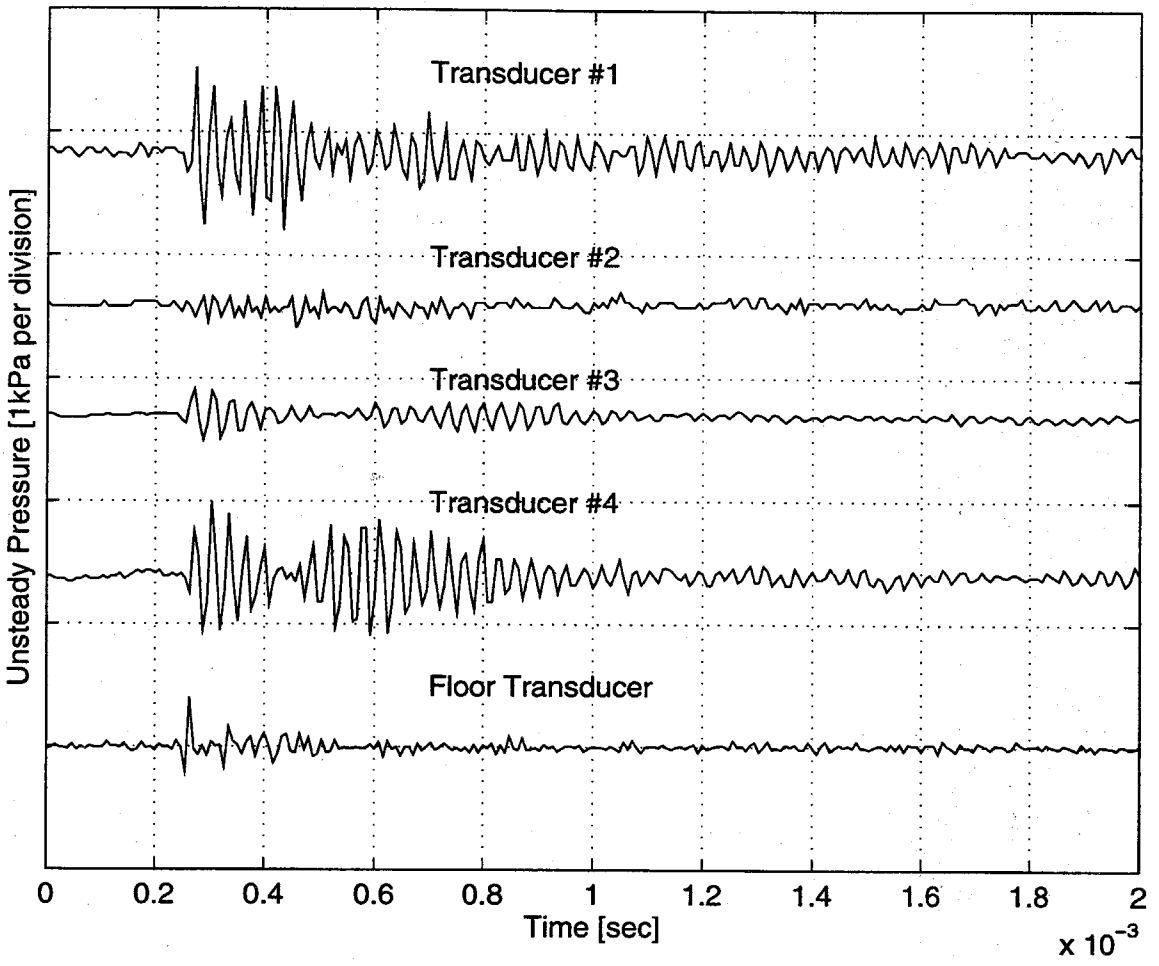

Figure 2.8: Effect of the presence of an air bubble inside a transducer recess. Response of the four recess mounted transducers under an impulsive excitation with an air bubble present in transducer number 2. The transducers are numbered from the leading edge.

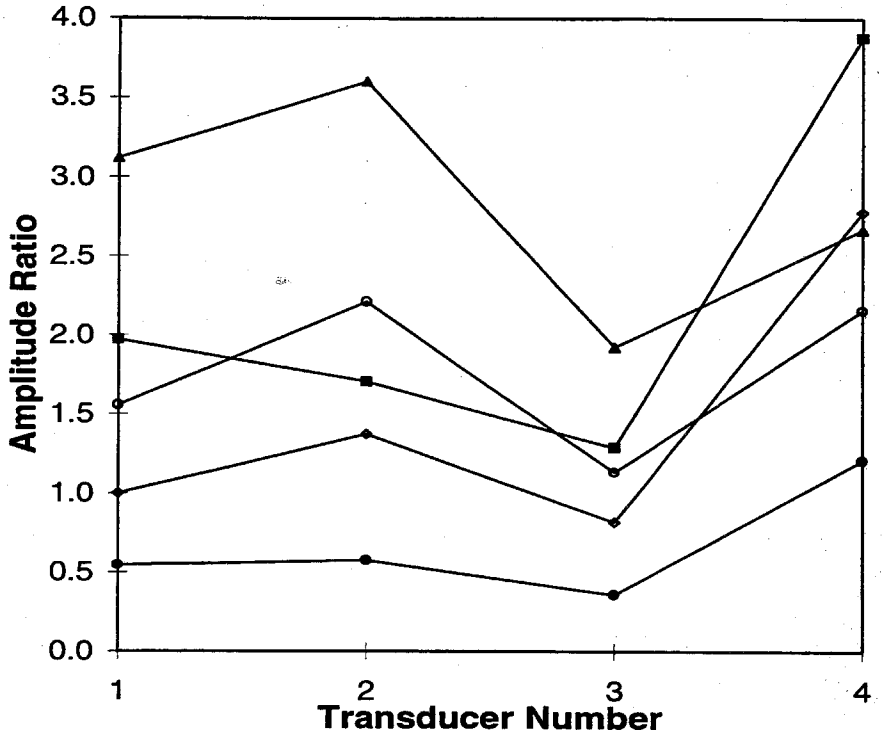

Figure 2.9: Results from in-situ calibration of PCB 105B02 recess mounted pressure transducers. Ratio of pressure amplitude measured by each transducer to a reference pressure supplied by the B&K hydrophone for five different frequencies: $3.0kHz$ (◊), $3.5kHz$ (■), $4.0kHz$ (▲), $4.5kHz$ (●) and $5.0kHz$ (○). Transducers are numbered from the leading edge.

Chapter 3 Cloud Cavitation Acoustics: Parametric Study

Initial studies of the dynamics and acoustics of cloud cavitation were performed using the NACA 64A309 hydrofoil. The effects of various flow parameters on the cloud cavitation acoustics as reflected in both the acoustic impulse and the measured spectra were established in a systematic fashion.

Experiments were conducted in the following parameter ranges:

Mean angle of attack, $\overline{\alpha_f}$	9°
Oscillation amplitude, $\Delta\alpha_f$	±5°
Reduced frequency, k	0.55 to 0.93
Cavitation number, σ	0.9 to 1.5
Air content (ppm)	4 to 10
Tunnel Velocity, U (m/s)	8

The total air content, TAC, was measured before and after each run. For most of the experiments, the TAC was in the range of $8 - 10ppm$. Then the water was deaerated so that the TAC was in the range $4 - 5ppm$, and measurements were repeated at several of the previous conditions.

Data for approximately 40 cycles were obtained at each condition, and in selected cases still photographs were taken. Figure 3.1 illustrates the cloud and sheet cavitation structures present on the oscillating hydrofoil. In this photograph, the flow is from left to right. Tip vortex cavitation is visible in the upper right corner of the photo and sheet and cloud cavitation are present on the suction side of the foil. The

dynamics of this process will be described in further detail in chapter 4.

Figure 3.2 shows a typical unsteady pressure signal from the floor transducer before high-pass filtering, along with a curve indicating the foil instantaneous angle of attack during one oscillation cycle. The origin of the time axis corresponds to $\alpha = 7.9°$ where α is increasing. Two clear pulses at about $\alpha = 10°$ represent the acoustic pressure radiated by the cloud in this particular cycle. This pulse is one of the larger ones recorded by the floor transducer during these experiments; most pulses were on the order of a few atmospheres in magnitude. The multiple peaks seen in this signal are characteristic of many of the signals obtained in these experiments. The presence of multiple peaks is either indicative of the presence of more than one event, or more likely, the result of multiple shock waves propagating through the cloud as will be discussed in further detail in section 6.2.

3.1 Parametric Study Results - Acoustic Impulse

The experimental results depicted in figures 3.3, 3.4, and 3.5 illustrate the variation of the dimensionless impulse, I^*, with cavitation number, reduced frequency and total air content. Each data point in these figures represents the average of all the impulses occurring during approximately 40 foil oscillation cycles. Within the parameter space, significant cycle-to-cycle variation was observed in both the physical attributes of the cavitation and the resulting impulse. A measure of this scatter is depicted in figure 3.3 and 3.4 by vertical bars which represent one standard deviation above and below the average impulse value. As demonstrated in these two figures, the standard deviation ranges from approximately 60% of the mean for dimensionless impulses greater than 0.4 to 120% of the mean for I^* less than 0.4. However it is important to observe that the repeatability of the mean value was approximately ± 0.1.

Figures 3.3 and 3.5 show the change in impulse with reduced frequency, k, for

different cavitation numbers. As expected, the cavitation number, σ, and reduced frequency, k, have a significant effect on the measured impulse, but no simple relationship between either of these two parameters and the impulse is evident. The highest cavitation number, $\sigma = 1.5$, resulted in the lowest impulse for all but one value of k. With the same exception, the sound level produced at $\sigma = 1.2$ exceeded the level measured at $\sigma = 0.9$. This reduction in sound level was also readily detectable in the laboratory as the cavitation number was lowered from 1.2 to 0.9. Thus, in general, the noise appears to peak at some intermediate value of σ.

Arndt, Ellis and Paul (1993), using a static hydrofoil, noted a similar non-monotonic relationship between the noise level and σ, but this behavior differs from that found by McKenney and Brennen (1994). An explanation is offered by the fact that the present mean angle of attack, $\overline{\alpha_f}$, is larger than the one used by McKenney and Brennen (1994). This seems to alter the cavitation number at which the noise peaks. In the present experiments, it was observed visually during the experiments that, for $\sigma = 0.9$, the sheet cavity not only covered nearly the entire surface of the hydrofoil, but also extended past the trailing edge for a large part of the oscillation cycle. At the lower $\overline{\alpha_f}$ used by McKenney and Brennen (1994), however, the sheet cavity seldom covered more than about 60% of the foil surface.

Although the total air content (TAC) varied from $4ppm$ to $10ppm$ during the experiments, it appeared to have little effect on the noise, as shown in figure 3.4. This result was unexpected since, as will be shown later in part 2, the injection of air into the sheet cavity, even at very low flow rates, results in a profound reduction in the measured acoustic impulse. A high level of TAC was expected to produce a similar effect due to the diffusion of air into the sheet cavity. The lack of any measurable effect of TAC can be attributed to the lack of significant diffusion during the relatively short time period associated with the unsteady cavitation growth and collapse or to an insufficient range of TAC levels explored in these experiments. This result was

not wholly unprecedented since Bark (1985) noted that the TAC had no influence on cavitation structures observed on his oscillating hydrofoil. Figure 3.5 presents a summary of the results for the averaged acoustic impulses and shows the variations with reduced frequency, cavitation number, and TAC. The results for the air injection experiments are also included in this figure and will be discussed in greater detail in part 2.

3.2 Parametric Study Results - Spectral Analysis

Further insight into cloud cavitation noise generation can be obtained by Fourier analysis of the radiated acoustic pressure. Figures 3.6 and 3.7 are two typical examples of cloud cavitation noise spectra. Each line in the figure corresponds to a single set of parameters and represents an average of approximately 40 Fourier transforms normalized using the method described in section 2.7. The spectra obtained from the current experiments exhibit a characteristic behavior proportional to f^{-n} over the frequency range of $80 - 6000Hz$, where $0.7 > n > 0.8$. This compares reasonably well with the roughly f^{-1} behavior of previous experimental results for cavitation noise spectra including the work of Blake, Wolpert and Geib (1977) and Arakeri and Shanmuganathan (1985).

Figure 3.6 presents the averaged spectra for each of the three cavitation numbers. It is clear that there is a significant change in the spectrum with cavitation number particularly in the range from $100Hz$ to $7kHz$. Moreover, the relative changes in magnitude in this range correspond with the previously described changes in the acoustic impulse with σ. This result differs from the monotonic increase in spectral density with decreasing cavitation number which was reported by Blake, Wolpert and Geib (1977) for both sheet and traveling bubble cavitation on a static foil, but Arndt, Ellis and Paul (1993), also using a static foil, measured a non-monotonic relationship

between the noise spectral density and σ in the frequency range of $1kHz$ to $10kHz$.

Figure 3.7 shows that the frequency content of the sound changes little with variation in the reduced frequency of foil oscillation. Average spectra were also examined for different air contents, but showed little change with this parameter.

The large peak in the spectra at $4kHz$ appears for every data set in the entire parameter space. This $4kHz$ peak is even observed in the spectral analysis of data taken at high pressures when no cavitation was present on the foil. It can be shown that the fundamental resonant frequency of the LTWT test section is $3.5kHz$. Apparently, the $4kHz$ peak is an artifact of the LTWT facility. This conclusion is further supported by the fact that the location and relative magnitude of the peak shows no appreciable variation with the various flow parameters including σ and k.

3.3 Comparison to Single Traveling Bubble Impulses

It is interesting to compare the results for the acoustic impulse (depicted in figure 3.5) with previous results for single traveling bubble cavitation. Figure 3.8 illustrates the approximate relation between the cloud cavitation impulses, the impulses observed by Kuhn de Chizelle *et al.* (1995) for single traveling bubbles, and the impulse magnitudes predicted by the Rayleigh-Plesset equation for a spherical bubble. The discrepancy between the empirical and theoretical results for traveling bubble cavitation is attributed by Kuhn de Chizelle *et al.* (1995) to a lack of sphericity exhibited by the observed bubbles. From this figure, it is evident that the noise generated by cloud cavitation is several orders of magnitude larger than the sound level resulting from single traveling bubble cavitation. The impulses generated by some clouds are even greater than the theoretical prediction for a single spherical bubble of the same maximum volume, suggesting that clouds are very effective noise sources.

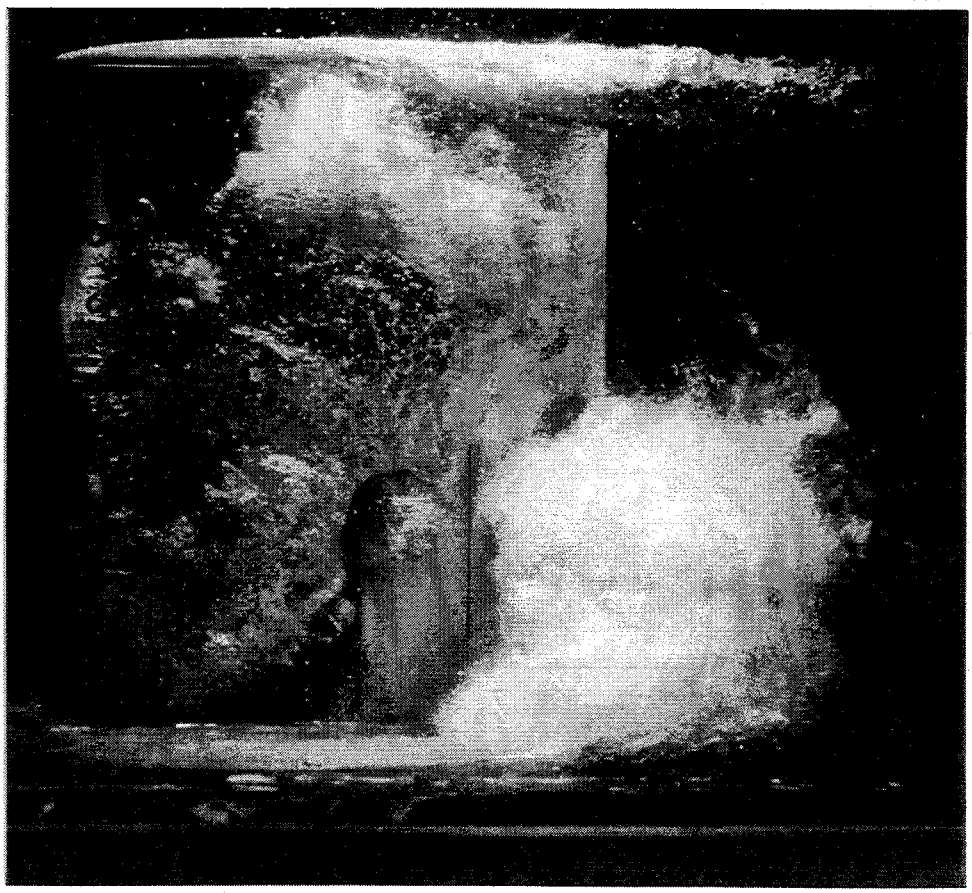

Figure 3.1: Cloud cavitation on the oscillating NACA 64A309 hydrofoil. $\sigma = 1.2, k = 0.9, U = 8m/s$.

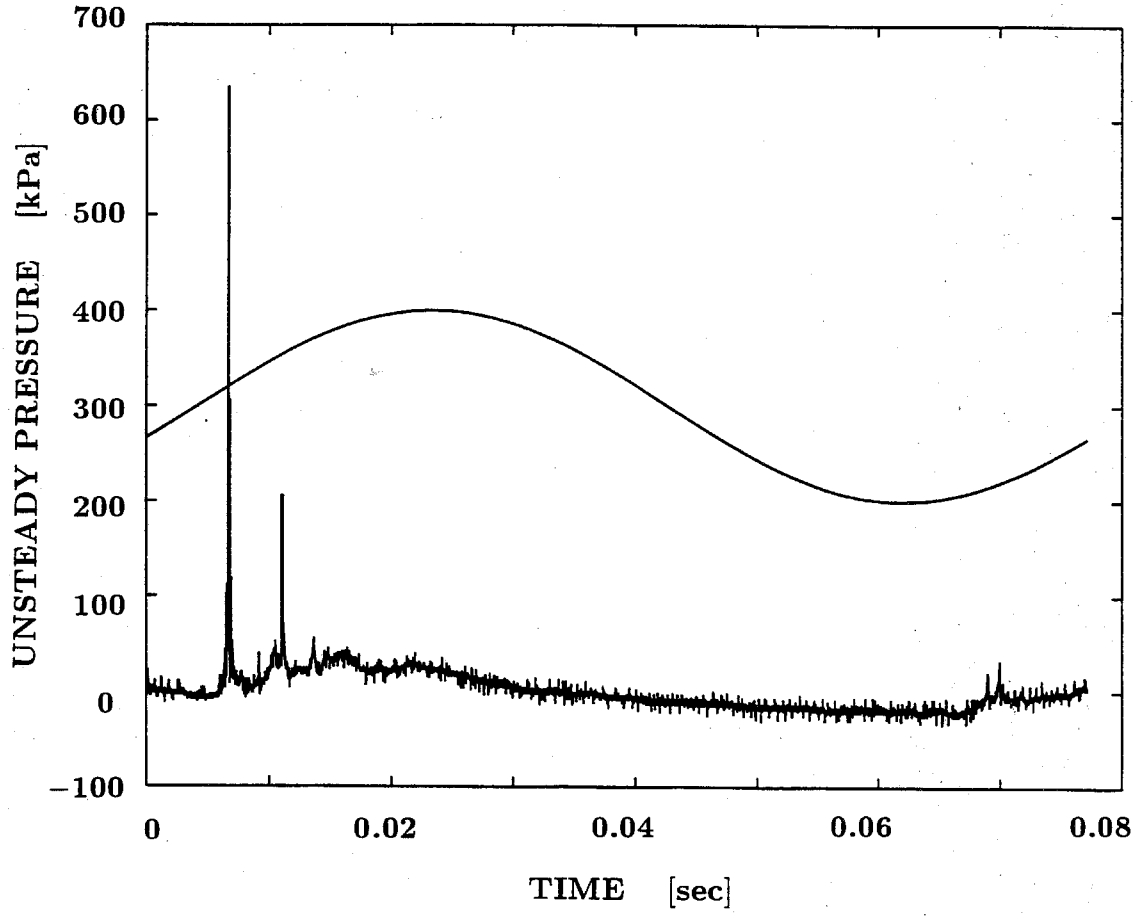

Figure 3.2: Typical output from the PCB HS114A21 transducer located in the tunnel test section floor. The signal from one oscillation cycle is shown together with a sinusoid qualitatively representing the instantaneous angle of attack of the foil. Data for $\sigma = 1.0$, $k = 0.8$, $TAC = 4 - 5ppm$, $U = 8m/s$.

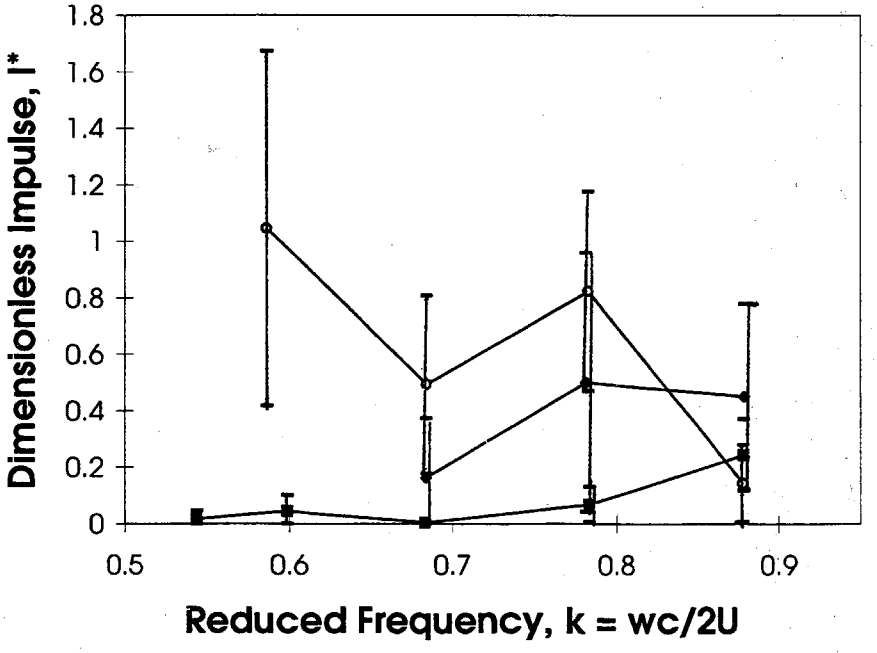

Figure 3.3: Effect of cavitation number, σ, on the dimensionless impulse, I^*. Data shown for $\sigma = 0.9$ (♦), $\sigma = 1.2$ (○), $\sigma = 1.5$ (■) with $TAC = 7 - 10ppm$, $U = 8m/s$.

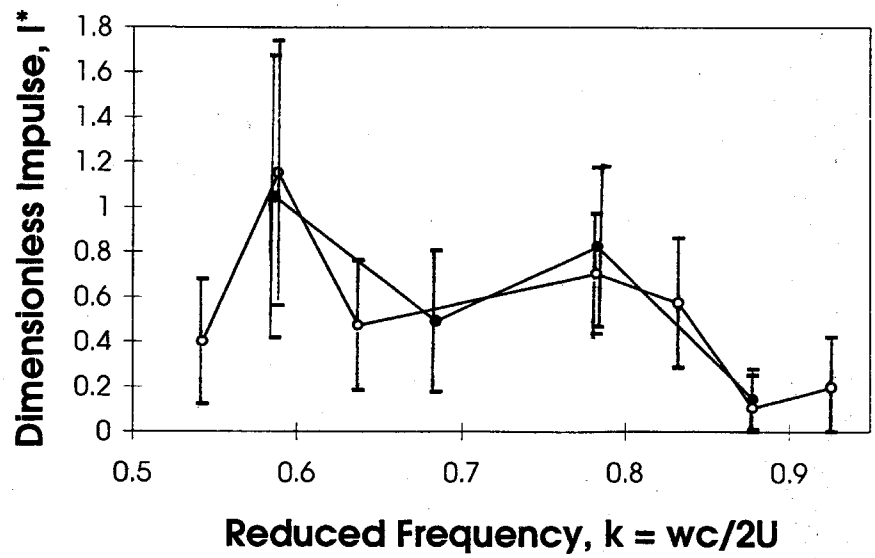

Figure 3.4: Effect of total air content (TAC) on dimensionless impulse, I^*. Data shown for $TAC = 4 - 5ppm$ (○), $TAC = 8 - 10ppm$ (●) with $\sigma = 1.2$, $U = 8m/s$.

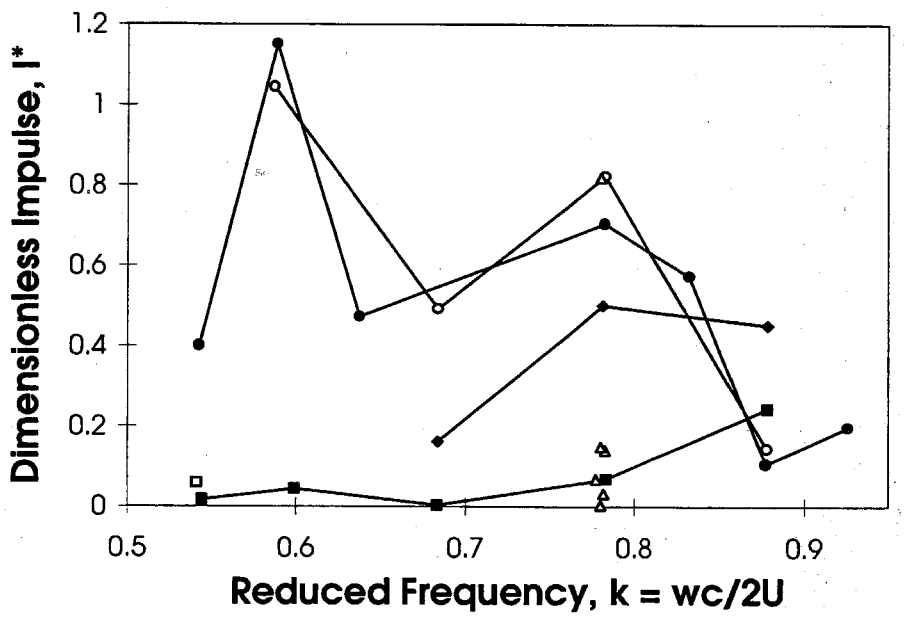

Figure 3.5: Summary of dimensionless impulse data for cloud cavitation. Data without air injection: $\sigma = 0.9$, $TAC = 7 - 8ppm$ (♦); $\sigma = 1.2$, $TAC = 4 - 5ppm$ (●); $\sigma = 1.2$, $TAC = 8 - 10ppm$ (○); $\sigma = 1.5$, $TAC = 4 - 5ppm$ (□); $\sigma = 1.5$, $TAC = 9 - 10ppm$ (■);. Data with air injection: $\sigma = 1.2$, $TAC = 4 - 10ppm$ (△).

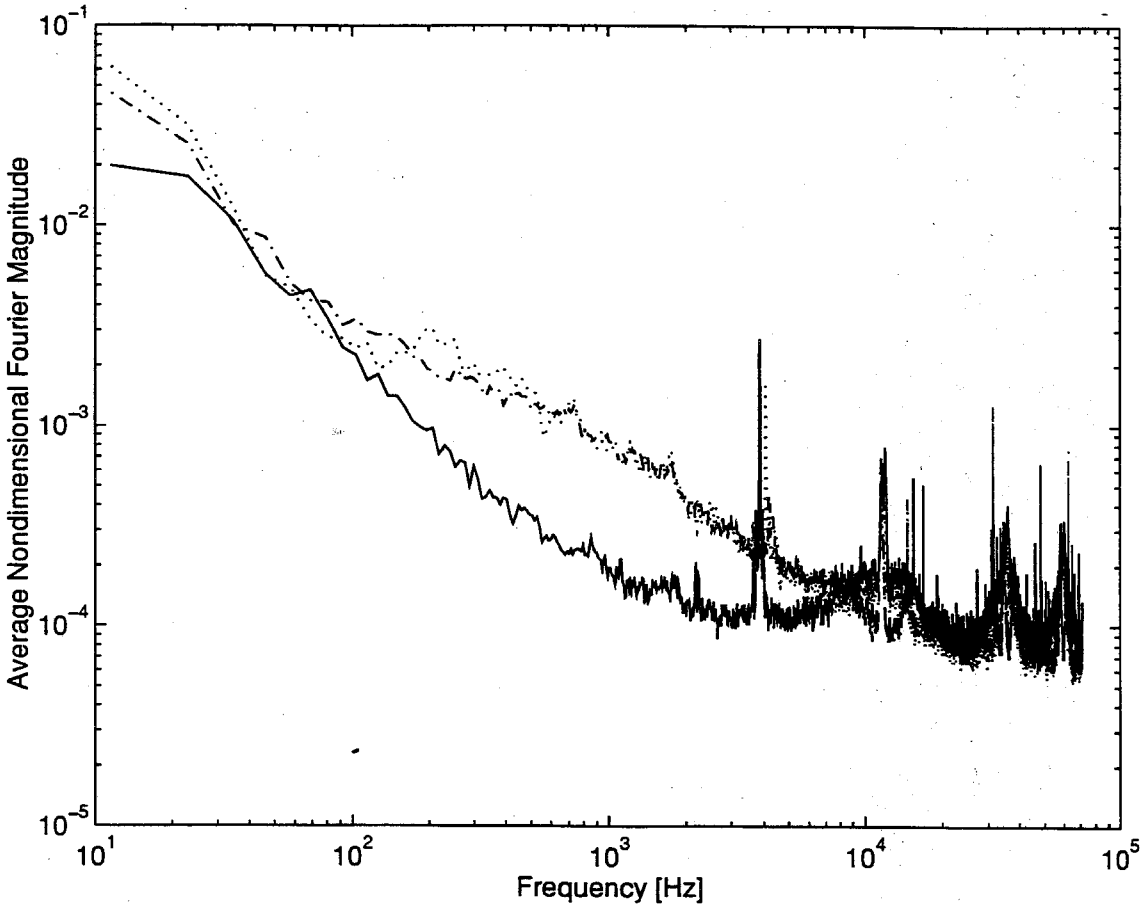

Figure 3.6: Comparison of the normalized spectra of unsteady pressures at three different cavitation numbers: $\sigma = 1.5$ (solid line), $\sigma = 1.2$ (dotted line), and $\sigma = 0.9$ (dash-dot line). Data for $k = 0.7$, $TAC = 7 - 10ppm$, $U = 8m/s$.

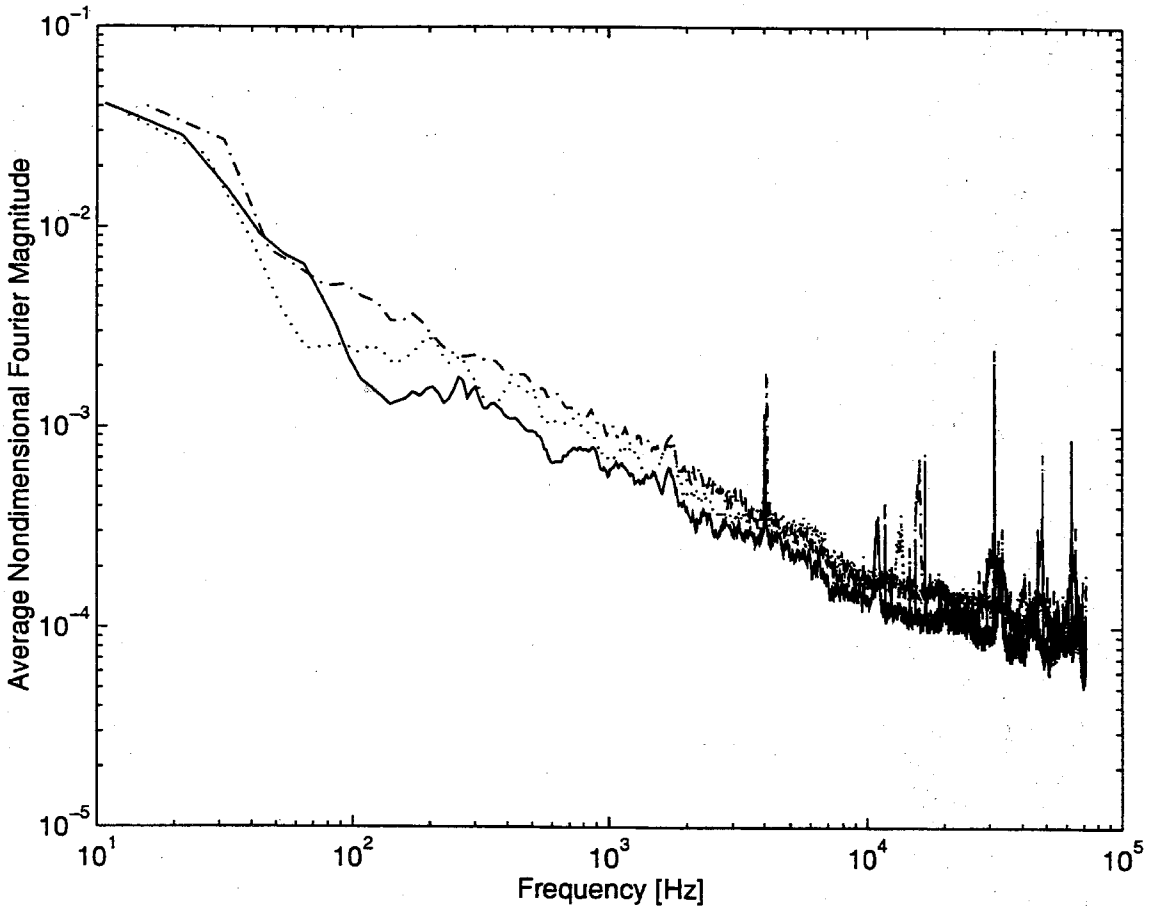

Figure 3.7: Comparison of the spectra of unsteady pressures at three different reduced frequencies: $k = 0.64$ (solid line), $k = 0.8$ (dotted line), and $k = 0.93$ (dash-dot line). Data for $\sigma = 1.2$, $TAC = 4 - 5ppm$, $U = 8m/s$.

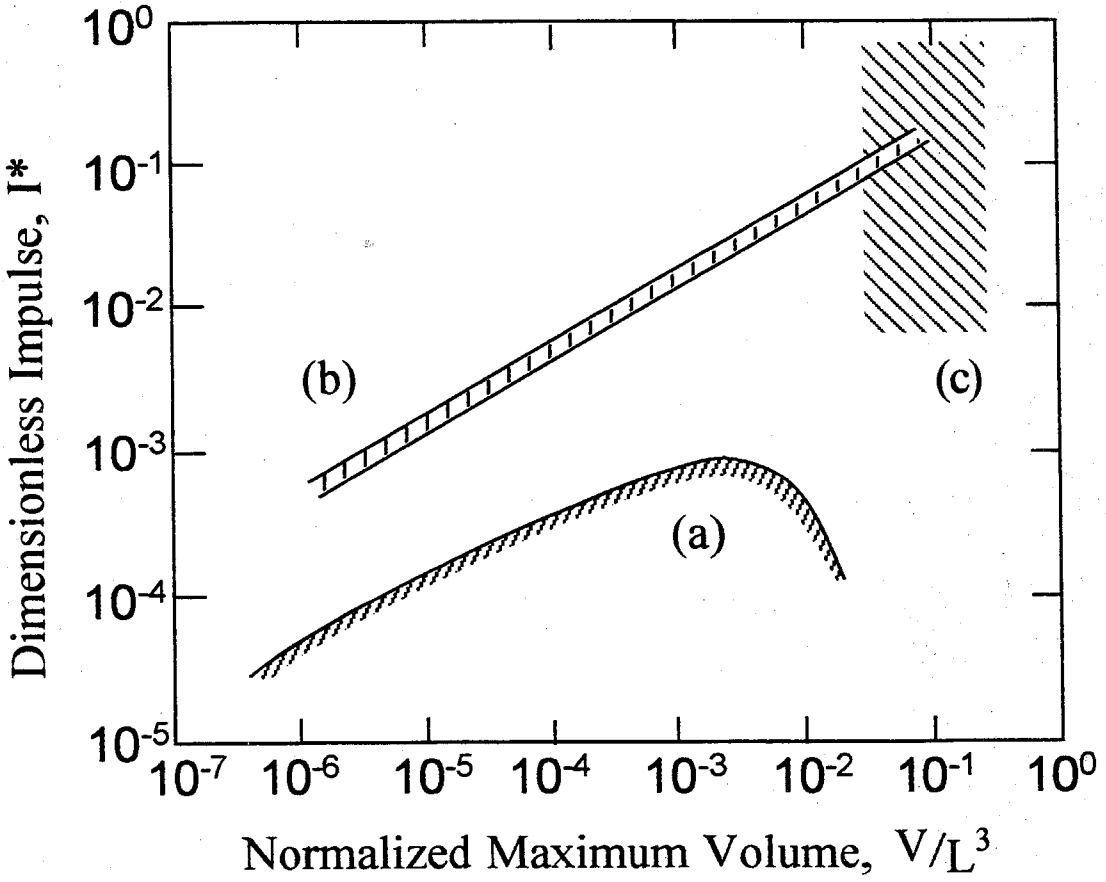

Figure 3.8: Acoustic impulse magnitude ranges as a function of the maximum bubble or cloud volume, for (a) single traveling bubble cavitation (Kuhn de Chizelle *et al.* (1995)), (b) the Rayleigh-Plesset spherical bubble model for the conditions of the aforementioned experiments, and (c) cloud cavitation results from the present experiments.

Chapter 4 Cavitation Observations - Stages of the Cavitation Cycle

Detailed observations of cavity growth and collapse and cloud formation on an oscillating hydrofoil are discussed by several previous authors, including Wade and Acosta (1966), Knapp(1955), Bark (1985), McKenney and Brennen (1994), Shen and Peterson (1978, 1980), Blake *et al.* (1977), Franc and Michel (1988), Hart *et al.* (1990), Kubota *et al.* (1989,1992), Le *et al* (1993), de Lange *et al.* (1994) and Kawanami *et al.* (1996). By viewing the high speed motion pictures taken during the current experiments, a series of stages in the cloud cavitation process can be identified. These stages are depicted schematically in figure 4.1 for a single foil oscillation cycle. In addition, selected frames from a high speed movie of a single foil oscillation cycle are shown in figure 4.2. It should be noted that the description below and the sketches of figure 4.1 are based on a mean angle of attack of 5°. The high speed motion picture depicted in figure 4.2 was taken with the foil oscillating at a mean angle of attack of 7°. Although the same structures are observed in the same order during experiments at both mean angles of attack, the instantaneous angle of attack at which the stage occurs will be different for the two cases.

During that part of the oscillation cycle when the instantaneous angle of attack, α_f, is increasing, cavitation inception occurs in the tip vortex and is soon followed by traveling bubble cavitation in the area of C_{pmin} as can be seen in frame (a) of figure 4.2. The traveling bubble cavitation stage was observed to persist for a longer period of time on the thicker modified NACA 0021 foil than on the NACA 64A309 foil. As the angle of attack increases further, the bubbles coalesce into a single attached

cavitation sheet which attains its maximum length as the angle of attack reaches a maximum. This process is depicted in frames (b) and (c) of figure 4.2. At this point, a re-entrant liquid jet penetrates the attached cavity from the downstream edge and flows toward the leading edge of the foil. This re-entrant jet mechanism was described by Knapp (1955) and further explored in the work of Wade and Acosta (1966), Lush and Skipp (1986), Kubota *et al.* (1992), de Lange *et al.* (1994) and Kawanami *et al.* (1996). The re-entrant jet does not progress uniformly toward the leading edge along the span; the jet penetration is maximum at approximately 30% span (from the base of the foil). This can be seen in photographs (c), (d), (e) and (f) of figure 4.2. The arrow in these frames indicates the frontal edge of the re-entrant jet.

The current observations indicate, however, that the process which occurs *after* the passage of the re-entrant jet is critical. The large pressure pulses on the foil surface, which will be described in greater detail in chapter 5, were detected only after the re-entrant jet had passed the measurement location. The jet proceeds to the leading edge of the foil and, in the process, breaks up the attached sheet cavity into a bubbly mixture which detaches from the foil surface and accelerates downstream. The thickness of the bubbly mixture increases in the region through which the jet passes by a mixing of the vapor/gas contained in the cavity with the surrounding liquid to create a much larger bubbly mixture volume. The break up of the sheet cavity is seen in frames (d) through (g) of figure 4.2 and the detachment of the bubbly mixture from the foil surface begins in frame (h). Local disturbances in the bubbly mixture and variations in the local void fraction are then observed as the mixture is convected toward the trailing edge. The nature of these structures will be addressed in section 5.1. Finally, the remains of the sheet cavity form a cloud of bubbles that undergoes a coherent collapse as it is convected into a region of higher pressure near the foil trailing edge. This collapse can be seen in frames (n) and (o) of figure 4.2. As shown in these frames and discussed in section 5.1, this collapse results in only a

slight change in the cloud radius but a large change in void fraction magnitude and distribution inside the cloud.

These cloud cavitation structures cannot be fully described in two dimensions. As mentioned above, there is a large increase in the thickness of the bubbly mixture, and thus a decrease in the void fraction, after the re-entrant jet passage. This variation is depicted in figure 4.3. This figure contains sketches traced from high speed motion pictures taken both from a profile view through the test section ceiling and a planform view through the test section side wall. The two movies were taken at the same operating conditions, but were not filmed simultaneously. Cycle to cycle variations in the details of the cloud cavitation structure are significant, but the overall structure is quite repeatable. Thus, figure 4.3 presents a general comparison between the structures seen in the planform and the profile at the same point in the foil oscillation cycle.

Sketch (a) of figure 4.3 was taken at an angle of attack of 10°, with the angle of attack, α_f, decreasing. The re-entrant jet has begun to penetrate the sheet cavity and its front is closest to the foil leading edge at a spanwise location approximately 30% from the base of the foil. The thickness of the attached sheet cavitation is on the order of the thickness of the foil. The region near the trailing edge was obstructed during the filming of the profile view, but the position of the re-entrant jet is apparent by the appearance of a bubbly mixture extending out beyond the sheet cavity liquid-vapor interface. As seen in sketch (b), (c) and (d), (α_f = 8.4°, 6.9° and 5.4°, respectively) as the re-entrant jet moves to the foil leading edge, the bubbly mixture expands off the foil surface by a distance of almost a half a chord length. At first however, this expansion only occurs near the 30% span location. In sketches (a) through (e) attached sheet cavitation is still present at other spanwise locations with a thickness on the order of the foil thickness. In sketch (f) (α_f = 3.2°, α_f increasing), the break-up of the attached sheet cavitation into a bubbly mixture is complete. The mixture

continues to expand as it is convected downstream and the individual bubbles of the mixture collapse, (see sketch (g) and (h), $\alpha_f = 4.7°$ and $7.7°$). Traveling bubble cavitation reappears briefly in sketch (g) and is observed in both the profile and planform views. It is also evident in the profile motion picture that the void fraction of the bubbly mixture is significantly lower than the void fraction of the attached sheet cavity.

These profile and planform images are not unlike the description of cloud cavitation on a two-dimensional hydrofoil provided by de Lange *et al.* (1994), Shen and Petersen (1978), Franc and Michel (1988) and Kawanami *et al.* (1996); the most important difference is the large spanwise variation in cavitation structure, thickness and void fraction observed on the three-dimensional hydrofoil of the current experiments.

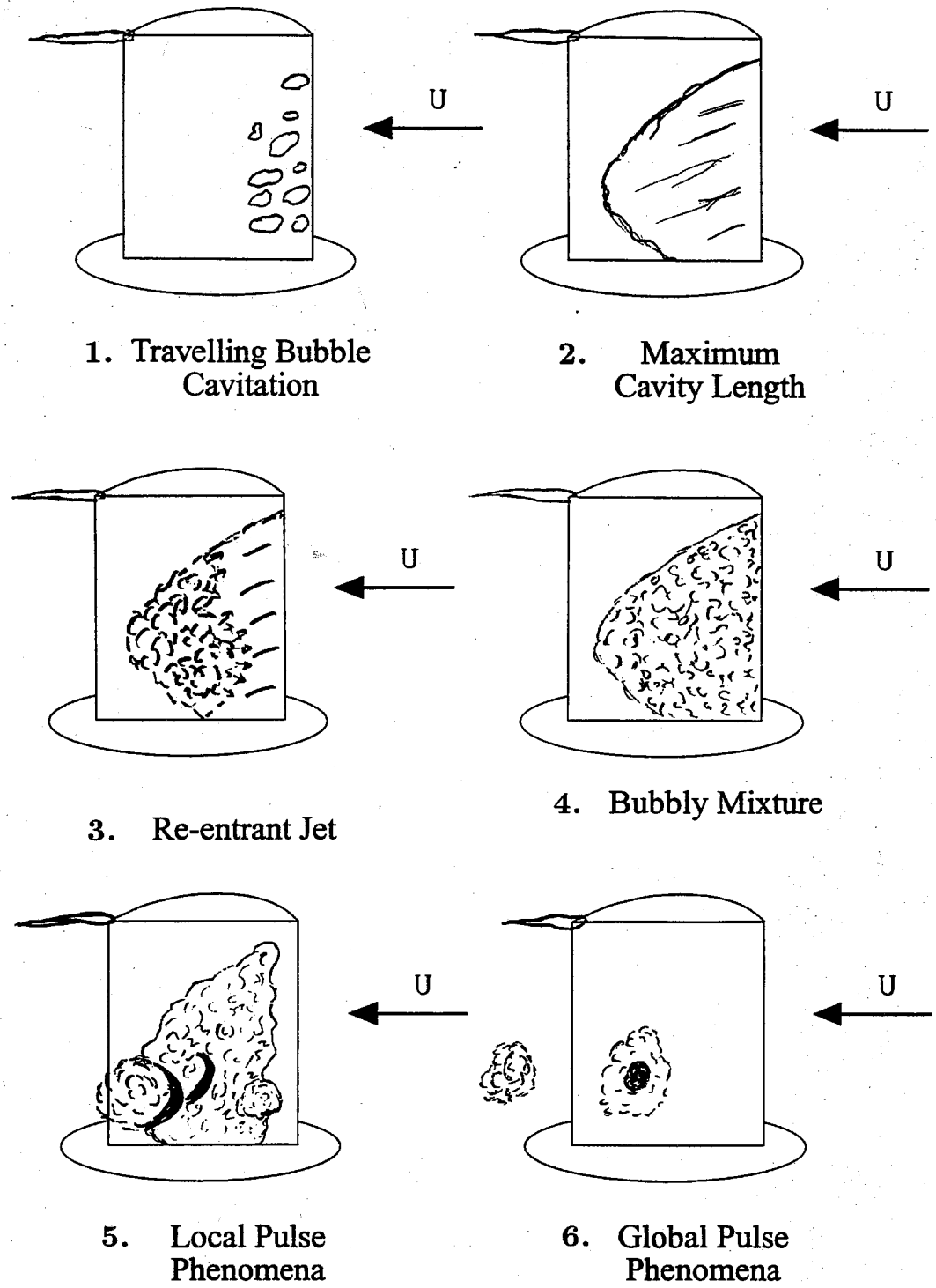

Figure 4.1: Cavitation structures observed during a single oscillation cycle for a mean angle of attack of 5°. The angle of attack increases from sketch 1 to a maximum at sketch 2 and then decreases to a minimum at sketch 5.

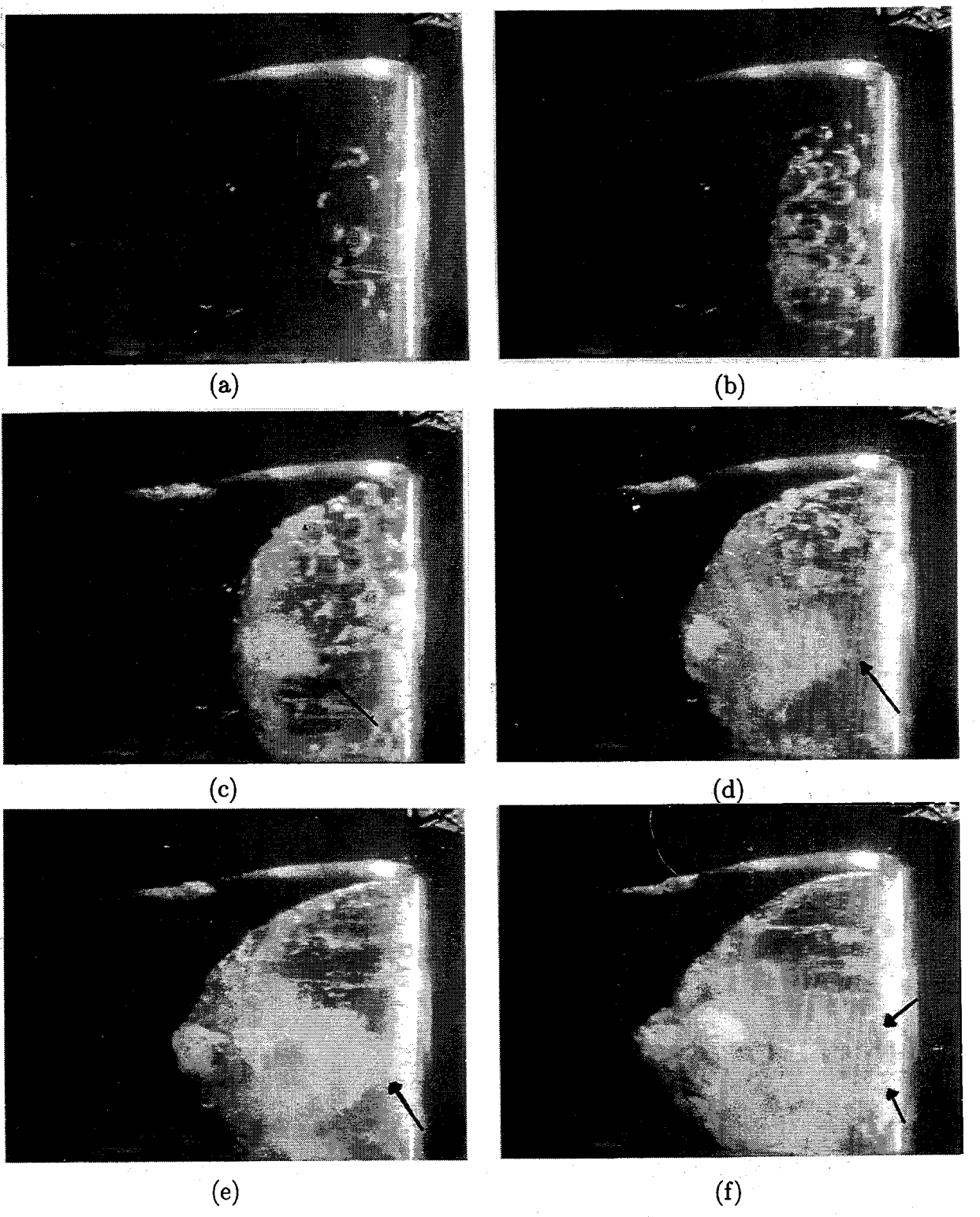

Figure 4.2: Cavitation structures observed during a single oscillation cycle. Selected frames from a high speed motion picture of a single oscillation cycle. Frames are sequential, but not necessarily consecutive. NACA 0021 foil oscillating at $k = 0.7$, $\sigma = 0.95$, $U = 8.5m/s$, $\overline{\alpha_f} = 7°$.

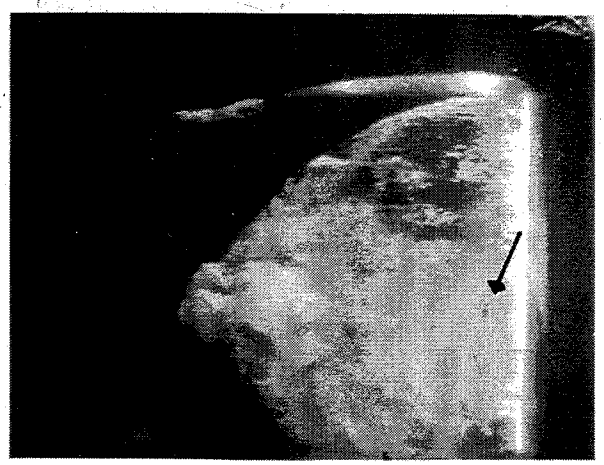

(g)

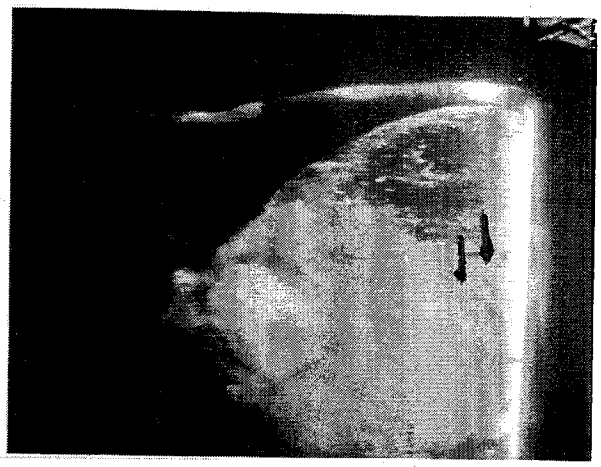

(h)

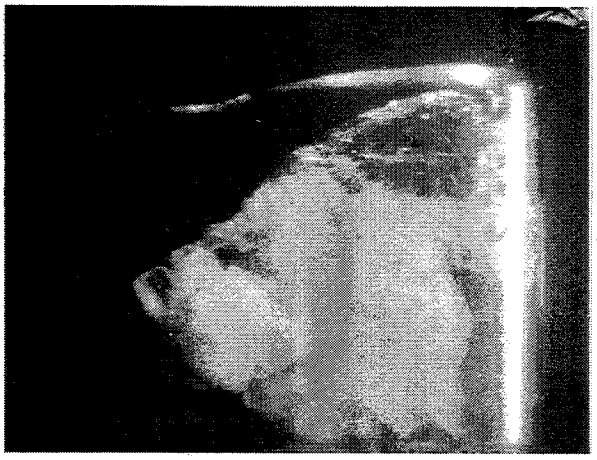

(i)

(j)

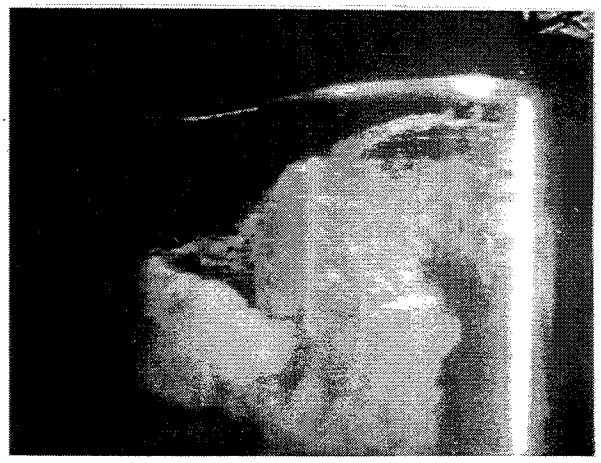

(k)

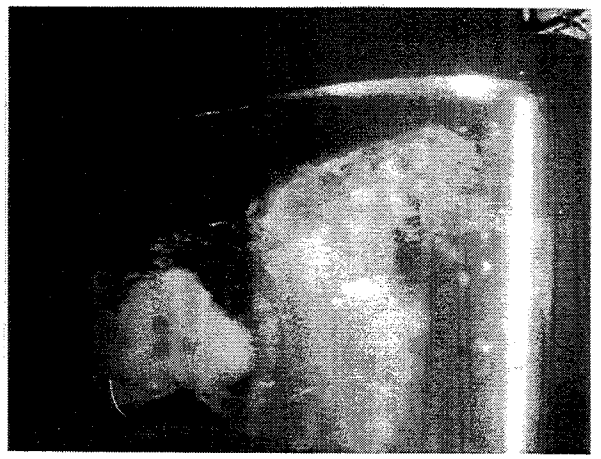

(l)

Cavitation structures observed during a single oscillation cycle. Selected frames from a high speed motion picture of a single oscillation cycle. Frames are sequential, but not necessarily consecutive. NACA 0021 foil oscillating at $k = 0.7$, $\sigma = 0.95$, $U = 8.5m/s$, $\overline{\alpha_f} = 7°$.

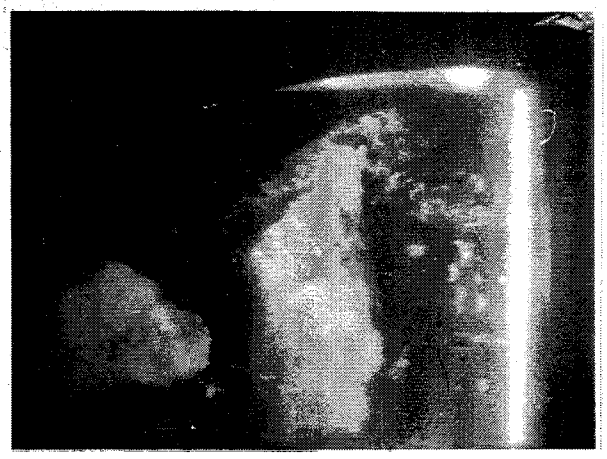

(m)

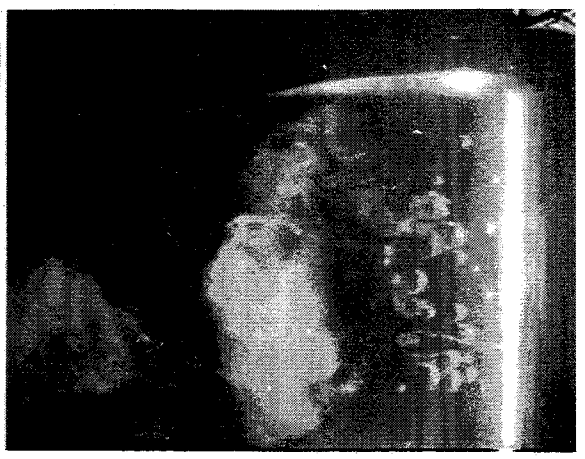

(n)

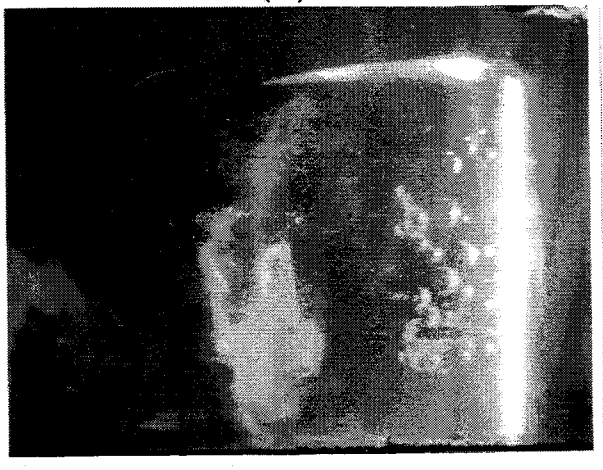

(o)

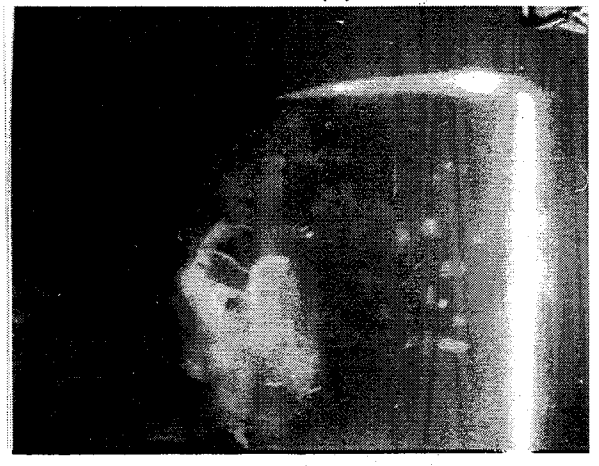

(p)

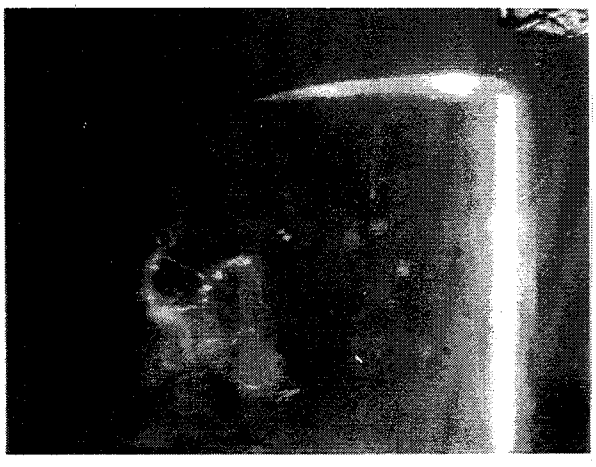

(q)

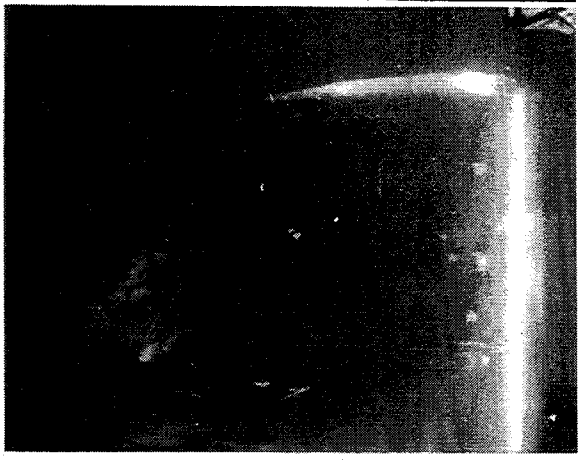

(r)

Cavitation structures observed during a single oscillation cycle. Selected frames from a high speed motion picture of a single oscillation cycle. Frames are sequential, but not necessarily consecutive. NACA 0021 foil oscillating at $k = 0.7$, $\sigma = 0.95$, $U = 8.5m/s$, $\overline{\alpha_f} = 7°$.

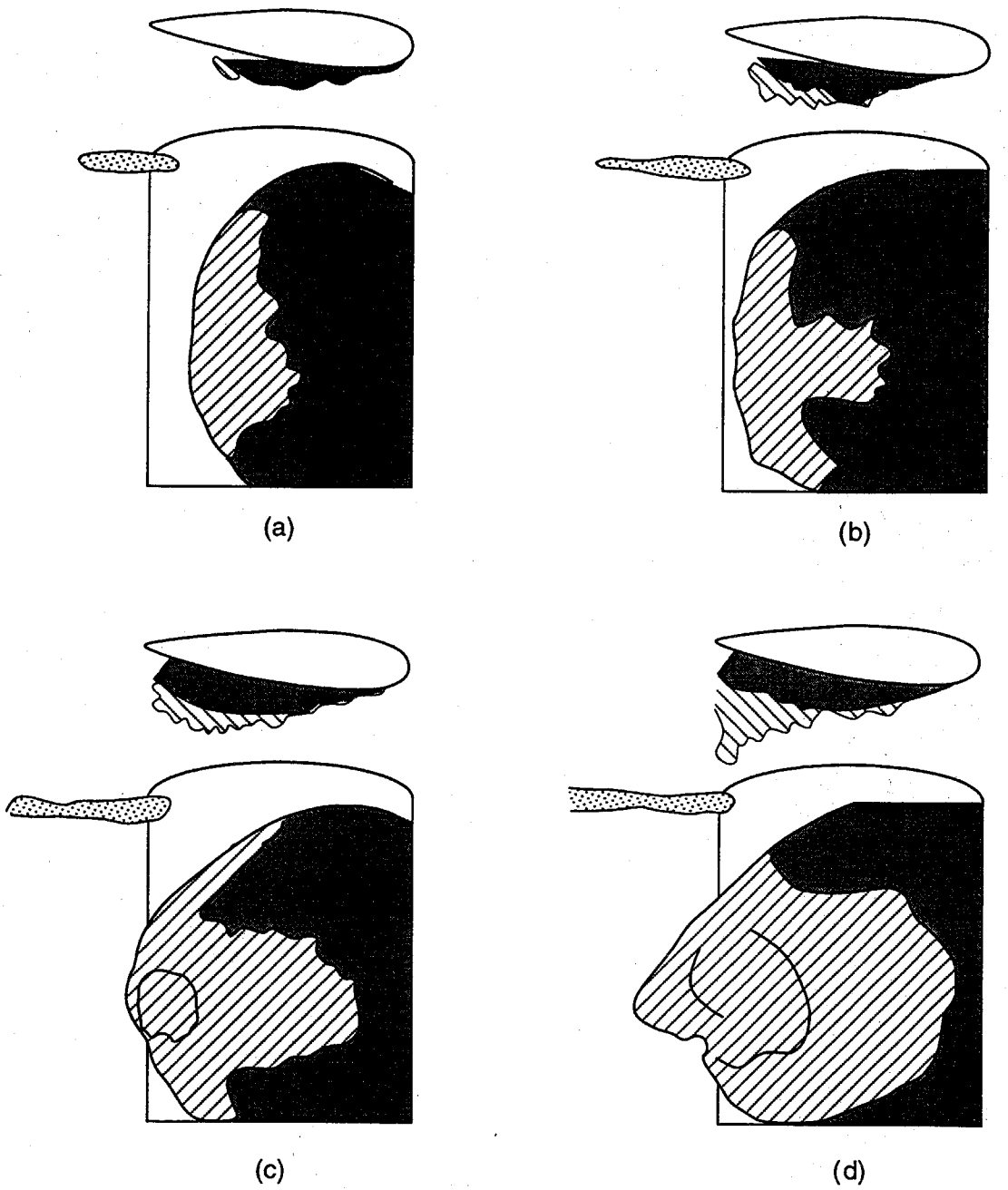

Figure 4.3: Profile and planform sketches of cloud cavitation structures as traced from high speed motion pictures of a single foil oscillation cycle. Shaded areas - sheet cavitation; Hatched areas - bubbly mixture; Dotted areas - traveling bubble or tip vortex cavitation. NACA 0021 foil oscillating at $k = 0.7$, $\sigma = 0.9 - 0.95$, $U = 8.5m/s$, $\overline{\alpha_f} = 7°$.

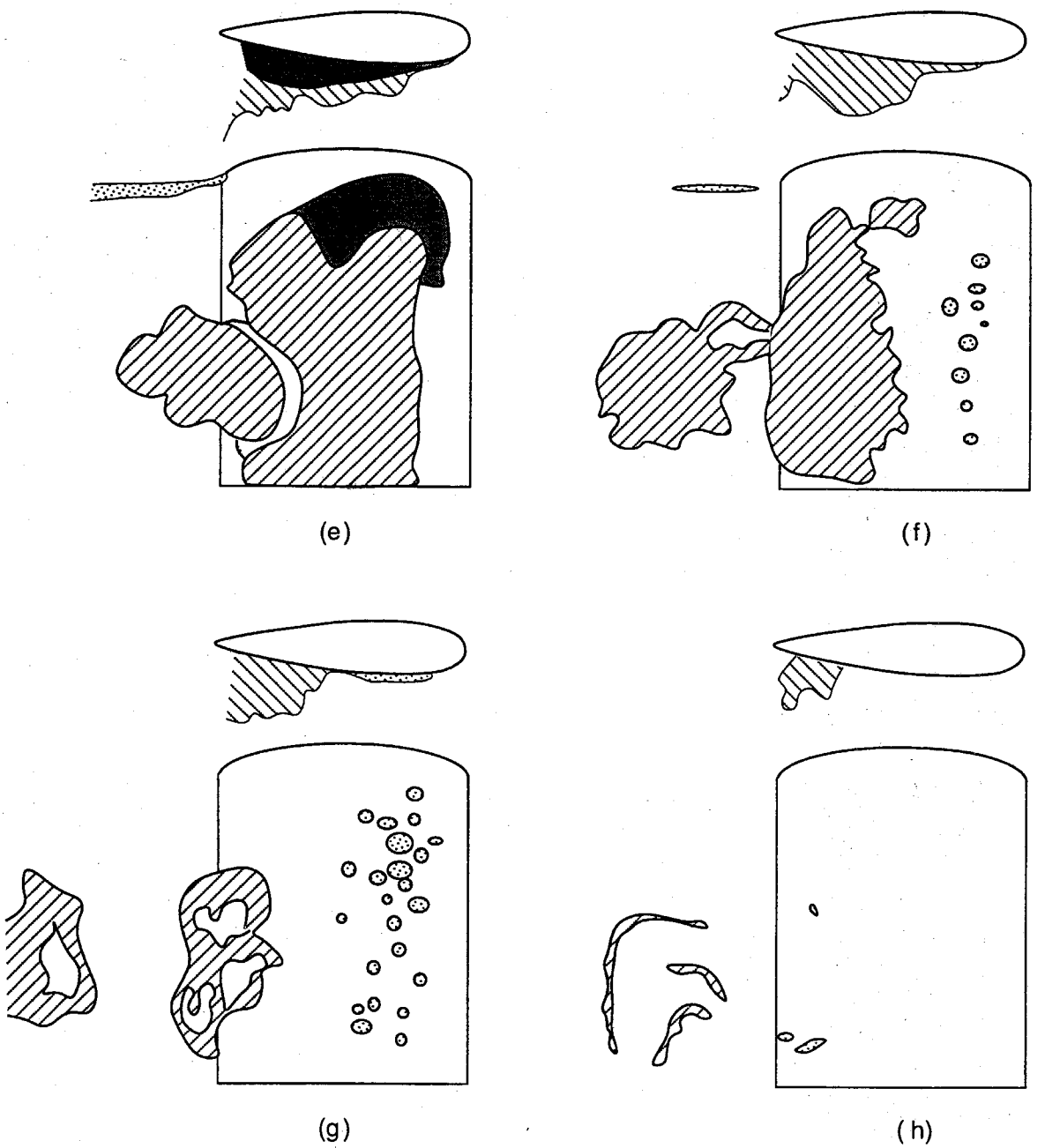

Profile and planform sketches of cloud cavitation structures as traced from high speed motion pictures of a single foil oscillation cycle. Shaded areas - sheet cavitation; Hatched areas - bubbly mixture; Dotted areas - traveling bubble or tip vortex cavitation. NACA 0021 foil oscillating at $k = 0.7$, $\sigma = 0.9 - 0.95$, $U = 8.5m/s$, $\overline{\alpha_f} = 7°$.

Chapter 5 Pressure Pulses due to Cloud Cavitation

The high speed motion pictures taken of cloud cavitation on the NACA 64A309 foil showed the presence of several interesting structures on the suction surface. To investigate these phenomena further, the NACA 0021 hydrofoil was built to obtain measurements of the unsteady surface pressures which could then be correlated with the photographic record of the cavity and its structures. Experiments were performed while oscillating the foil and while holding the foil at a fixed angle of attack. As discussed in section 2.7, the data presented here were obtained from 40 samples at each operating condition where a single sample is defined by either one oscillation cycle or a $0.066sec$ time period in the case of the static foil experiments. The mean angle of attack was 5°, and the oscillation amplitude was 5°. The foil was fixed at an angle of attack of 5° during the static foil experiments. Experiments were performed at cavitation numbers of 0.85, 0.95, and 1.05, at tunnel velocities of $7.5m/s$, $8m/s$ and $8.5m/s$ and at reduced frequencies of 0, 0.76, 1.00 and 1.22. The total air content was was $9.3ppm$ for the oscillating foil experiments and $8.2ppm$ for the static foil experiments.

5.1 Cavitation Structure

A typical set of output signals from the transducers is shown in figure 5.1 which represents a single foil oscillation cycle with the origin corresponding to the maximum angle of attack. The output signals are characterized by very large amplitude pressure

pulses of very short duration. As exemplified by figure 5.1, the magnitudes of these pulses are of the order of tens of atmospheres with typical durations of the order of tenths of milliseconds. As previously described in chapter 3, the radiated acoustic pressure also contains pressure pulses which are illustrated by the bottom trace in figure 5.1. The magnitude of these pulses measured by the transducer in the tunnel floor is only on the order of one atmosphere. The closest approximation to the far field pressure is that measured by the transducer in the ceiling of the tunnel test section; this also contains impulses, but these pulses were of less than $10kPa$ in amplitude. Although these far field measurements are affected by both the directional dependence of the ceiling transducer and the tunnel test section acoustics, it is clear that there are order of magnitude differences in the amplitudes of the pulses measured on the foil, near the cavitating region and in the far field, respectively.

The low frequency variation present in the signal prior to the $0.025sec$ mark and after the $0.05sec$ mark was also observed at high cavitation numbers when the foil was fully wetted. This part of the signal is the result of stresses in the foil which are communicated through the transducer casings. This explanation is supported by the virtually instantaneous propagation of the low frequency disturbance and by the observation of similar signals even when the foil was oscillating in air.

Two different types of pressure pulses were identified and can be illustrated by figure 5.1. The pulses occurring before the $0.04sec$ mark are randomly distributed in time and space and are not repeated from cycle to cycle. These will be referred to as *local* pulses. The pulses located between the $0.04sec$ and $0.05sec$ marks occur virtually simultaneously, are of higher amplitude and are repeated each cycle. These will be referred to as *global* pulses; they produced substantial far-field noise and the location of the global impulses relative to the foil oscillation was quite repeatable.

The distinction between these two types of pressure pulse can be further elucidated by examining the high speed movies. By synchronizing the high speed movies and

the transducer data acquisition, it is possible to determine exactly which cavitation structures are responsible for the generation of the large amplitude pressure pulses.

Two different types of structures were correlated with the presence of local pulses. The first such structure is depicted in photographs (a) through (c) of figure 5.2 and the two photographs of figure 5.3. These structures are crescent shaped regions of low void fraction. They appear randomly in the bubbly mixture which remains after the passage of the reentrant jet. The existence of this type of transient flow structure is a common occurrence during the detachment of a cavitation cloud from a sheet cavity as noted by Shen and Peterson (1978), Bark (1985), and McKenney and Brennen (1994). The two photographs of figure 5.3 show how complicated these flow structures can be, while photographs (b) and (c) of figure 5.2 illustrate the common simultaneous observation of more than one crescent shaped structure.

An examination of the high speed movies synchronized with acoustic data for over 40 oscillation cycles indicated the presence of a local pulse whenever the downstream edge of such a low void fraction structure passed over a transducer; the pulse is thus registered when transitioning from a region of high void fraction to low void fraction. These observations are consistent with those of Shen and Peterson (1978). The downstream boundary of these low void fraction regions are observed to propagate into the bubbly mixture as the region expands. The first local pulse registered by transducers # 1 and #3 in figure 5.1 were caused by the passage of the downstream edge of one of these crescent shaped regions of low void fraction. Small crescent shaped cavitation structures are also visible near the leading edge of the foil in frames (f), (g) and (h) of figure 4.2, as indicated by the arrows.

The second type of flow structure which was correlated with the occurrence of a local pulse is shown in photograph (d) of figure 5.2. The movie and pressure data consistently showed the presence of a local pulse when the upstream boundary, or leading edge, of the detached bubbly mixture passed over a transducer; thus these

phenomena will be referred to as leading edge structures. These structures are created when the sheet cavity detaches from the foil. As with the first kind of local pulse, this second type is observed during a transition from a region of high void fraction to a region of low void fraction. The transitions which cause both types of local pulses are discrete and geometrically coherent.

This leading edge structure is also clearly evident in photographs (h) through (m) of figure 4.2. Figure 5.4 depicts the transducer output corresponding to the photographs of figure 4.2. The large local pulse detected by transducer #1 just after the $0.03sec$ mark occurs between photographs (i) and (j) of figure 4.2. The distinct upstream edge of the bubbly mixture passes over transducer #1 between these two frames of the high speed movie. The second local pulse registered by transducer #1 in figure 5.1 was also caused by the passage of a leading edge structure.

It should be noted that a local pulse was not necessarily detected in the acoustic data each time either a crescent shaped region or a leading edge structure passed over a transducer. For example, the leading edge structure evident in the photographs of figure 4.2 generates a very large local pulse when it passes over transducer #1 but no large pulse is detected when the same structure passes over transducer #2. The lack of a local pulse when such a distinct structure was present was the exception rather than the rule, however. Conversely, however, the presence of a large local pulse in the acoustic data would be accompanied by one of these structures in the synchronized high speed motion pictures with very few exceptions.

The cause of the global pulse is also evident in the high speed motion pictures. Figure 5.5 depicts four consecutive frames from one such movie and figure 5.6 contains the corresponding synchronized acoustic data. The cavitation cloud which is the remnant of the attached sheet cavity undergoes a rapid and coherent collapse between frames (b) and (c) of figure 5.5. These two frames were taken only $2msec$ apart and correspond to the region marked by the vertical lines in figure 5.6. The collapse of this

region radiates a pressure pulse which is detected by all of the foil transducers and the transducer located in the tunnel floor. The delay in the occurrence of the global pulse in the output of transducer #1 and #2 may be attributed to the presence of traveling bubble cavitation near the leading edge of the foil. The presence of a bubbly mixture near these transducers will cause a local decrease in the sonic speed.

A global collapse is also observed between photographs (n) and (o) of figure 4.2. The large pulses detected by all four foil transducers and the transducer in the floor just before the $0.05sec$ mark in figure 5.4 occurs between these two photographs of figure 4.2. An even better example of a global event in the transducer output is seen just before the $0.05sec$ mark in figure 5.1. This pulse, which was detected virtually simultaneously by all five transducers, was caused by a large coherent cloud collapse similar to the one depicted in figure 5.5.

It should be noted that all of these global cloud collapses do not involve large changes in the overall dimensions of the cloud; rather collapse involves large changes in the void fraction distribution within the cloud. Rapid and non-uniform changes in the void fraction occur throughout the cloud interior as shown in figure 5.5. Also, the global collapse often generates multiple pulses in quick succession. These multiple pulses can be seen in the output from transducers #1, #4 and the floor transducer in figure 5.1, from transducer #4 in figure 5.4 and from transducer #4 in figure 5.6. An explanation for the dynamics of the global cloud collapse and for the existence of multiple radiated pressure pulses is given in chapter 6 section 6.2.

5.2 Static Foil Experiments

A typical set of output signals from the transducers during the static foil experiments is shown in figure 5.7. The magnitude of the observed pulses is considerably lower than those measured while the foil was oscillating; they were typically only a few at-

mospheres in amplitude. There was a substantial reduction in the radiated noise, and only local events were observed. The shedding of bubble clouds from the downstream edge of the attached cavity was not characterized by any particular frequency; rather the clouds were detached in a continuous process. It should be noted that the mean flow conditions were steady in the current experiments. More severe noise production can be expected in static foil experiments performed with periodically fluctuating mean flow conditions, such as the experiments of Kawanami *et al.*.

Four consecutive frames from a high speed motion picture taken at the same time as the acoustic data of figure 5.7 are shown in figure 5.8. While the cavitation structure is smaller and less coherent than the cloud cavitation observed on the oscillating foil, local events are still discernible on the foil surface. A crescent shaped region of low void fraction can be observed propagating from the $\frac{1}{4}$ chord position to the midchord in these four frames near the transducer location along the span. The two local pulses seen in the output from transducers #1 and #2 between the $0.035sec$ and $0.045sec$ mark in figure 5.7 were caused by the passage of the downstream boundary of this crescent shaped region. This flow structure is marked by the arrows in figure 5.8.

5.3 Impulse Measurements

The experimental results depicted in figures 5.9 through 5.15 illustrate the variation of the average acoustic impulses with reduced frequency, cavitation number and tunnel velocity for both the static and the oscillating foil. In each figure the calculated impulses are presented for both the global and local pressure pulses detected by the four foil mounted transducers and the transducer located in the tunnel test section floor. Each average acoustic impulse presented in the figures is based on data collected during 40 foil oscillation cycles.

Figure 5.9 illustrates the variation in the magnitudes of the local and global im-

pulses with reduced frequency at a constant cavitation number, σ, and tunnel velocity, U. Global impulses are virtually non-existent with the static foil under the conditions of figure 5.9 which result in nominally steady partial cavitation on the static foil. On the oscillating foil, there appears to be a broad range of reduced frequencies around unity in which the coherent collapses associated with global pulses are triggered. As seen in figure 5.9, there also appear to be specific frequencies like $k = 0.76$ and $k = 1.22$ which seem to produce the maximum global impulses. This general pattern of variation with reduced frequency is similar to that seen in the radiated noise by McKenney and Brennen (1994) and also in the parametric study results of chapter 3; note that the radiated noise measured by the floor transducer is only substantial when global pulses are present. We also note from figure 5.9 that the spatial distribution of the measured impulses is similar for all reduced frequencies; they tend to be larger at mid-chord where the sheet cavitation breaks up and collapses.

Data was also taken with the foil oscillating at $k = 0.23$ due to the relevance of this reduced frequency to surface combatant vessel applications. The results for this value of k are shown in figure 5.10, along with the data from figure 5.9. Data was not obtained from transducer #4 at $k = 0.23$ since the number of sampled channels had to be reduced to acquire an entire oscillation cycle in the $64k$ memory buffer of the RC card at this low oscillation frequency. Very large local impulses were measured at this frequency, but, similar to the results for $k = 1.00$, global pulses were infrequently noted. Data was taken at two different mean angles of attack during the $k = 0.23$ experiments and the two conditions are compared in figure 5.11. While the total impulse increases at every transducer location as $\overline{\alpha_f}$ increases from 5° to 7° the global pulses are virtually absent from the data at the higher mean angle of attack. It is also interesting to note that the spatial distribution remains unchanged as the mean angle of attack is varied.

Figures 5.12 and 5.13 illustrate the variations in the impulses with the cavitation

number, σ, for the static and oscillating foils, respectively. With the static foil, the local impulses appear rather suddenly when σ is reduced below unity. The largest impulses occur near transducer #2, close to the cavity closure region; however, as σ is decreased to 0.85 the values at #3 increase as the cavitation collapse extends to that location. Le *et al.* (1993) also noted that the largest pulses on their static foil occurred near cavity closure.

When the foil is oscillating, the global impulses produced are also very sensitive to changes in cavitation number with the largest global impulses occurring in the middle of the cavitation number range. A similar effect was detected in the radiated impulses by McKenney and Brennen (1994) and Reisman *et al.* (1994), but the occurrence of cloud cavitation in the present experiments is more sensitive to changes in σ, perhaps due to the larger thickness of the NACA 0021 foil.

It is important to emphasize that extremely large local pressure pulses occur at cavitation numbers which do not produce global pulses. An average local acoustic impulse in excess of $0.025kPa.s$ is observed on #2 in figure 5.13 at $\sigma = 0.85$. This flow condition is characterized by sheet cavitation which extends well beyond the trailing edge of the foil and does not produce large radiated pressure pulses outside of the cavitating region.

Both with the static foil and with the oscillating foil (at high cavitation numbers), large local impulses occur on the foil surface without any substantial radiated impulse being registered by the floor transducer. This suggests that significant cloud cavitation damage could occur on a foil which is not exhibiting large acoustic radiation. Conversely, global pulses always produce substantial radiated noise.

The effects of the magnitude of the tunnel velocity are illustrated in figures 5.14 and 5.15 for the static and oscillating foils, respectively (in the latter case, since the foil oscillation frequency was held constant at $12.7Hz$, there is also a small variation in the reduced frequency as the tunnel velocity changes). With the static foil, the local

impulses increase rapidly with increasing velocity as one would expect since cavitation noise normally scales with the velocity raised to some large power. Note again the predominance of events near transducer #2. The total impulse also increases with increasing tunnel velocity when the foil oscillates, as shown figure 5.15. This increase occurs at every measuring location with the single exception of the value measured by the #2 transducer at $U = 8.5m/s$.

5.4 Global Pulse Propagation

By examining the time delays in the global pulse signals from the five transducers (four foil surface transducers and the floor transducer) it was possible to extract some information on the location of the origin of the global pulses and on the speeds of propagation of those pulses through the inhomogeneous environment which exists near the surface of the hydrofoil at the time of the global cloud collapse. This was accomplished by measuring the time intervals between peak occurrences in the transducer outputs for 41 events observed at one particular flow condition. The results of these calculations are shown in figure 5.16. The bar graphs represent the speeds of propagation between neighboring transducers as calculated from the observed time intervals (the one on the right is the calculated speed between #4 and the floor transducer, #F). In all cases, the propagation speeds are a fraction of the sonic speed in either the pure liquid or pure vapor phase. The speeds calculated for the first two intervals are approximately 3.5 times as fast as those measured for the two downstream intervals. Since the sonic speed can be substantially slower in a bubbly mixture than in the pure liquid phase, this difference is consistent with the void fraction distribution observed immediately after global cloud collapse for the experiments with a mean angle of attack of 5°. As shown in figure 4.1, the void fraction increases sharply downstream of the third foil transducer since the sheet cavitation remains have been

carried away from the leading edge of the foil prior to the global cloud collapse.

The approximate origins of the global pulses were calculated by noting which transducer registered the earliest global pulse. The results of this tabulation are depicted by the line in figure 5.16. The global pulses most frequently originated near the fourth foil transducer; this is consistent with the high speed movie observations (e.g. figure 5.5).

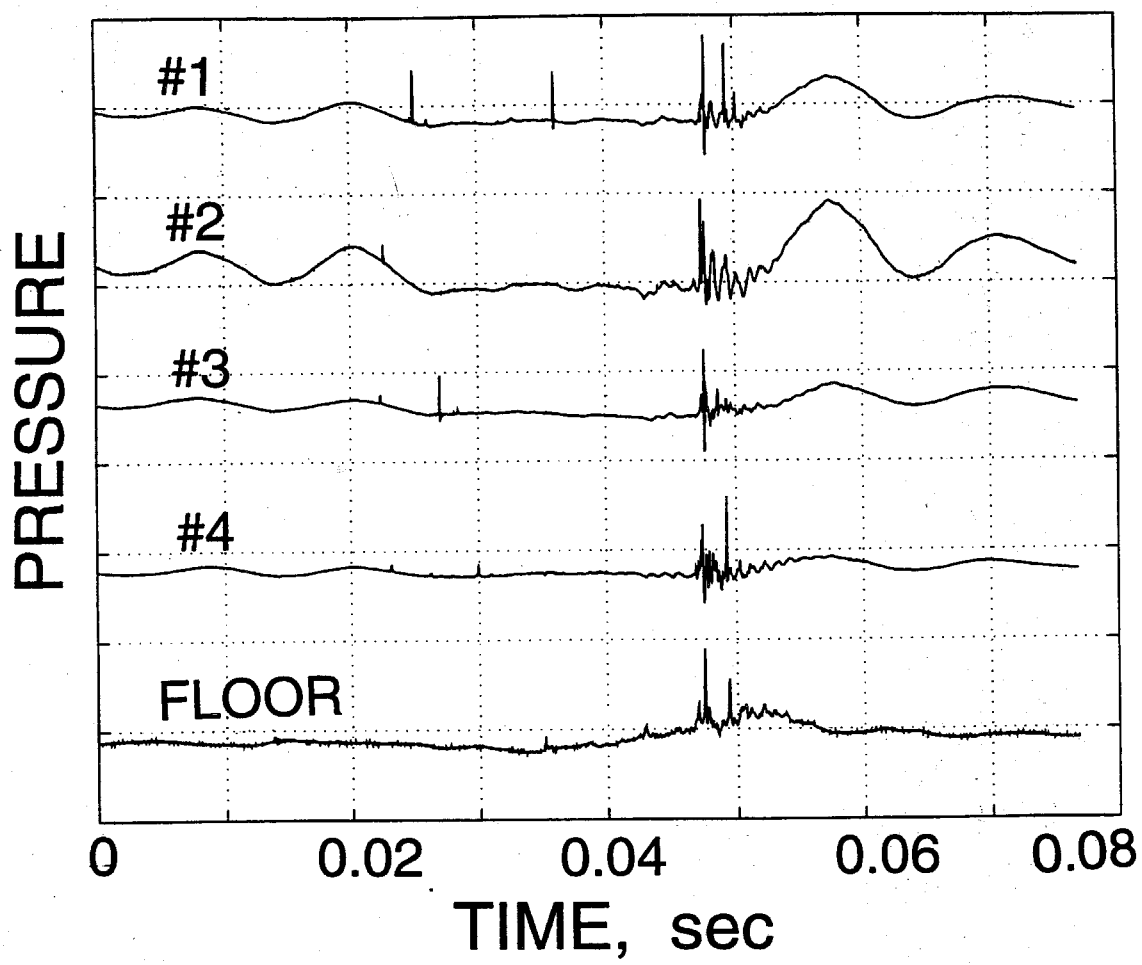

Figure 5.1: Typical surface and far field transducer output during a single foil oscillation cycle. The top four traces are from the foil surface transducers and are numbered from the leading edge. The bottom signal is from the transducer mounted in the tunnel floor. The vertical axis scale is 1 $MPa/div.$ for the foil surface transducers and 100 $kPa/div.$ for the floor transducer. This typical data is for $\sigma = 0.95$, $k = 0.78$, $U = 8m/s$ and $\overline{\alpha_f} = 5°$.

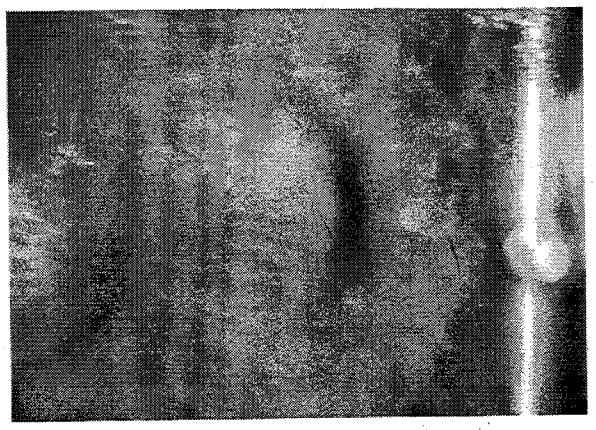

(a)

(b)

(c)

(d)

Figure 5.2: Local pulse structures. Photographs (a) to (c) depict crescent shaped flow structures of low void fraction. Photograph (d) depicts a leading edge type event. Field of view consists of the transducer area of the NACA 0021 foil. Flow is from right to left with $\sigma = 0.9$, $k = 0.71$, $U = 8.5m/s$ and $\overline{\alpha_f} = 7°$.

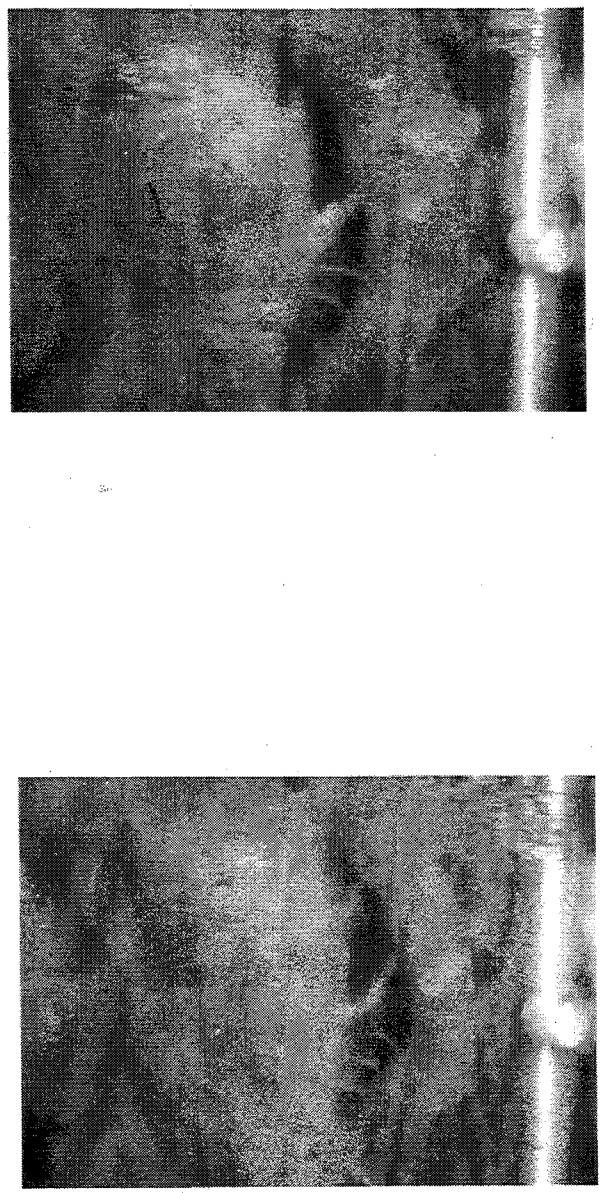

Figure 5.3: Additional crescent shaped flow structures of low void fraction. Field of view consists of the transducer area of the NACA 0021 foil. Flow is from right to left with $\sigma = 0.9$, $k = 0.71$, $U = 8.5m/s$ and $\overline{\alpha_f} = 7°$.

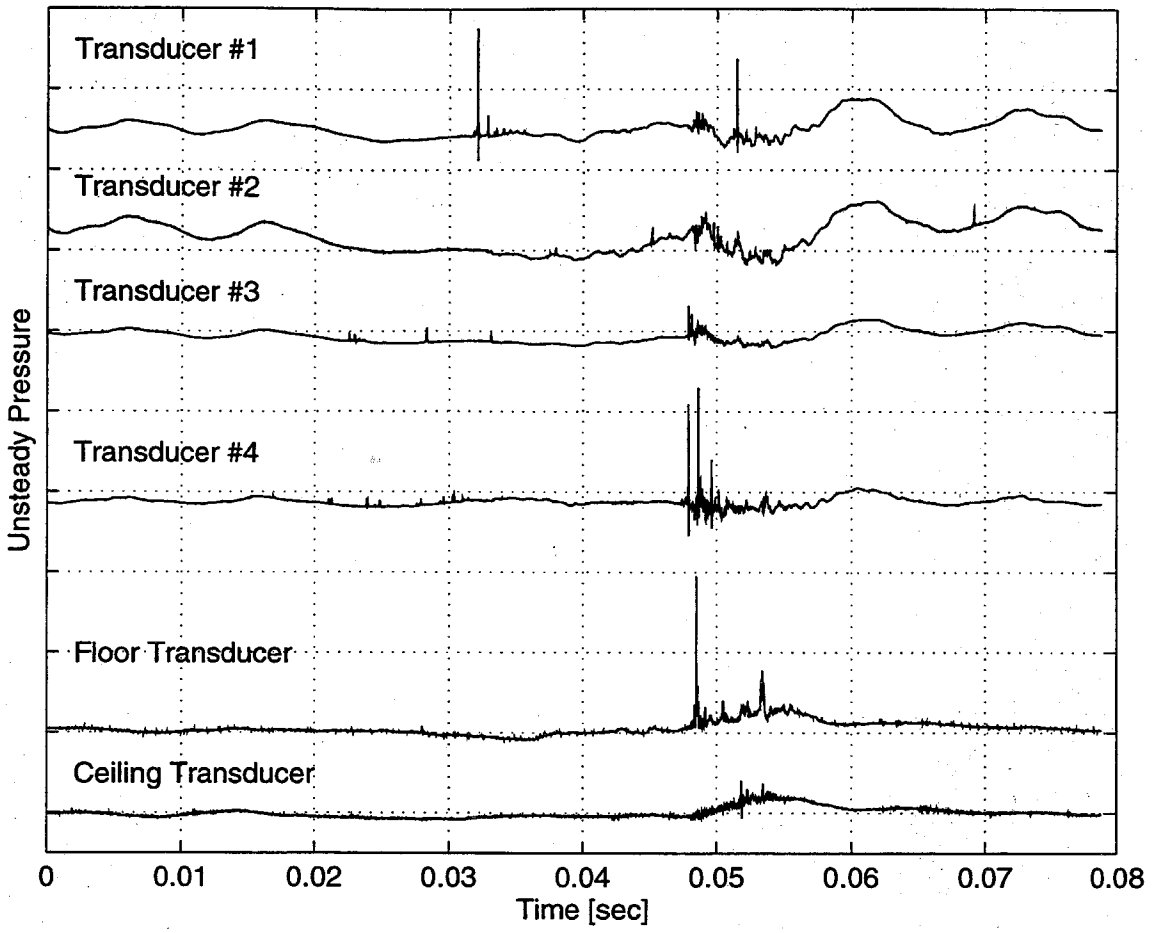

Figure 5.4: Transducer output corresponding to the single oscillation cycle depicted in the photographs of figure 4.2. The vertical axis scale is $1MPa$ per division for the foil surface transducers and $100kPa$ per division for the floor and ceiling transducers. Data for $\sigma = 0.95$, $k = 0.71$, $U = 8.5m/s$ and $\overline{\alpha_f} = 7°$.

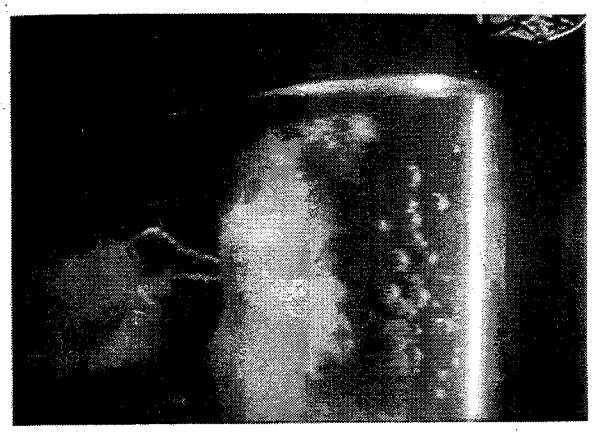

(a)

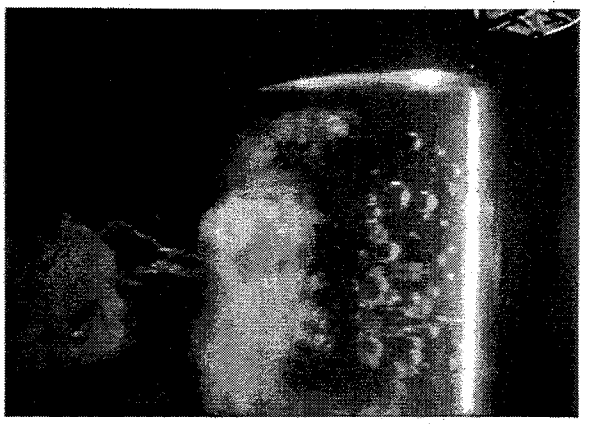

(b)

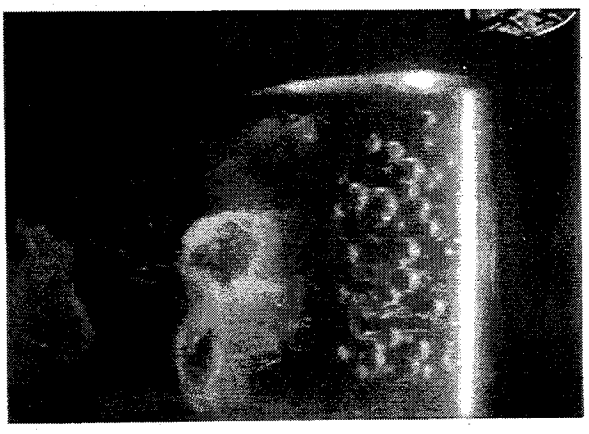

(c)

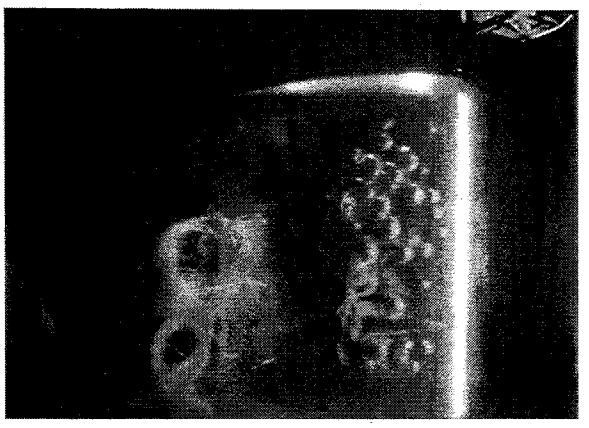

(d)

Figure 5.5: Global cloud collapse. Consecutive high speed movie frames taken during the marked time interval of figure 5.6. Data for $\sigma = 0.95$, $k = 0.71$, $U = 8.5m/s$ and $\overline{\alpha_f} = 7°$

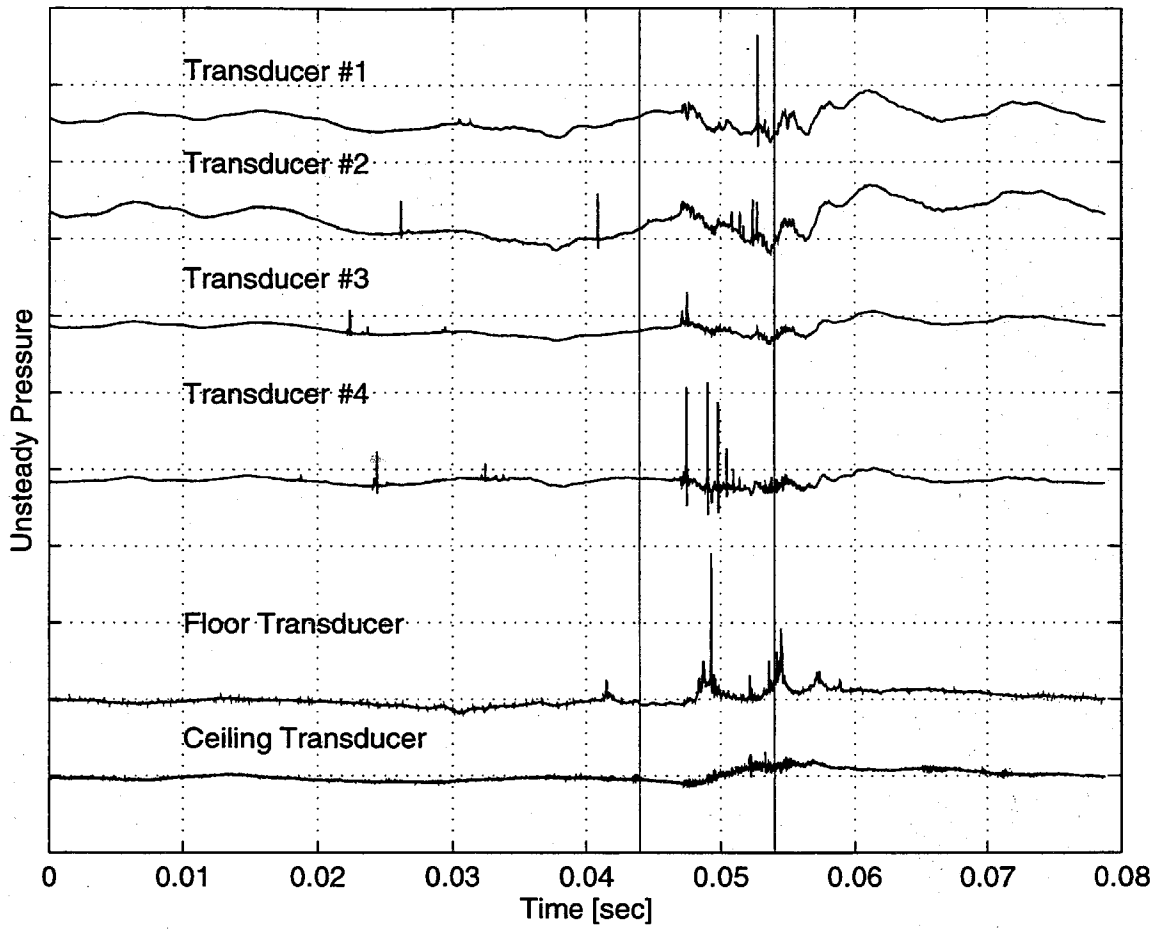

Figure 5.6: Transducer output corresponding to the global collapse photographs of figure 5.5. The vertical axis scale is $1MPa$ per division for the foil surface transducers and $100kPa$ per division for the floor and ceiling transducers. Data for $\sigma = 0.95$, $k = 0.71$, $U = 8.5m/s$ and $\overline{\alpha_f} = 7°$.

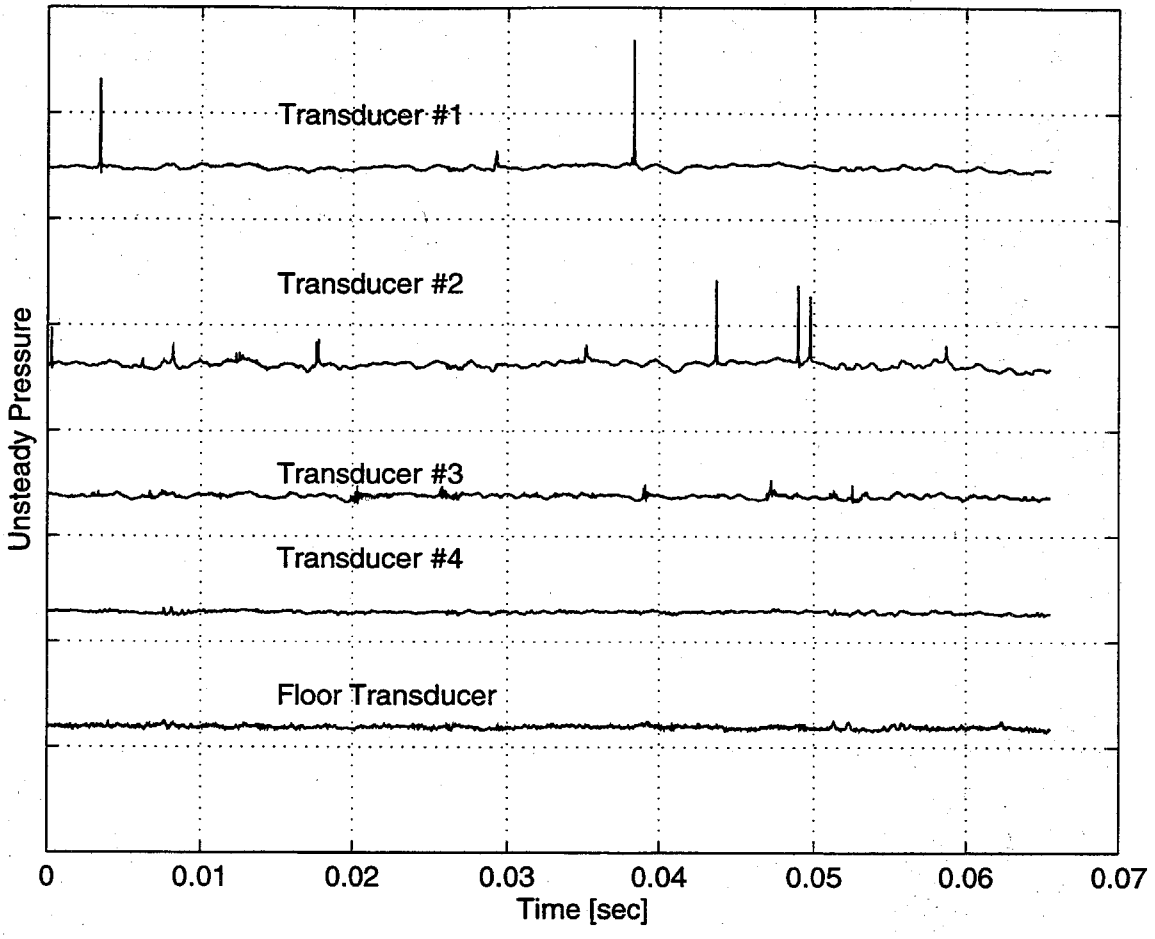

Figure 5.7: Typical transducer output during static foil experiments. Data corresponds to the photographs of figure 5.8. The top four traces are from the transducers mounted on the foil and are numbered from the leading edge. The bottom signal is from the transducer mounted in the tunnel floor. The vertical axis scale is $500kPa$ per division for the foil surface transducers and $50kPa$ per division for the floor transducer. This typical data is for an angle of attack of 5°, $\sigma = 0.95$, $U = 8.5m/s$.

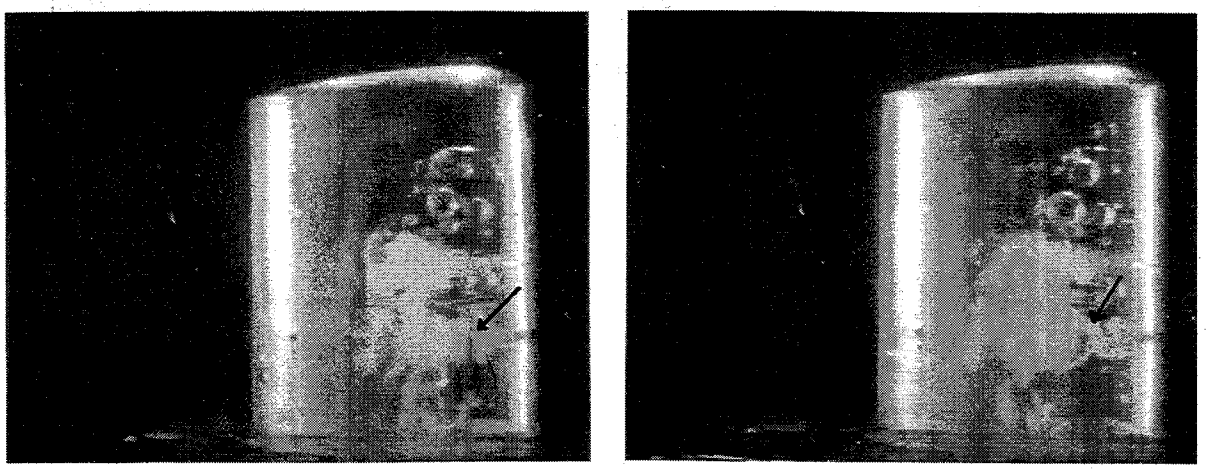

(a) (b)

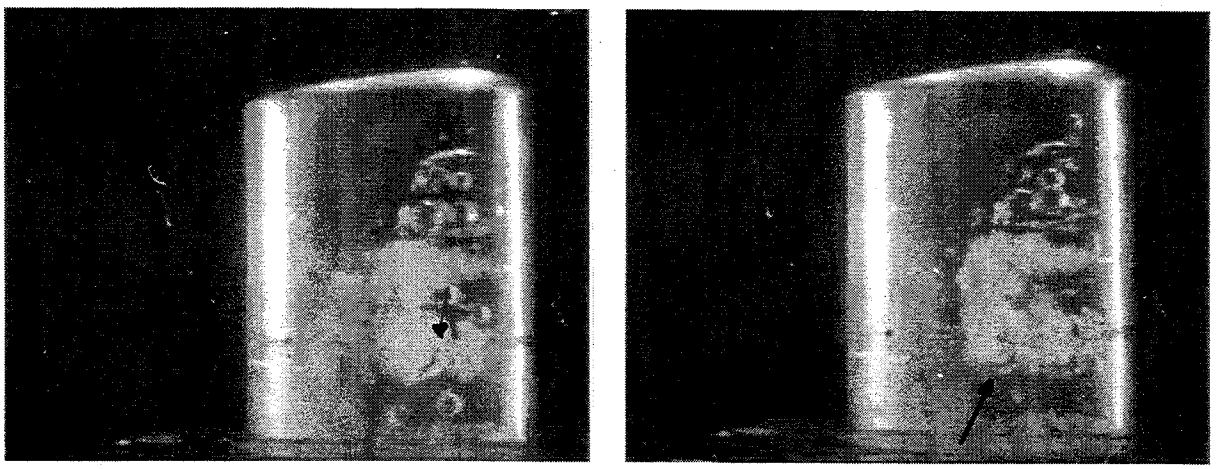

(c) (d)

Figure 5.8: Consecutive high speed movie frames taken during static foil experiments. Flow conditions were: an angle of attack of 5°, $\sigma = 0.95$, $U = 8.5m/s$.

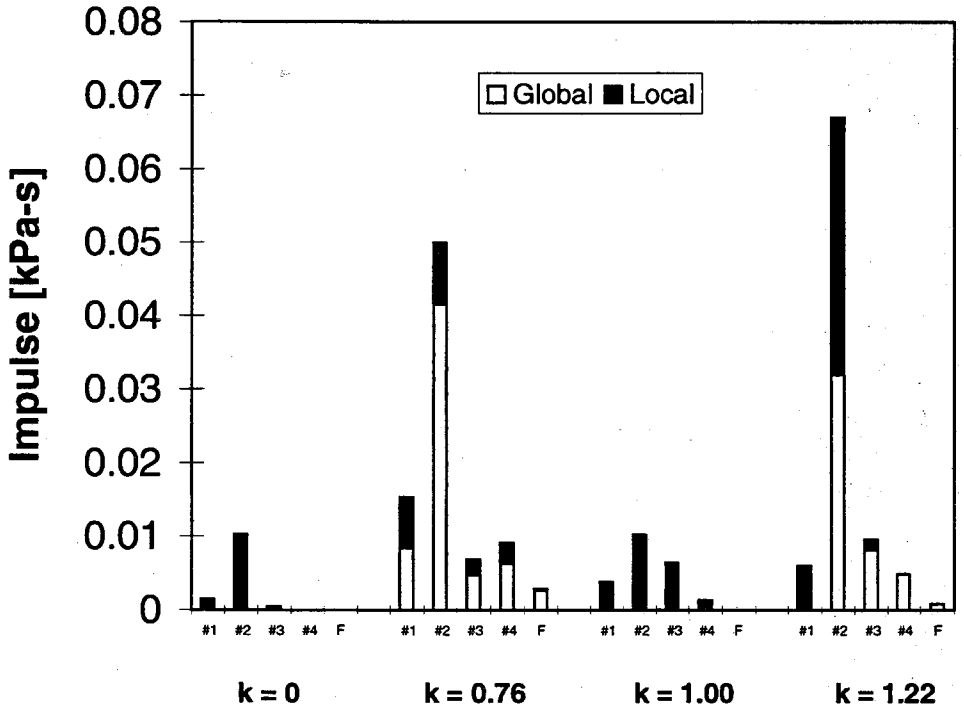

Figure 5.9: Effect of the reduced frequency, k, on the impulse, I. Data for $\sigma = 0.95$, $U = 8m/s$ and $\overline{\alpha_f} = 5°$

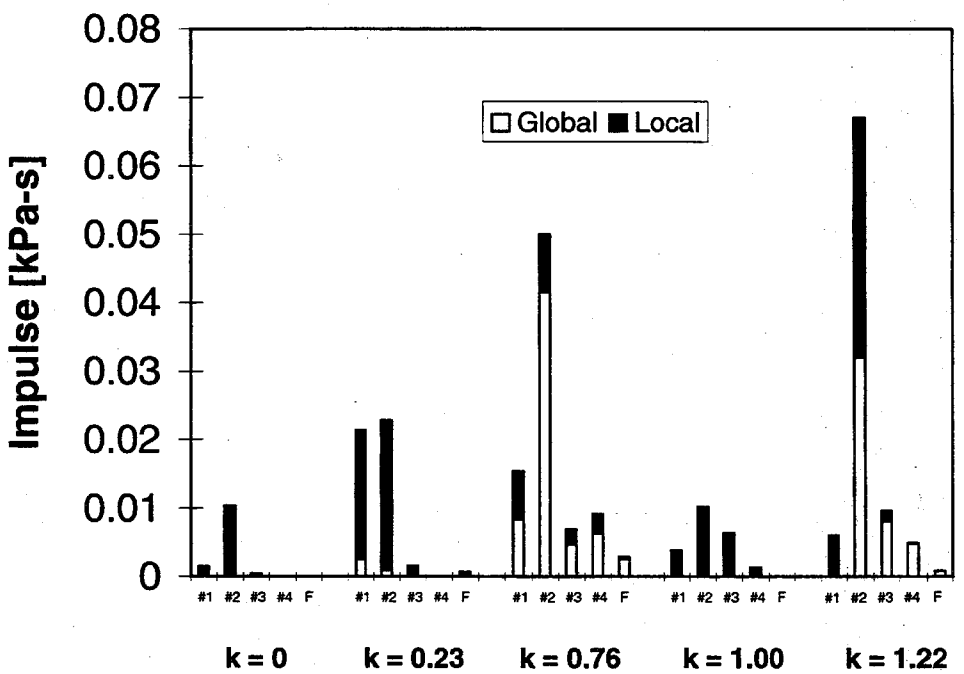

Figure 5.10: Impulse data for $k = 0.23$ along with the results of figure 5.9. Measurements are not available for transducer #4 at $k = 0.23$. Data for $\sigma = 0.95$, $U = 8m/s$ and $\overline{\alpha_f} = 5°$

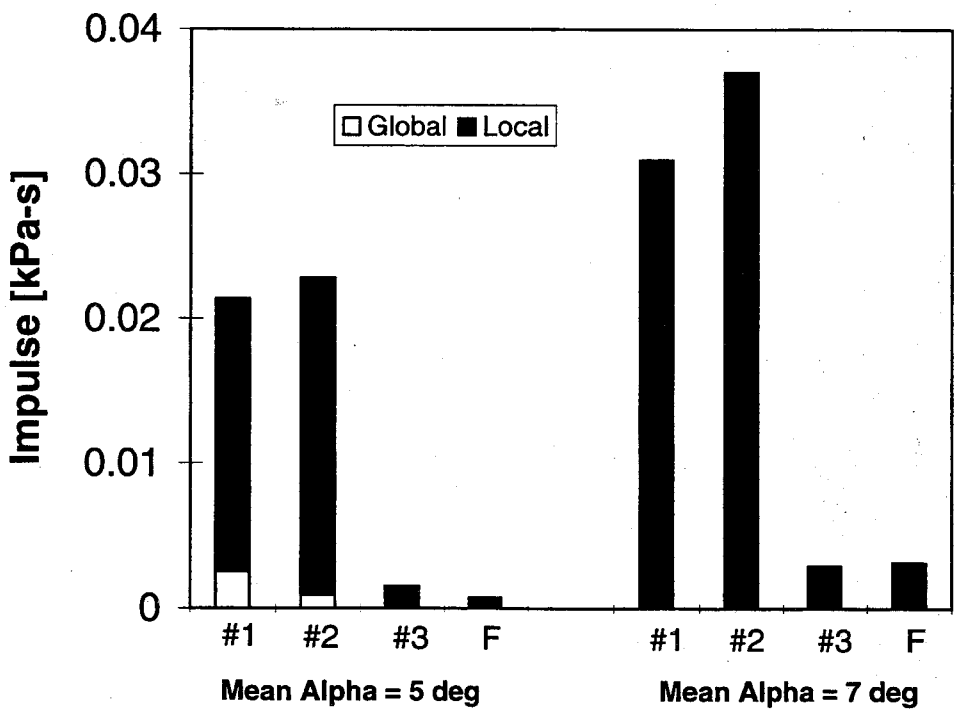

Figure 5.11: Impulse data for $k = 0.23$ at two different mean angles of attack, $\overline{\alpha_f}$. Measurements are not available for transducer #4. Data for $\sigma = 0.95$ and $U = 8m/s$.

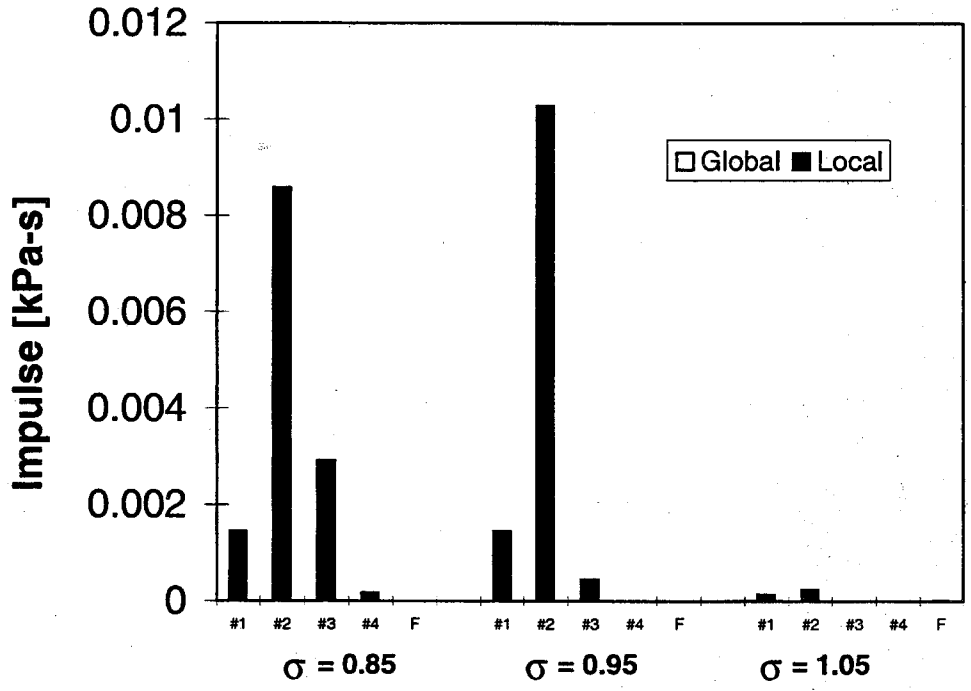

Figure 5.12: Effect of cavitation number, σ, on the impulse, I. Data for the static foil at an angle of attack of 5° and $U = 8m/s$.

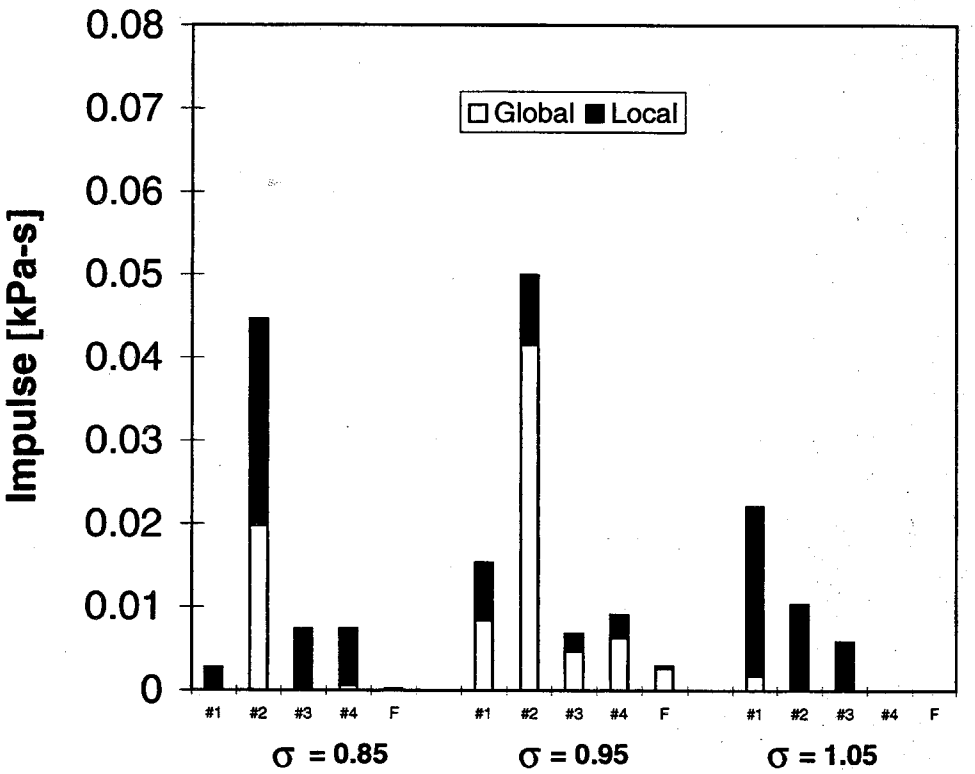

Figure 5.13: Effect of the cavitation number, σ, on the impulse, I. Data for the oscillating foil with $k = 0.76$, $U = 8m/s$ and $\overline{\alpha_f} = 5°$.

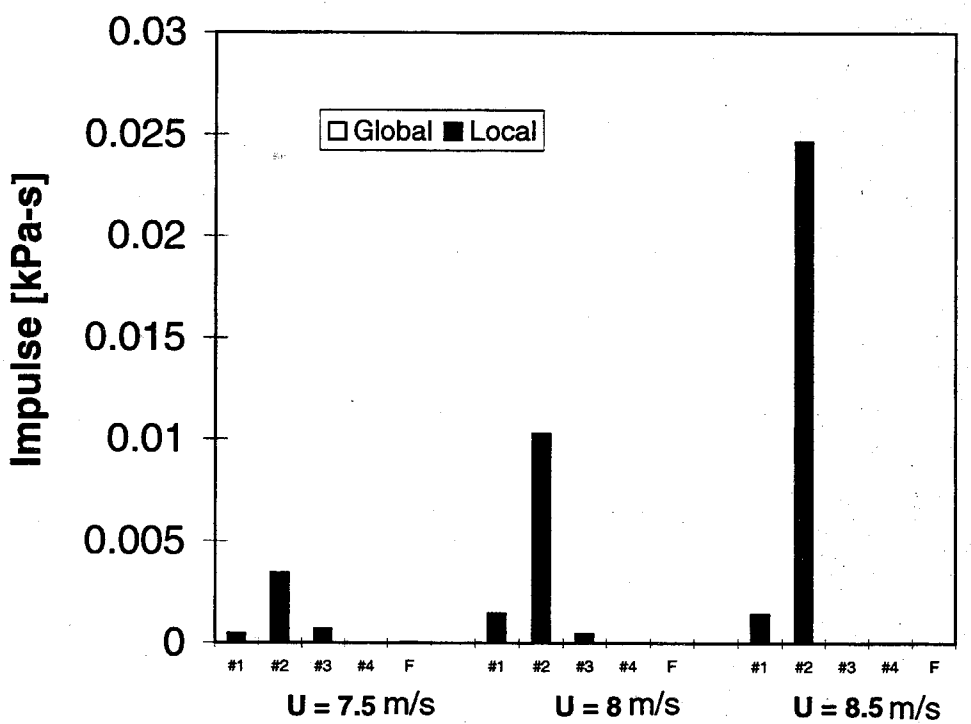

Figure 5.14: Effect of tunnel velocity, U, on the impulse, I. Data for a fixed angle of attack of 5° and $\sigma = 0.95$.

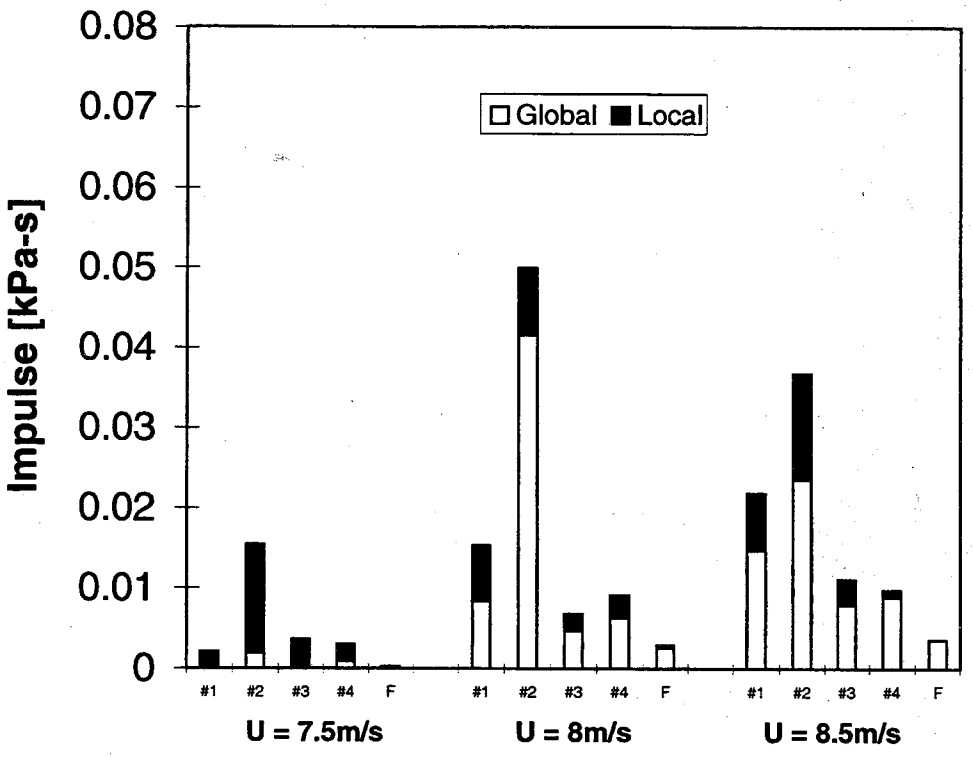

Figure 5.15: Effect of the tunnel velocity, U, on the impulse, I. Data for $\sigma = 0.95$, $0.72 < k < 0.81$ and $\overline{\alpha_f} = 5°$.

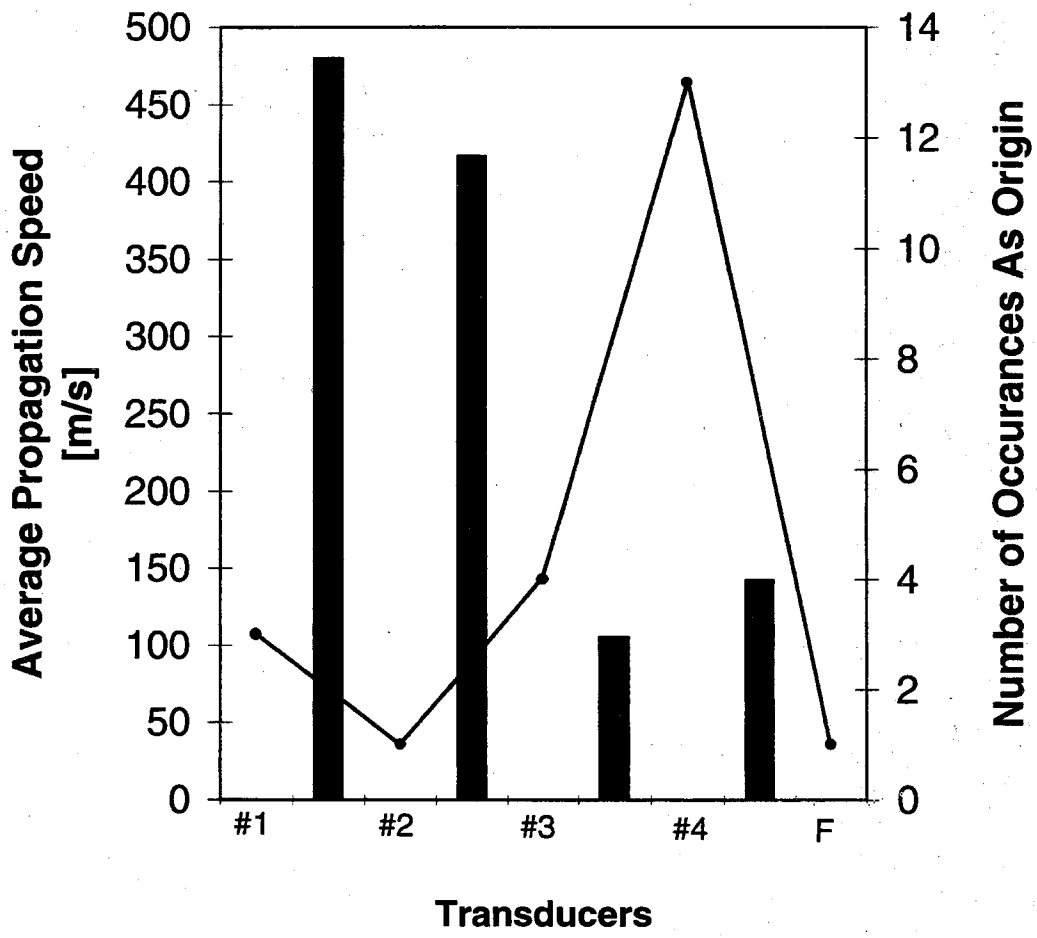

Figure 5.16: Speed of propagation and location of the origin of the global pressure pulses. Data for $\sigma = 0.95, k = 0.76, U = 8m/s$, and $\overline{\alpha_f} = 5°$.

Chapter 6 Bubbly Shock Waves

6.1 Bubbly Shock Waves in Local Event Structures

The large pressure pulse detected when a boundary of a local event structure passes over a transducer along with the geometrically coherent and nearly discrete change in void fraction across the boundary indicated that these structures consist of bubbly shock waves. This section consists of a more detailed examination of these structures and compares them to previous investigations of bubbly shock waves.

Both in the case of the crescent shaped regions and the leading edge structures, the boundary whose passage was correlated with the local pressure pulses was observed to propagate into the mixture. The downstream border of the crescent shaped region of photograph (a) of figure 5.2 and the entire upstream edge of the bubbly mixture depicted in photograph (d) of this figure are both bubbly shock waves. In the frame of reference of the shock wave, the bubbly mixture is moving upstream, or to the right in the photographs.

Noordzij and van Wijngaarden (1974) conducted an investigation of bubbly shock waves and undertook experiments to validate the analytical results. These experiments examined a shock propagating through a vertical tube containing a mixture of glycerine and air bubbles. Their experimental results were characterized by a greater than 80% change in void fraction across the shock, a value comparable to that which would apply to the photographs of figure 5.2.

Another similarity to the bubbly shock analysis and experiments of Noordzij and

van Wijngaarden (1974) is seen in photograph (d) of figure 5.2 which demonstrates the occurrence of multiple shocks, as indicated by the two arrows. After the initial shock passes, the bubbles rebound only to be collapsed again by a subsequent shock. The presence of multiple pulses as a leading edge structure passes over a transducer was common in the current experiments. Although only weak secondary shocks are present in the data from transducer #1 in figure 5.4 after the passage of a leading edge structure, the observation of bubble rebound after shock passage, such as that depicted in photograph (d) of figure 5.2, did indeed correlate with the presence of a series of strong secondary local pressure pulses. In the experiments of Noordzij and van Wijngaarden (1974), a similar series of oscillations in the void fraction was observed after the shock front passage.

The characteristic curvature of the shock waves present in the crescent shaped regions can be explained by the inhomogeneity of the bubbly mixture. As discussed at the end of chapter 4, large spanwise variations in void fraction are evident in the high speed movies after the passage of the re-entrant jet. This variation is due to a large spanwise variation in the thickness of the bubbly mixture. Since the void fraction of the undisturbed sheet cavity is near unity and since the total volume of vapor changes little during this rapid process, the sonic speed as a function of spanwise position will have a minimum near the 30% span location where the void fraction is the lowest. This reduction in the sonic speed near the 30% span location would cause a normal shock wave originating near the foil leading edge to curve concave toward the direction of propagation. The characteristic crescent shape is thus caused by the curving of the bubbly shock wave around the region of lower void fraction.

Such a variation in void fraction distribution was shown to result in the curvature of a normal bubbly shock by Kameda and Matsumoto (1995). Their experiments consisted of a bubbly shock tube containing a mixture of nitrogen gas and silicone oil. With an initial parabolic distribution of void fraction as a function of radial

coordinate, the front of the shock was observed to curve toward the high void fraction region due to the difference in propagation velocity.

6.2 Bubbly Shock Waves in Global Event Structures

An explanation for the extremely large pressure pulses radiated by cloud cavitation (see figure 3.8) is the formation of an inwardly propagating shock wave within the collapsing cloud as originally suggested by Mørch, Kedrinskii and Hanson (Mørch (1980, 1981, 1982) and Hanson *et al.* (1981)). Mørch and his co-workers speculated that collapse of the cloud involved the formation of a bubbly shock wave on the surface of the cloud and that inward propagation and geometric focusing of this shock would lead to very large localized pressure pulses.

This shock wave mechanism was recently demonstrated theoretically by Wang and Brennen (1994). The numerical calculations performed by Wang and Brennen (1994) employed a non-barotropic but homogeneous model which neglected for simplicity the relative motion between the bubbles and the liquid and did not allow for bubble break-up or coalescence. The model did, however, incorporate the interactive effects that the cavitating bubbles have on themselves and on the pressure and velocity of the liquid flow by coupling the conventional mass and momentum equations for the flow with the Rayleigh-Plesset equation for the bubble radius. The basic equations are same as those used by d'Agostino and Brennen (d'Agostino & Brennen (1983) and d'Agostino *et al.* (1988, 1989)) except that all the nonlinear terms are retained. These equations are reproduced here:

$$\frac{1}{r^2}\frac{\partial(r^2u)}{\partial r} = \frac{12\pi\eta R^2}{3+4\pi\eta R^3}\frac{DR}{Dt} \quad ; \quad r \leq A(t),$$

$$\frac{Du}{Dt} = -\frac{1}{6}(3 + 4\pi\eta R^3)\frac{\partial C_P}{\partial r} \quad ; \quad r \leq A(t),$$

where $u(r,t)$ is the mixture velocity, $R(r,t)$ is the individual bubble radius, $C_P(r,t) = (p(r,t) - p_0)/(\frac{1}{2}\rho_L U^2)$ is the pressure coefficient in the cloud, $p(r,t)$ is the mixture pressure and p_0 is the initial equilibrium pressure in the mixture, $A(t)$ is the radius of the cloud. The bubble population per unit liquid volume, η, is related to the void fraction, α, by $(\frac{4}{3}\pi R^3)\eta = \alpha/(1-\alpha)$. The variables and equations are non-dimensionalized using the initial bubble radius, R_0, a reference flow velocity, U, the time scale, R_0/U, and the dynamic pressure, $\frac{1}{2}\rho_L U^2$. To incorporate the bubble interactive effects, the dynamics of the bubbles are modeled using the Rayleigh-Plesset equation which connects the local mixture pressure coefficient, C_P, to the bubble radius, R:

$$R\frac{D^2R}{Dt^2} = -\frac{1}{2}C_P + \frac{2}{We}[R^{-3k} - R^{-1}] - \frac{3}{2}(\frac{DR}{Dt})^2 + \frac{\sigma}{2}[R^{-3k} - 1] - \frac{4}{Re}\frac{1}{R}\frac{DR}{Dt} \; ; \; r \leq A(t).$$

Using this model, a finite cloud of nuclei as depicted in figure 6.1 is subjected to a temporary decrease in the ambient pressure which causes the cloud to cavitate and then collapse. The cloud is assumed to be convected through a simple sinusoidal pressure depression whose depth is given by C_{pmin} and whose duration is defined by t_p (consequently the length, D, of the low pressure region is given by $D = Ut_p$). Results were obtained for various cavitation numbers, σ, and initial void fractions, α_0, in addition to A_0/R_0, D/R_0, C_{pmin}, etc.

A typical time history of the dimensionless bubble size at different positions within the cloud is shown in figure 6.2. The bubbles inside the cloud grow initially and then collapse rapidly. The collapse process begins at the outside edge of the cloud and accelerates toward the cloud center as a shock wave passes through the cloud. The bubbles then rebound only to be collapsed by another shock as the process is repeated.

A typical resulting time history of the radius of the cloud is shown in figure 6.3. Note that, unlike single bubbles, the cloud radius, $A(t)$, only decreases to a size marginally smaller than its equilibrium size during the collapse process. Wang and Brennen (1994) also examined the acoustic consequences of the shock wave. The normalized acoustic far-field noise, p_a, was calculated from the volumetric acceleration of the cloud using

$$p_a(t) = \frac{2R_0}{D}\left[A^2(t)\frac{d^2A(t)}{dt^2} + 2A(t)(\frac{dA(t)}{dt})^2\right],$$

where the normalizing length scale was chosen to be the length of the low pressure region, D. This normalized acoustic far-field noise is also depicted in figure 6.3. The series of collapses and rebounds of the cloud due to the inward propagation of a series of spherical shock waves cause the large peaks in the radiated acoustic noise present in this figure.

A similarity is noted between the numerical results depicted in figure 6.3 and the experimental results of figure 3.2. Direct comparisons between the experiments and the computations are difficult since Wang (1996) shows that the characteristic cloud dynamics and the resulting noise generation are strongly dependent on the parameter $\beta = \alpha_0(1-\alpha_0)A_0^2/R_0^2$ where α_0 is the initial void fraction, A_0 is the initial cloud radius and R_0 is the initial bubble radius. All of these parameters are very difficult to measure experimentally and only the initial cloud radius, A_0, was measured during the present work. Nonetheless, using the following parameters: $\sigma = 0.45$, $C_{PMIN} = -0.75$, $\alpha_o = 0.5\%$, $A_o = 100$, and $D/A_o = 2.5$, which correspond to figure 6.3, a maximum radiated acoustic pressure amplitude of $120kPa$ and a time interval between peaks of $0.7msec$ is calculated. These values are within one order of magnitude of those corresponding to figure 3.2: a maximum amplitude of $650kPa$ and an interval of $5msec$.

Several other qualitative similarities between the current experiments and the

work of Wang and Brennen (1995) are noted. One such agreement is the observation that the global collapse process does not involve large changes in the overall dimensions of the cloud; rather collapse involves large changes in the void fraction distribution within the cloud, as discussed in section 5.1. It was also noted that the global collapses observed during the experiments often generate multiple pulses in quick succession (e.g. figure 5.1, 5.4, 5.6 and 3.2). This observation is also similar to the results of Wang and Brennen (1995) as depicted in figure 6.3.

An additional quantitative comparison can be made by estimating the speed of propagation of the global shocks observed in the current experiments. The final stage of the global collapse occurs very rapidly as shown in frames (b) and (c) of figure 5.5. As seen in this figure, the global shock wave propagates from the outside of the cloud to the cloud center, a distance of approximately $6cm$, between the two frames which were taken during a time interval of $2msec$. Thus a crude estimate of the shock propagation speed is $30m/s$. The actual propagation takes place during a fraction of this interval, but this estimate provides a lower bound on the experimentally observed shock propagation speed. For the free stream velocity of the present experiments, $8.5m/s$, Wang (1996) calculates a shock propagation speed ranging from $8m/s$ near the exterior of the cloud to $800m/s$ near the center of the cloud. Also, the calculations of Kameda and Matsumoto (1995) result in a shock propagation speed of between $400m/s$ and $500m/s$. Although the lower bound estimate of $30m/s$ seems reasonable, this comparison is limited by the lack of information concerning the void fraction of the clouds observed in the experiments; the void fraction is shown by Wang (1996) to be an important parameter in the calculation of shock propagation speeds.

Finally, it should be noted that the clouds observed in the current experiments (e.g. figure 5.5) lack the spherical symmetry assumed in the model used by Wang and Brennen (1995). Nonetheless, it is also clear from figure 5.5 that the collapse of all or part of these non-spherical clouds produce points at which shock waves focus. The

various foci associated with curved gasdynamic shock waves is reviewed in the work of Sturtevant and Kulkarny (1976) and nonlinear gasdynamic effects are shown to limit the maximum amplitude at focus. However, it is not clear exactly what form the foci might take in the highly non-uniform, three dimensional bubbly environments such as that depicted in figure 5.5.

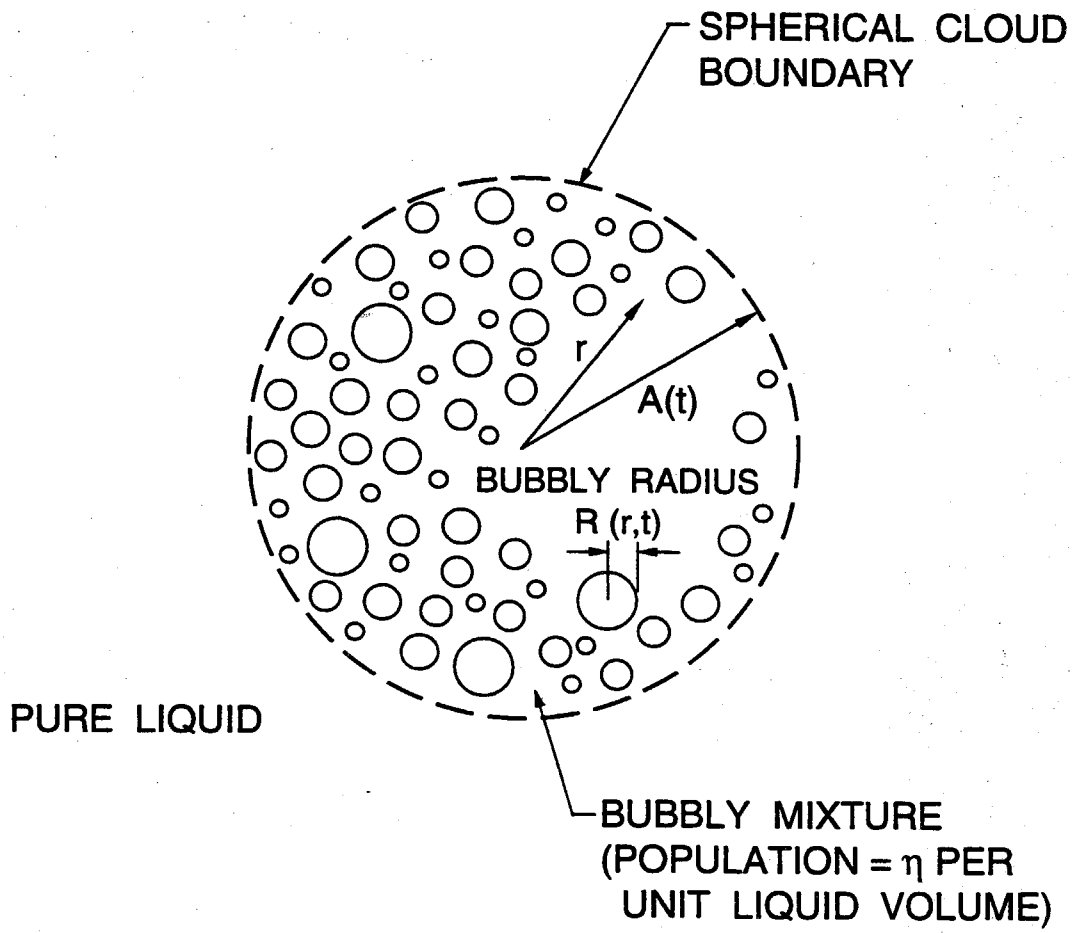

Figure 6.1: Schematic of a spherical cloud of bubbles used in numerical study by (Wang 1996).

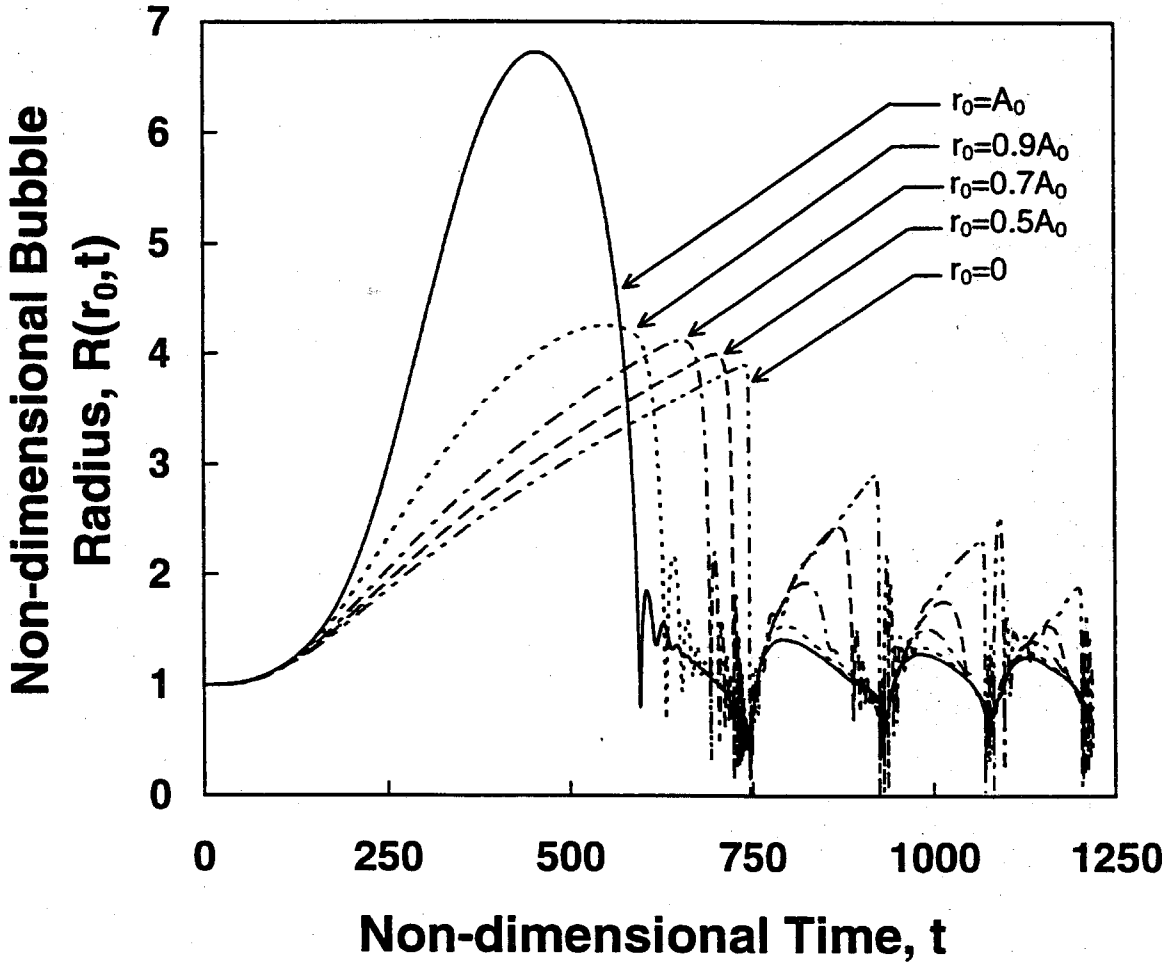

Figure 6.2: The time history of the dimensionless bubble size at five different positions in the cloud. Parameters used are $\sigma = 0.45$, $C_{pmin} = -0.75$, $\alpha_0 = 3\%$, $A_0 = 100$, and $D/A_0 = 5$. (Wang 1996)

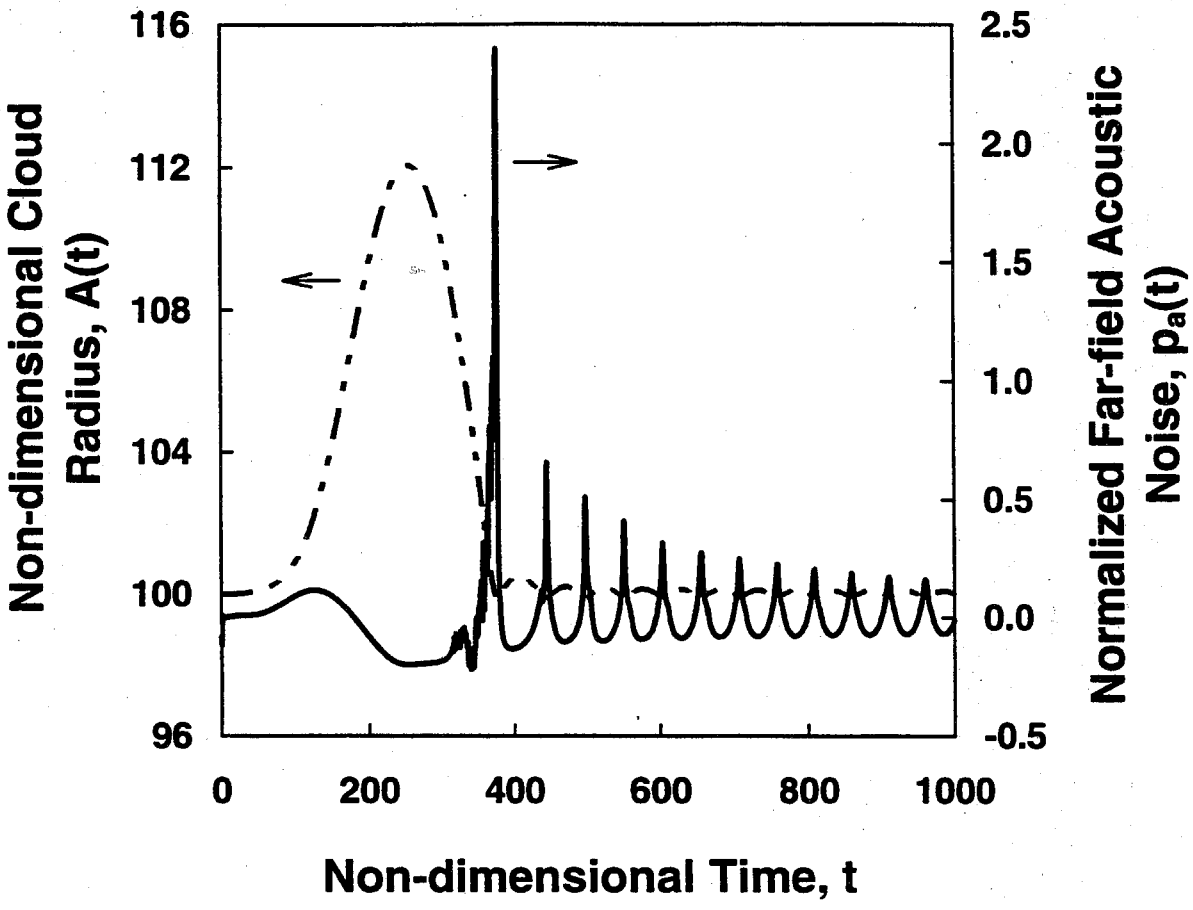

Figure 6.3: The time history of the dimensionless cloud radius and the far field cloud acoustic noise. Parameters used are $\sigma = 0.45$, $C_{PMIN} = -0.75$, $\alpha_o = 0.5\%$, $A_o = 100$, and $D/A_o = 2.5$. (Wang 1996)

Chapter 7 Summary and Discussion: Part 1

Large amplitude impulsive pressures were measured during experiments with both an oscillating and a static hydrofoil experiencing cloud cavitation, and these pressure pulses were correlated with the observation of several distinct cavitation structures. The pressure pulses were measured by piezoelectric transducers; four were recess mounted along the chord of the suction surface of a hydrofoil and two were flush mounted in the walls of the LTWT test section. These acoustic measurements were synchronized with high speed motion picture photography to determine the causal relationship between the cloud cavitation dynamics and the generation of the pressure pulses.

A preliminary parametric study detected large impulsive radiated acoustic pressures generated by cloud cavitation on the oscillating NACA 64A309 hydrofoil. The magnitudes of the pressure pulses measured by the transducer in the LTWT test section floor were on the order of several atmospheres. The acoustic impulses associated with these pulses were obtained by integration, and the variations with cavitation number, foil oscillation frequency and total air content were examined. The measured impulses peaked at the intermediate cavitation number studied and were relatively independent of the air content. The variations with foil oscillation frequency were significant and non-monotonic. Spectra of the noise, averaged over more than 40 cycles, were also examined and exhibited a typical f^{-1} variation with frequency. The shape of the spectra varied significantly with cavitation number, but changes in the air content and foil oscillation frequency produced no such discernible variation.

The impulses were consistent with, though considerably larger than, what would be expected from the extrapolation of data on single bubble cavitation. This suggests the existence of an additional mechanism in the cloud collapse that augments the noise, such as an inwardly propagating shock.

An examination of high speed motion pictures of cloud cavitation on an oscillating hydrofoil led to the identification of several distinct stages. Initial traveling bubbles near the leading edge coalesce into a single attached sheet cavity as the angle of attack increases. A re-entrant liquid jet then penetrates the sheet cavity from the downstream edge and breaks up the cavity into a bubbly mixture. The thickness of the bubbly mixture rapidly increases in the region of the jet by a mixing of the vapor/gas contained in the cavity with the surrounding liquid to create a much larger bubbly mixture. The dynamics of this process have been commented upon by several previous investigators including Knapp (1955), Wade and Acosta (1966), Lush and Skipp (1986), Kubota *et al.* (1992), de Lange *et al.* (1994) and Kawanami *et al.* (1996). The present observations underscore the importance of the jet as a mechanism for creating the bubbly mixture and determining the void fraction distribution inside the mixture. No large pressure pulses were observed prior to this stage in the oscillation cycle. Subsequently, shock waves are formed and propagate into the mixture resulting in the formation of crescent shaped regions and leading edge structures. The bubbly mixture detaches from the leading edge and is convected downstream to the stagnation region where the global collapse occurs.

The installation of recess mounted transducers in the NACA 0021 foil allowed for the measurement of unsteady pressures on the suction surface at four locations along the chord for a range of flow conditions. Large positive pressure impulses were detected on the surface of this hydrofoil during cloud cavitation, both while the foil oscillated and while it was held at a fixed angle of attack. The pulses were shown to have magnitudes on the order of tens of atmospheres with typical durations of the

order of tenths of milliseconds. Pressure pulses of similar magnitude were observed by Le *et al.* (1993), who measured pulse magnitudes of up to 7 MPa on a stationary foil at $\sigma = 0.81$, $U = 12m/s$ and an angle of attack of 4.8°. Their experiments used flush-mounted transducers with face diameters of $1mm$ and bandwidths over $300kHz$.

However, these pulse magnitudes are significantly greater than those measured by Shen and Peterson (1978) who detected pulses with magnitudes comparable to the dynamic pressure (up to $110kPa$). There are at least two explanations for this discrepancy. The primary reason is that the transducers used by Shen and Peterson (1978) had a bandwidth of only $2kHz$. The short duration impulses measured in the current experiments have a broadband frequency content with substantial contributions above $2kHz$. In addition, both the amplitude of foil oscillation (up to 1.55°) and the mean angle of attack (3.25°) used by Shen and Peterson (1978) were significantly less than those of the current experiments.

The radiated pulse magnitudes measured by Bark (1985) and Bark and van Berlekom (1978) were on the order of tens of kPa, but these were measured at locations off the foil surface. They are more comparable to the far field measurements made with the ceiling transducer in the current experiments but are significantly smaller than the impulse amplitudes measured by the transducer mounted in the LTWT floor. This difference in amplitude may be attributed to the significantly lower velocities of the Bark and van Berlekom experiments which were performed at $5m/s$.

Furthermore, an examination of the high speed movies led to the identification of two distinct types of pressure pulses. *Local* pulses, which are registered by a single transducer, are randomly distributed in time and space and are not repeated from cycle to cycle. Local pulses are caused at a given transducer location by the passage of either crescent shaped regions of low void fraction or leading edge structures. In either case, they are observed during a rapid transition from a region of high void

fraction to a region of low void fraction. The crescent-shaped regions are similar to the "depressions in the cavity surface" noted by Shen and Peterson (1978) and the "deep inward buckling of the cavity interface" observed by Bark (1985).

On the other hand, *global* pulses, which occur almost simultaneously on all four transducers, are of higher amplitude, radiate substantial far field noise and are repeated at the same point of each oscillation cycle. Global pulses are caused by large scale cloud cavitation collapse and were not observed on the static foil with steady mean flow conditions.

By calculating the acoustic impulse, a quantitative measure of the effect of reduced frequency, k, cavitation number, σ, and tunnel velocity on the strength of both the local and global pressure pulses was obtained. The reduced frequency is an important parameter in the determination of the total impulse level and the local and global pulse distribution. The cavitation number has a significant effect on the global impulse strength, but large impulses are still present on the foil surface at values of σ where acoustic radiation is minimal and global pulses are rare or non-existent. The changes with tunnel velocity were significantly different for the stationary and oscillating foils. The local impulses on the stationary foil increased greatly with tunnel velocity and the global impulses on the oscillating foil did likewise. However, the local impulses on the oscillating foil did not change so dramatically with tunnel velocity. Also, the spatial distribution of the impulse measurements, while highly influenced by the cavitation number, is virtually independent of the reduced frequency and tunnel velocity.

It seems clear that both the local and global surface pressure pulses could contribute to foil damage. Indeed, the very large magnitudes of these surface impacts could be responsible for the foil damage reported by Morgan (1995), who observed propeller blade trailing edges bent away from the suction surface and toward the pressure surface.

The large pressure pulse associated with the local and global cavitation structures,

the geometric coherence of their boundaries and the nearly discrete change in void fraction across the boundaries of these structures indicate that these structures consist of bubbly shock waves. The change in the void fraction across the observed shock fronts and the rebounding of bubbles behind the initial shock and their subsequent collapse by secondary shocks bear strong similarities to the work of Noordzij and van Wijngaarden (1974) on shock waves in air bubble/glycerine mixtures. Also, the curvature of the shock fronts in the crescent shaped regions toward regions of higher void fraction due to differences in the propagation velocity is an observed behavior which is in good agreement with the observations of Kameda and Matsumoto (1995) who examined shock waves propagating through a bubbly mixture of nitrogen gas and silicone oil. Indeed, the relationship between the curvature of the front and the local void fraction as the front propagates through the highly inhomogeneous bubbly mixture is further evidence that these fronts are bubbly shock waves.

The global collapse process entails not a volumetric collapse of the cloud itself, but rather a rapid change in the void fraction distribution inside the cloud. The radius of the cloud changes only slightly during this process as the void fraction decreases dramatically at locations throughout the cloud. This process is similar to the numerical work of Wang and Brennen (1994) who showed how a shock wave develops as part of the non-linear collapse of a spherical cloud of cavitation bubbles. The focusing of the shock produced very high pressures at the center of the cloud and then caused a rebound of the cloud. The volumetric acceleration induced a large pulse in the far-field noise. Direct comparisons between the numerical and experimental work are difficult due to the importance of the parameter β (which involves the void fraction, α) and the difficulty associated with estimating α experimentally. Rough quantitative comparisons were in good agreement, however. The presence of multiple radiated pulses in quick succession was another shared characteristic of the current experiments and the numerical work of Wang and Brennen (1994).

Of course, the experimental clouds are far from spherical, but the collapse of all or parts of non-spherical clouds will produce points at which shock waves focus to produce large radiated pulses. It is not currently clear what three-dimensional forms the propagating shocks might take in the highly non-uniform bubbly environments which occur in real flows. Even in a homogeneous fluid, the focusing of shock waves can become quite complex (Sturtevant and Kulkarny (1976)). However, the present experiments suggest that shock focusing is the primary mechanism for the enhanced noise and damage potential associated with cloud cavitation.

Although surface measurements of unsteady pressure were not attempted with the NACA 64A309 foil, observations of the cloud cavitation structures on this foil are indicative of the generality of these findings. In the high speed motion pictures taken of cloud cavitation on this foil, both types of local event structures are clearly evident. Crescent shaped regions and leading edge structures are present and their kinematics and dynamics do not differ significantly from those seen on the NACA 0021 foil. Global events are also present and the cloud collapse behaves as described in section 5.1 and section 6.2. This similarity in the local and global cloud cavitation structures is observed despite the significantly different cross-sections and surface pressure distributions of the two foils (see figure 2.4 and figure 2.5). The only significant difference in the stages of cloud cavitation observed on the two foils is the presence of traveling bubble cavitation on the NACA 0021 foil for a longer portion of the foil oscillation cycle. The traveling bubble cavitation rapidly changes to attached sheet cavitation on the NACA 64A309 foil due to its large leading edge suction relative to the more uniform pressure distribution on the thicker NACA 0021 foil.

The structures described in this thesis are expected to be important features in a wide range of cavitating flows since they were observed on two significantly different hydrofoils and since similar structures were noted in the work of Shen and Peterson (1978) on a Joukowski section and by Bark (1985) on a NACA 16 hydrofoil. However,

scaling effects remain to be examined. How these bubbly shock structures behave in high Reynolds number flows is not currently known, but predictions can be made by anticipating a large increase in the parameter β due to a large increase in the ratio of the cloud radius to the typical bubble radius.

Part II

Control of Cloud Cavitation Noise by Air Injection

Chapter 1 Introduction

The presence of a non-condensible gas inside a single cavitation bubble reduces the rate of collapse and increases the minimum bubble volume (Brennen (1995)). Thus one mitigation strategy is the deliberate injection of air to help "cushion" the collapse, thereby reducing the noise and damage potential. Several previous investigations have explored this method by ejecting air from ventilation holes in the suction surface of a hydrofoil. Ukon (1986) used air injection from the leading edge of a stationary foil and found a consistent reduction in the cavitation noise in the frequency range 0.6 to $100kHz$. The maximum noise reduction achieved was of the order of $20dB$. There is some suggestion in his data that air flow rates above a certain optimal level no longer decrease the noise. Arndt *et al.* (1993) performed similar air injection tests with a stationary foil and found some reduction in the mean square hydrophone signal in the 10 to $30Hz$ band. The reduction was a factor of approximately 3 to 5 for small air flow rates, but there was little additional effect at higher flow rates.

It should also be noted that the United States Navy has employed air injection systems to reduce the cavitation noise produced by the propellers of surface combatant ships. These devices are referred to as Prairie/Masker systems, but detailed principles of operation of these devices have not been released to the public. It is known, however, that these devices continuously inject air into the propeller region.

Minimizing the volume of air injected by such a system is desirable for several reasons. Minimizing the air flow rate would improve the efficiency of the system, reduce any adverse effects on the propeller performance and reduce the number of bubbles present in the wake of the ship. The reduction of bubbles in the ship wake is desirable for military applications since it makes the ship more difficult to detect.

One strategy for the minimization of the air flow rate is to inject a pulse of air, rather than a continuous stream. It was uncertain, however, whether the same level of noise reduction could be attained with pulsed air injection as with continuous injection.

The objective of the present experiments was to examine and quantify the effectiveness of air injection in the reduction of cloud cavitation noise, to identify the physical process responsible for any such noise reduction and to investigate the effectiveness of pulsed air injection.

Chapter 2 Experimental Facilities

2.1 Location of Ventilation Holes

Both the NACA 0021 and the NACA 64A309 hydrofoil were equipped with ventilation holes to allow air to be injected into the suction side of the foil. The NACA 64A309 foil had a $\frac{5}{16}in$ diameter central shaft drilled along the span at the axis of rotation (38% chord from the leading edge). Four ventilation holes were drilled in the suction surface of the foil perpendicularly intersecting this central shaft. These holes were $\frac{1}{16}in$ in diameter and were located at 15%, 36%, 58% and 80% along the span as measured from the foil root. The number and size of these holes proved to be excessive since the asymptotic noise reduction limit flow rate was much lower than anticipated (see chapter 3).

The NACA 0021 foil had only a single air injection hole. It was also located at the axis of rotation (38% chord from the leading edge). This $\frac{1}{8}in$ diameter hole was placed at 34% span from the foil root to locate the air injection point near the point of cloud detachment and the thickest part of the sheet cavitation. After leaving the injection valve, (see section 2.3) the air passed through a $\frac{1}{8}in$ diameter thin wall steel tube which was connected to the upper half of the NACA 0021 foil using a Swagelok fitting. The size of the hole and steel tube was selected to ensure that the choked flow rate would be significantly greater than the asymptotic noise reduction limit flow rate determined in the previous experiments (see chapter 3). Subject to this restriction, the volume of air between the valve and the injection point was minimized to increase the dynamic response of the air injection system.

2.2 Orifice Air Flow Meter

For the continuous air injection experiments, the air flow rate was measured using an orifice flow meter. This flow meter had a water manometer for measuring the pressure drop across the orifice, Δp, and an analog pressure gage for measuring the static pressure upstream of the orifice, p_1. The normalized air flow rate, $q = Q/Ucs$, was given by the following equation (Avallone and Baumeister(1978)):

$$q = \frac{\kappa Y A \sqrt{\frac{2\Delta p p_1}{RT_1}}}{\frac{p}{RT} Ucs},$$

where A is the area of the orifice, R is the ideal gas constant, T_1 is the temperature just upstream of the orifice and p and T are measured in the tunnel test section. Y is the compressibility factor, which was taken to be unity in all the present cases. Finally, κ is an empirical constant which was determined by measuring the volume of air exiting the flow meter in a given period of time for several values of Δp. The data from this calibration are presented in figure 2.1, and κ was determined to be 1.229 (Zenit (1994)).

The uncertainty associated with the measurement of p_1 during the experiments was estimated to be $\pm 1 inHg$. This led to a $\pm 12\%$ uncertainty in the measurement of q.

2.3 Pulsed Air Injection System

To perform experiments involving the injection of air during only a fraction of the foil oscillation period, a pulsed air injection system was designed. This system consisted of a solenoid valve and valve control hardware and software. The solenoid was originally designed to be used as a fuel injector for a natural gas vehicle and had a bandwidth of approximately $230Hz$. This valve was connected to the $\frac{1}{8}in$ thin wall steel tube as described in Part 2, section 2.1.

The valve was actuated by an electronic control unit. The synchronization pulse from the foil motor control unit and the output from the foil motor shaft encoder were connected to the valve control unit. This circuit would then open and close the valve once each foil oscillation cycle. The offset of the point in the foil oscillation cycle at which the valve opens relative to the point of maximum angle of attack could be adjusted by using a thumbwheel on the valve control unit. The offset could range from 0 to 100% of the foil oscillation period. The duration of the valve opening could also be adjusted by using a second thumbwheel which determined the point in the foil oscillation cycle that the valve would be closed.

Alternatively, the offset and duration could be supplied by a computer to allow for active feedback control of the pulsed air injection. Using two of the digital output channels of the RC card (see section 2.4) of chapter 2, 32 bits of data could be sent to the valve control unit each oscillation cycle to specify the percentage of the foil oscillation period at which the valve would open and close. Software was written to control the RC card and it was demonstrated that a full $64K$ buffer of data could be acquired in approximately $0.082sec$ immediately followed by the 32 bit data transmission which required only an additional $0.2msec$. Therefore, the foil synchronization pulse provides an adequate trigger provided that the foil oscillates at $12Hz$ or more. Aside from this demonstration, computer control of the valve was not further considered in the present work.

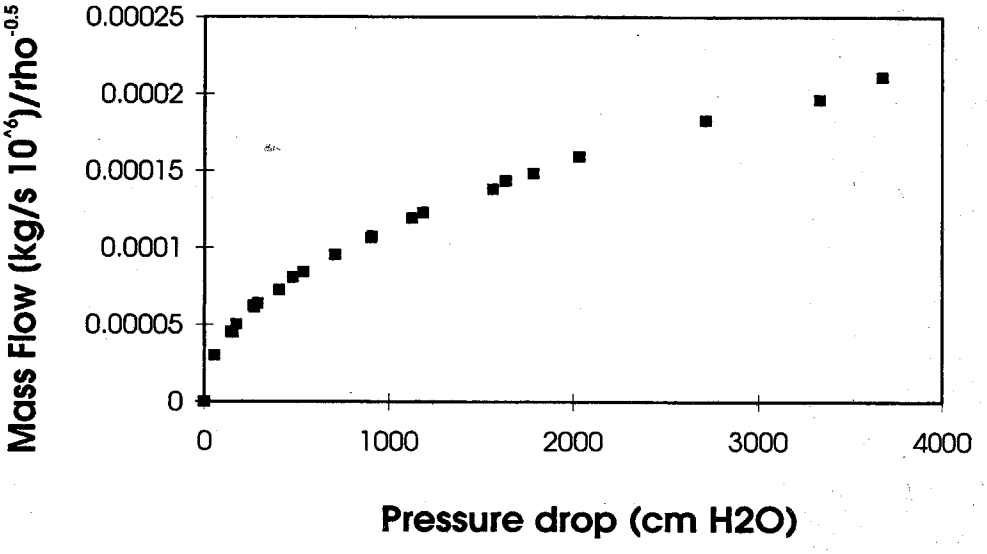

Figure 2.1: Orifice flowmeter calibration data. Mass flow rate plotted as a function of pressure drop across the orifice. Calibration performed by Roberto Zenit (1994) at atmospheric conditions.

Chapter 3 Experiments with NACA 64A309 Foil

During the parametric study described in part 1, chapter 3, measurements of the acoustic impulse were made while injecting air out of the NACA 64A309 foil at several different flow rates. This air injection resulted in a dramatic reduction in the sound level. At a sufficiently high air flow rate, the periodic bursts of noise associated with cloud cavitation collapse could no longer be detected either by ear or by transducer. Figure 3.1 illustrates this noise reduction as a function of normalized air injection flow rate, q, which is defined as the volumetric flow rate of air at the LTWT test section pressure and temperature, Q, divided by the tunnel velocity and the planform area of the foil, i.e. $q = \frac{Q}{Ucs}$. Data from the current experiments are plotted along with results from work by Arndt, *et al.* (1993) and Ukon (1986).

The ordinate of this figure is the ratio of the radiated acoustic pressure level at a given air flow rate to the radiated acoustic pressure level without air injection. To calculate this ratio, the average impulse data from the NACA 64A309 foil experiments and the root mean squared acoustic pressure for the data from Arndt *et al.* and Ukon were used. It should be noted that the experimental data showed a very strong correlation between the impulse and the RMS acoustic pressure.

The experiments performed by Arndt *et al.* and Ukon utilized stationary hydrofoils. Although cavitation clouds can separate periodically from sheet cavitation on a stationary foil, the collapse usually lacks the intensity of cloud cavitation caused by an imposed periodicity. The resulting low ratio of cavitation noise to background noise could explain the relatively small noise reduction due to air flow which is apparent in

the data of Arndt *et al.*.

In contrast, the results of the NACA 64A309 foil experiments indicate that the impulse could be reduced by a factor greater than 200 at an air flow rate, q, of approximately 0.001. At this flow rate, the periodic cloud cavitation noise was completely suppressed, and a further increase in the air flow rate had no discernible effect. An asymptotic limit to the amount of noise reduction is also evident in the data from Arndt, *et al.* (1993) and Ukon (1986).

Several qualitative differences were noted in the cloud cavitation structure with and without air injection. One effect of air injection was an increase in the average size of the sheet cavity. This phenomenon was previously noted by Ukon (1986). Although the two photographs in figure 3.2 were taken at identical cavitation numbers, reduced frequencies, and angles of attack, the cavity area extends much further along the chord in the air injection case. This effect is simply due to an increase in the mean pressure in the cavity and therefore a decrease in the effective cavitation number. Examination of the still photographs also shows that the vapor-liquid interface is disturbed by the injected air prior to the passage of the reentrant jet. The single attached cavity is thus fragmented into a bubbly mixture sooner and more severely when air is injected. Further discussion regarding the effect of air injection on the global and local event structures can be found in part 2, section 4.3.

The spectral content of the cavitation noise also changed with air injection. Figure 3.3 shows the average normalized Fourier spectra for three different air flow rates. The broadband f^{-n} behavior, with a value of n near unity, remains similar to that observed in the spectra from experiments without air injection (see part 1, section 3.2). However, as the air injection flow rate is increased, the Fourier magnitudes in the frequency range between 100 Hz and 8 kHz decrease relative to the high and low frequency content.

The prominent spike at $4kHz$ which was present in all of the other spectra is

absent in figure 3.3. In part 1, section 3.2, this spike was shown to be caused by a resonance of the LTWT test section. During the air injection experiments, an accumulation of air near the ceiling of the test section was observed. The presence of a free surface would drastically change the resonant properties of the tunnel. Furthermore, at the experimental conditions of $\sigma = 0.95, U = 8m/s$, a bubble with a radius of approximately $0.3mm$ would have a resonant frequency of $4kHz$ (Brennen (1995)). Many bubbles with radii of order $1mm$ were observed in the free stream in the LTWT during the air injection experiments and these bubbles will absorb acoustic energy in the frequency band near tunnel resonance. Therefore, the injection of air suppresses the tunnel resonance and thus no spikes are found in the spectra in the $4kHz$ range.

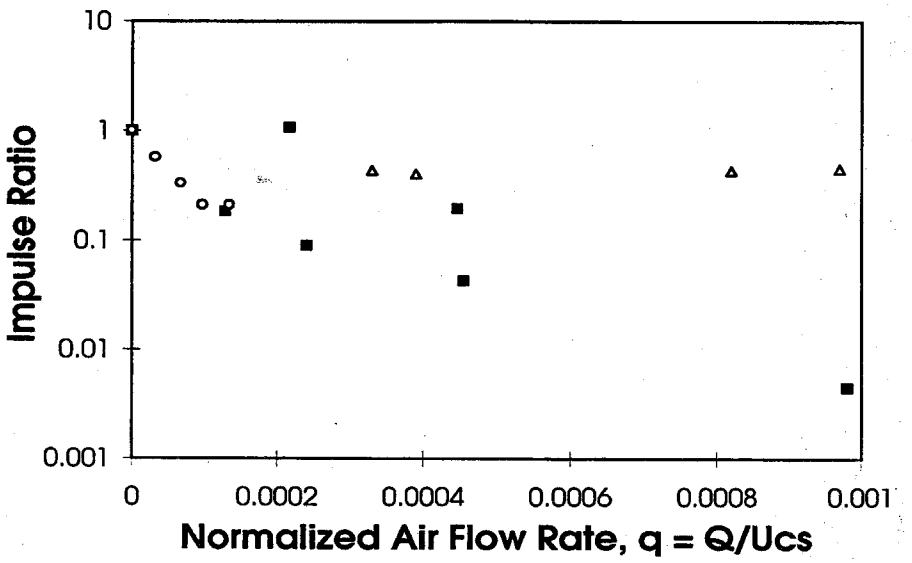

Figure 3.1: Effect of continuous air flow rate on the radiated noise, normalized by the noise without air injection. Data for the NACA 64A309 foil experiments at $\sigma = 1.2$, $k = 0.8$, $TAC = 5 - 10ppm$ are shown (■), and compared with data from Ukon (1986) at $\sigma = 0.74$, $\alpha = 6.4°$, $U = 8m/s$ (○) and Arndt *et al.* (1993) at $\sigma = 0.9$, $\alpha = 8°$, $U = 15$ and $7.5m/s$ (△).

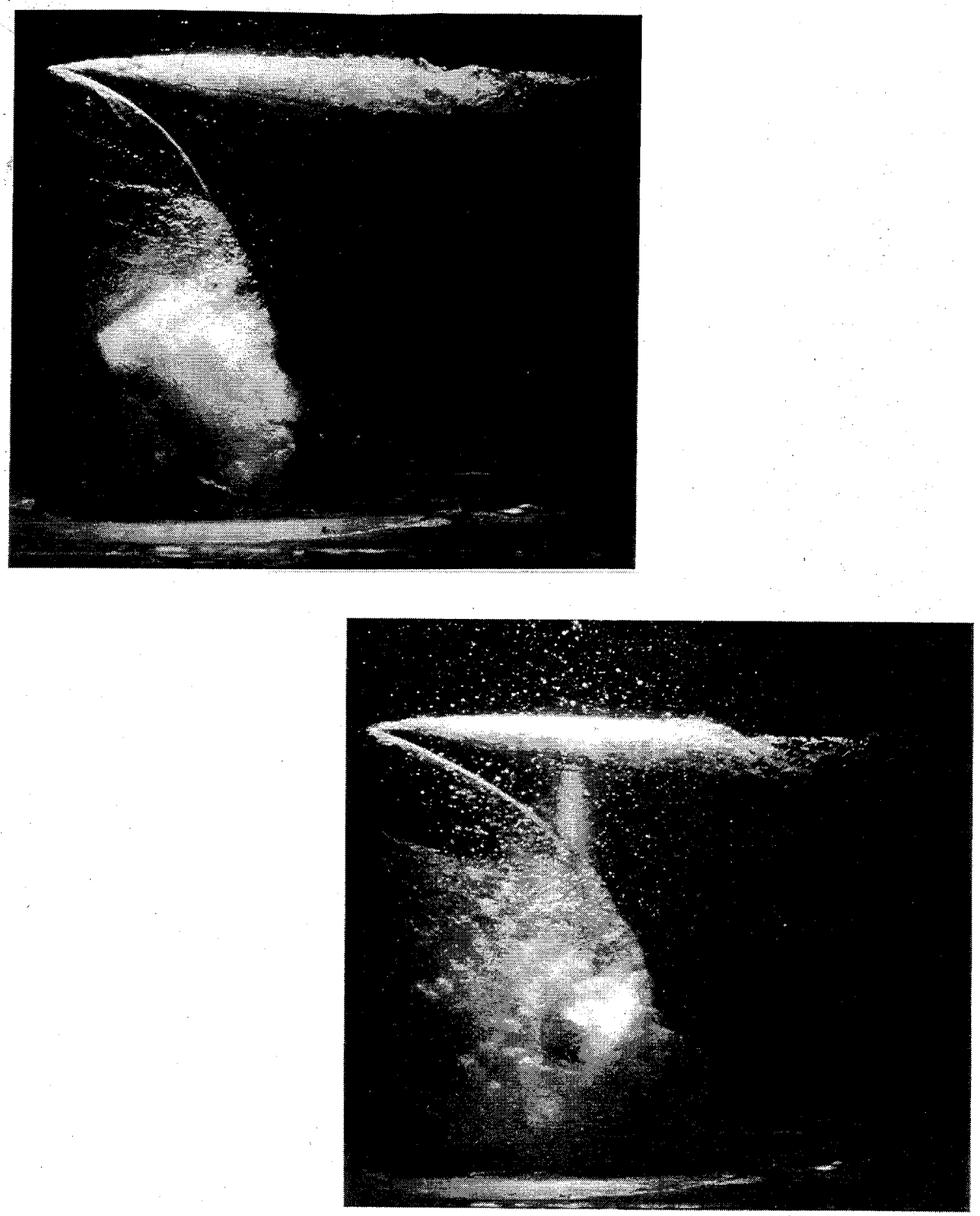

Figure 3.2: Qualitative effect of air injection on cloud cavitation structure. The photograph on the left is without air injection, the photograph on the right has a normalized air flow rate of $q = 4.5(10)^{-4}$. Both photographs were taken at $\sigma = 1.2$, $k = 0.8$, and $\alpha = 12.3°$ (α decreasing). Flow is from left to right.

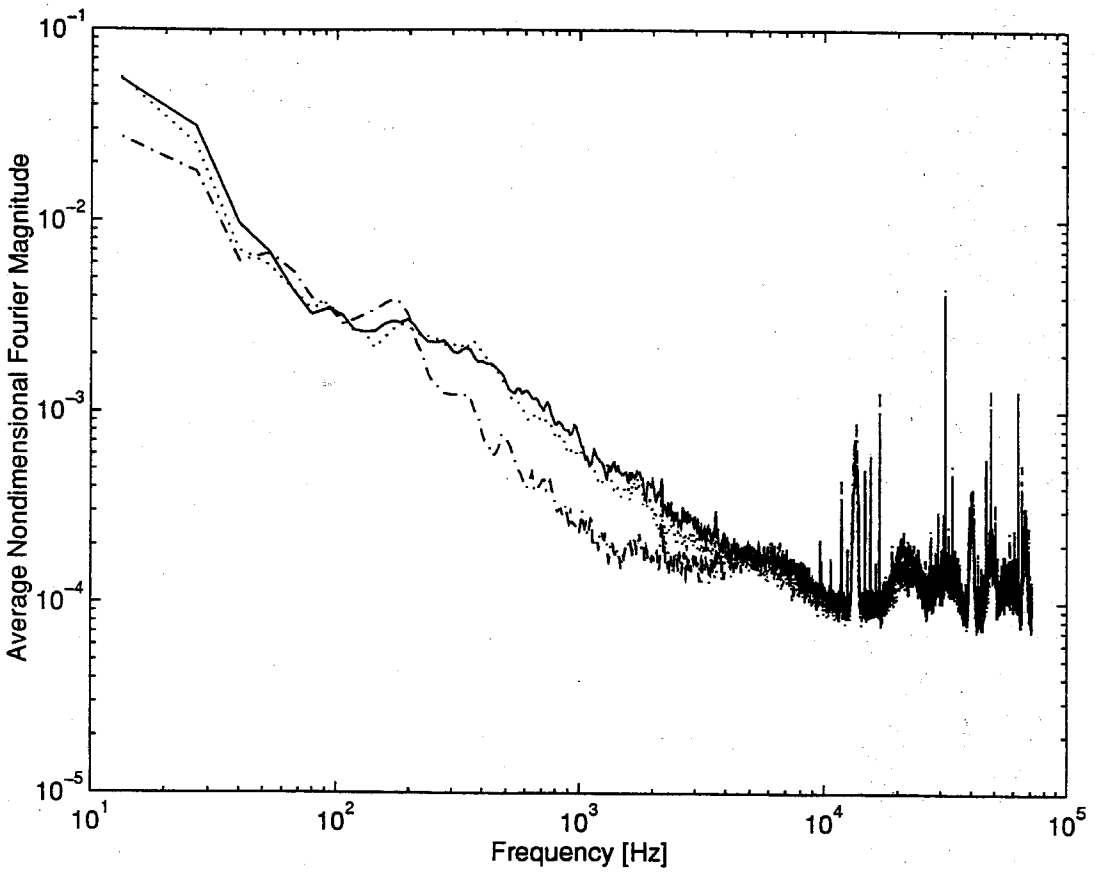

Figure 3.3: Effect of air injection on the spectral content of the noise for three normalized air flow rates: $q = 1.3 \times 10^{-4}$ (solid line), $q = 2.4 \times 10^{-4}$ (dotted line), $q = 9.8 \times 10^{-4}$ (dot-dash line). Data for $k = 0.8$, $TAC = 7 - 10ppm$.

Chapter 4 Experiments with NACA 0021 Foil

4.1 Floor Transducer Measurements - Continuous Air Injection

The continuous air injection experiments performed with the NACA 64A309 foil were repeated using the NACA 0021 foil and a similarly dramatic reduction in the cloud cavitation noise was observed. Figure 4.1 reproduces figure 3.1 and adds the data taken with the NACA 0021 foil. Each of the new data points corresponds to an average of the impulses of 40 oscillation cycles with the same flow conditions. The data for the NACA 0021 foil differs from the results for the NACA 64A309 foil in several respects.

Curiously, at the lowest air injection flow rate the average acoustic impulse increases relative to the case without air injection. This initial increase in radiated acoustic pressure was verified by repeating the experiments at this flow rate, $q = 1.6(10)^{-4}$, four times for a total of 160 oscillation cycles. All four points are plotted in figure 4.1. The increase in impulse was quite repeatable; the average impulse varied from $2.0(10)^{-3}$ to $2.6(10)^{-3}$ over these four runs and this variation is representative of the scatter observed at the other flow rates. The zero flow rate experiment was also repeated without any substantial change in the average impulse. The initial increase in the noise was also easily detected audibly in the laboratory.

After this initial increase in the cloud cavitation noise, the average impulse falls off rapidly as the air injection flow rate increases further. The noise reduction limit

is reached earlier than in the previous case. The reduction is also more complete; no pressure pulse exceeded the algorithm threshold at flow rates greater than $q = 5(10)^{-4}$.

These measurements made off the surface of the foil could be influenced by the presence of a large number of air bubbles in the acoustic transmission path between the cavitating foil and the floor transducer. The floor transducer was located near the cloud collapse region just downstream of the foil and this proximity diminishes the likelihood of any acoustic attenuation due to the air bubbles. Nonetheless, an effort was undertaken to examine the acoustic attenuation over larger distances in the LTWT test section and this effort is detailed in Appendix A. The lack of an attenuating effect on the floor transducer measurements was confirmed by noting that the average impulses measured at $q = 1.6(10)^{-4}$ and $q = 0$ were quite repeatable despite the fact that the TAC varied from 6.6 to 9.1 ppm during these experiments. Furthermore, the magnitudes of the 40 acoustic impulses obtained during a single continuous air injection experiment showed no correlation with running time. Therefore, acoustic attenuation due to the injection of air bubbles does not have a corrupting effect on the floor transducer measurements.

4.2 Surface Pressure Measurements - Continuous Air Injection

The recess mounted transducers installed in the NACA 0021 foil provided a clear indication of the effect of air injection on the acoustic impulses measured on the foil surface. Figure 4.2 depicts the impulses measured at the four different locations on the foil surface as a function of normalized air flow rate, q. Only the impulses measured near the trailing edge show the initial increase for a low air flow rate that was characteristic of the new floor transducer measurements depicted in figure 4.1.

The surface impulses show a high air flow rate asymptotic limit in the noise reduction similar to the behavior of the far field measurements. The reduction of the surface impulses is as high as two orders of magnitude at flow rates above $q = 7(10)^{-4}$.

4.3 High Speed Motion Picture Observations

By examining the high speed motion pictures taken of both the NACA 64A309 and NACA 0021 hydrofoils during the continuous air injection experiments, an explanation for the reduction in cloud cavitation radiated noise can be discerned. The injection of air at flow rates above the asymptotic noise reduction limit precludes the rapid and coherent global collapse of the cavitation cloud. The remains of the sheet cavitation, after detaching from the foil surface, persist as they are convected downstream. There is no rapid change in void fraction; rather, the cloud collapses gradually over a period of approximately $16msec$, an order of magnitude increase relative to the global collapse times observed with no air injection. Furthermore, there is no directional coherence to the collapse process. The void fraction decreases almost randomly throughout the cavitation cloud rather than progressing from the outside of the cloud toward the center as observed in the experiments without air injection and as illustrated by the numerical study by Wang (1996).

The injection of air does not, however, preclude the occurrence of local events. Both crescent shaped regions of low void fraction and leading edge structures are observed in the high speed movies of air injection on both foils. Although these local structures are frequently observed in the movies, they seldom result in the production of impulsive pressures on the foil surface. In the few cases where impulsive pressures were generated by local events, the magnitudes of the pulses were significantly lower than those measured without air injection; during air injection, the magnitudes of the local pulses did not exceed $500kPa$. As previously noted in the experiments without

air injection, (see part 1, section 5.1), in each case when local pressure pulses were detected by the foil surface transducers, they could be correlated with the presence of a local structure.

Figure 4.3 depicts selected frames from a high speed motion picture of air injection on the NACA 0021 hydrofoil with $k = 0.76$, $\sigma = 0.95$, $U = 8m/s$, $\overline{\alpha_f} = 5°$. The air flow rate was not measured during this experiment, but the flow rate was significantly greater than the asymptotic noise reduction limit depicted in figure 4.1. The acoustic data taken during the filming of this high speed movie is presented in figure 4.4, and there are no impulsive pressures, either local or global, detected on the foil surface. The radiated acoustic pressure measured by the floor and ceiling transducers also contains no impulses.

Frames (a) through (c) of figure 4.3 depict the re-entrant jet and the leading edge of the jet is marked by a dashed line in these photos. In frame (a) of figure 4.3, the re-entrant jet has begun to penetrate the attached cavity which has already been broken up to some extent by the air injection. In this photo, the jet has just reached the air injection point. The jet only makes slow progress toward the leading edge of the foil after passing the air injection point; the time interval between frames (b) and (c) is $8msec.$

Several leading edge and crescent shaped regions are clearly evident in the high speed movie frames. A leading edge structure is evident in frames (f), (g) and (h), as indicated by the arrows in figure 4.3. Crescent shaped regions of low void fraction are also seen in frames (c), (e), (f), (g), (h) and (i) of this figure. Despite the presence of structures as distinct as the crescent shaped region in frame (h), no local pulses are detected in the acoustic data of figure 4.4.

Frame (i) of figure 4.3 illustrates the fragmentation of the detached bubbly mixture when air is injected. Unlike the coherent bubble cloud depicted in frame (m) of part 1, figure 4.2, the remains of the sheet cavity become a highly non-uniform bubbly

mixture when air is injected. These fragmented bubble clouds persist as they are convected downstream into the high pressure stagnation region. There is no rapid or coherent global collapse like the one between frames (n) and (o) of part 1, figure 4.2 which were taken only $2msec$ apart. In contrast, frames (i) through (n) of figure 4.3 span an interval of $20msec$. In fact, the sheet cavity remains persist even as the next cycle begins, as depicted in frames (o) through (r).

The high speed movies indicate that the presence of the non-condensible gas in the bubble cloud prevents any rapid and coherent collapse process. Although local events are frequently observed visually, they rarely produce pressure pulses. When local structures do register pressure pulses, their magnitudes are significantly smaller than the ones produced without air injection. The presence of these shock structures without the observation of large amplitude pressure pulses is consistent with the observations of several previous investigators who performed shock wave experiments with mixtures consisting of a liquid and a non-condensible gas. The experiments and the analysis of Noordzij and van Wijngaarden (1974) demonstrated that shock waves in a bubbly mixture of glycerine and air can result in very large and rapid changes in void fraction. Also, the experiments performed by Kameda and Matsumoto (1995) show that a bubbly mixture of nitrogen gas in silicone oil will produce pressure pulses of only about one atmosphere in amplitude despite a rapid change in ambient pressure of over $100kPa$. Therefore, while it is clear that the air injection does not preclude the formation of the local shock structures, the lack of large pressure pulses is not inconsistent with the presence of these shocks when the bubbles contain large amounts of non-condensible gas.

The re-entrant jet is impeded by the air injection at this high flow rate and does not reach the leading edge of the foil. The air injection disturbs the vapor-liquid interface downstream of the injection point and this disturbance appears to promote the formation of the re-entrant jet. One possible explanation for the cessation of

the jet motion prior to reaching the leading edge is that since the jet formation is hastened by the air injection, the jet does not develop as much momentum as in the case without air injection. Another possible explanation is that the jet is deflected in a direction normal to the foil surface by the injection of air. This deflection could cause the jet to impact the vapor-liquid interface prior to reaching the leading edge. Either of these two scenarios would result in an effect similar to that observed by Kawanami *et al.* (1996) who placed obstacles on the suction side of a static hydrofoil to impede the motion of the re-entrant jet. The presence of these obstacles resulted in a broadband reduction in the cavitation noise spectra of between $5-20dB$ relative to the noise spectra generated without the obstacle.

4.4 Pulsed Air Injection Results

The final experiments performed in this work consisted of a preliminary study of the effectiveness of pulsed air injection. By experimentation it was evident that an optimal injection initiation time and pulse duration existed for a given set of flow parameters. The maximum reduction in the cloud cavitation noise was achieved for a given air pulse duration by initiating the injection just prior to the time at which the downstream edge of the sheet cavity passes the air injection hole. A pulse duration of roughly 30% of the foil oscillation period resulted in the maximum noise reduction, but a reduction in pulse duration below $0.3T$ resulted in an increase in the noise level. Therefore, for all of the pulsed air injection experiments, the valve control unit thumbwheels were set to initiate the air injection pulse as described above and the duration was set to $0.3T$.

The results for the pulsed air injection are plotted in figure 4.5 along with the data for the continuous injection experiments previously depicted in figure 4.1. The normalized air flow rate, q, for the pulsed experiments was taken to be the average q

over the entire oscillation cycle, i.e. the time averaged q over many oscillation cycles. This preliminary data is very promising since the pulsed air injection results in a lower impulse than the impulse attained by injecting the same mass of air spread over the entire oscillation cycle. Pulsed injection also attains the high flow rate limit faster than continuous injection.

Figures 4.6 through 4.9 depict the surface impulse measured for both continuous and pulsed air injection. The continuous injection data is repeated from figure 4.2 except that all 4 data points obtained at $q = 1.6(10)^{-4}$ are plotted individually rather than averaging. It is interesting to note that an initial increase in the impulse at low air flow rates is observed in the pulsed data, especially for transducer #4; this increase is similar to the one observed in the data measured by the floor transducer (see figure 4.1). The same or greater reduction in the unsteady pressure pulse magnitudes can be achieved in all cases by pulsing the same mass of air over only 30% of the foil oscillation period.

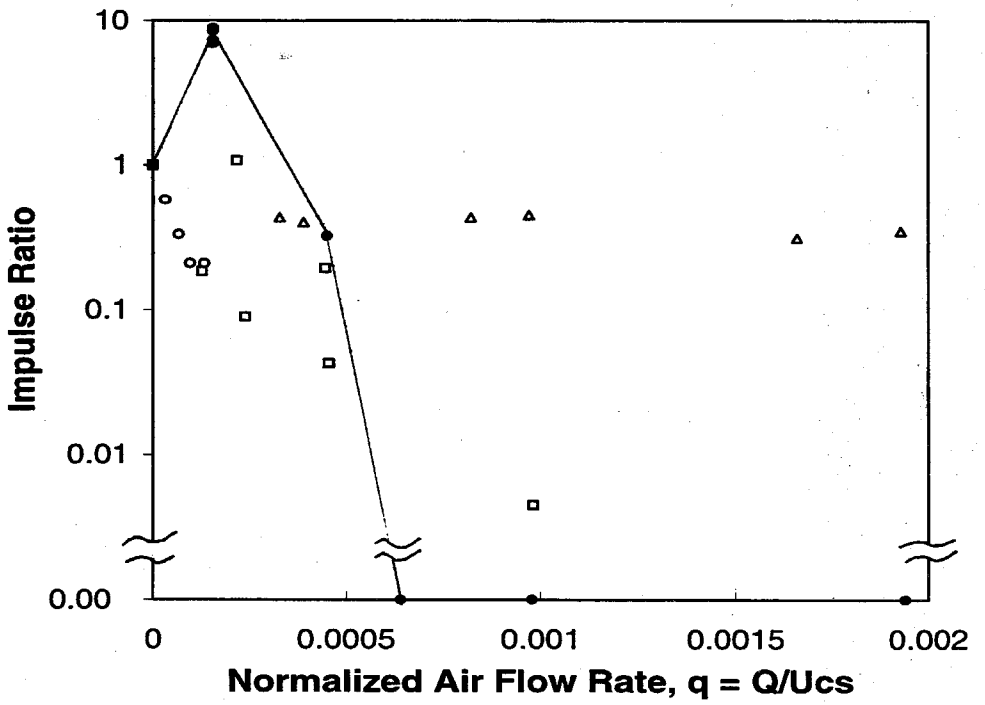

Figure 4.1: Effect of continuous air flow rate on the radiated noise, normalized by the noise without air injection. Data for the NACA 0021 foil experiments at $\sigma = 0.95, k = 0.76, U = 8m/s, TAC = 6-10ppm$ are shown (●), and compared with data from the NACA 64A309 experiments (□), Ukon (1986) at $\sigma = 0.74$, $\alpha = 6.4°$, $U = 8m/s$ (○) and Arndt *et al.* (1993) at $\sigma = 0.9$, $\alpha = 8°$, $U = 15$ and $7.5m/s$ (△).

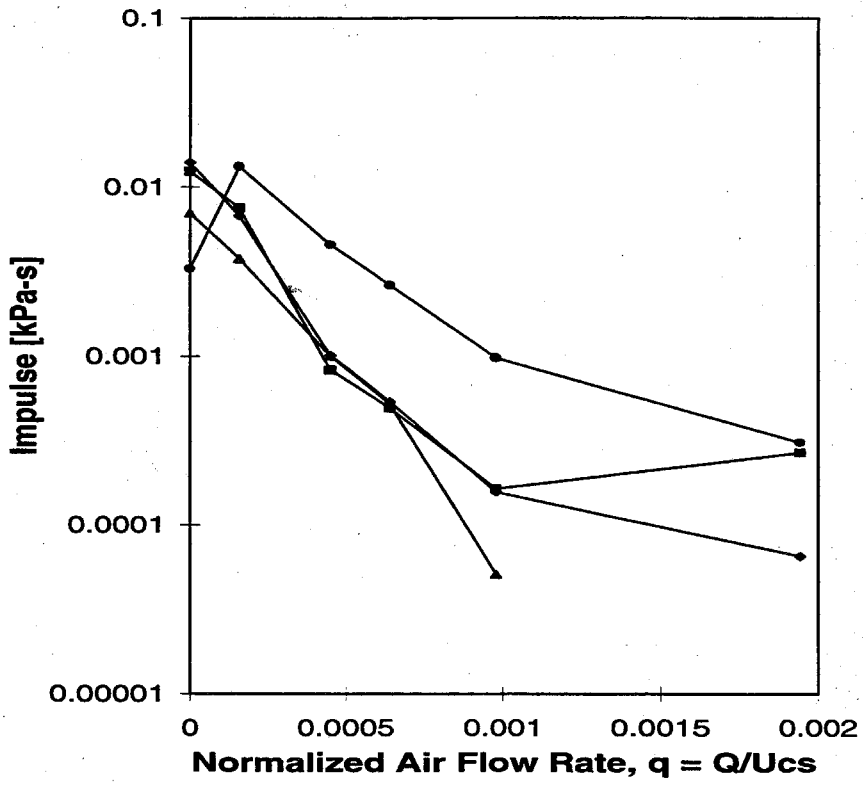

Figure 4.2: Total acoustic impulse measured at 4 different locations on the NACA 0021 foil surface as a function of normalized air flow rate, q. Data for transducer #1 (■), #2 (♦), #3 (▲) and #4 (●); $\sigma = 0.95$, $k = 0.76$, $U = 8m/s$, $TAC = 6 - 10ppm$.

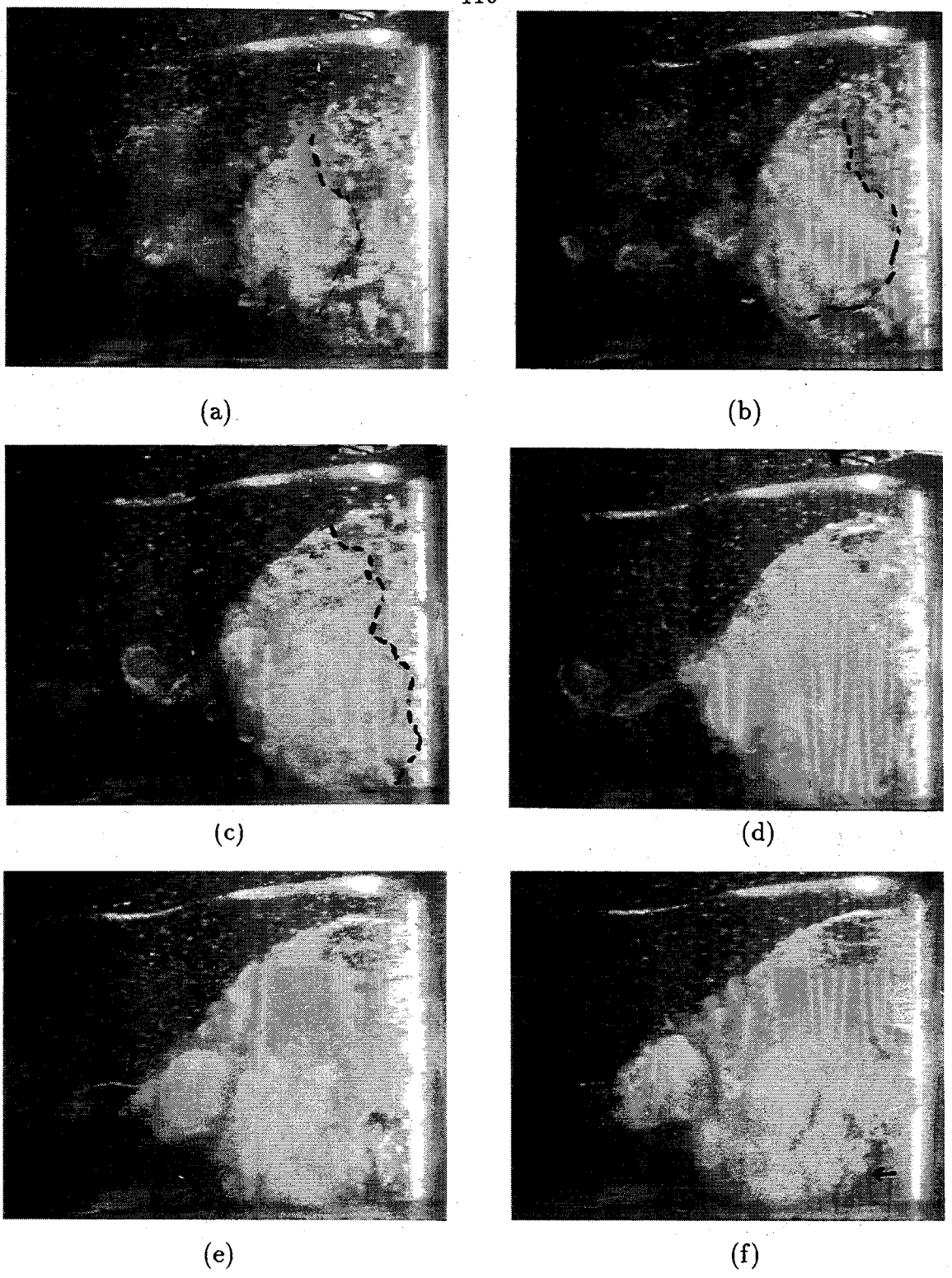

Figure 4.3: Cavitation structures observed during a single oscillation cycle with air injection. Selected frames from a high speed motion picture. Frames are successive but not necessarily consecutive. NACA 0021 foil oscillating at $k = 0.76$, $\sigma = 0.95$, $U = 8m/s$ $\overline{\alpha_f} = 5°$.

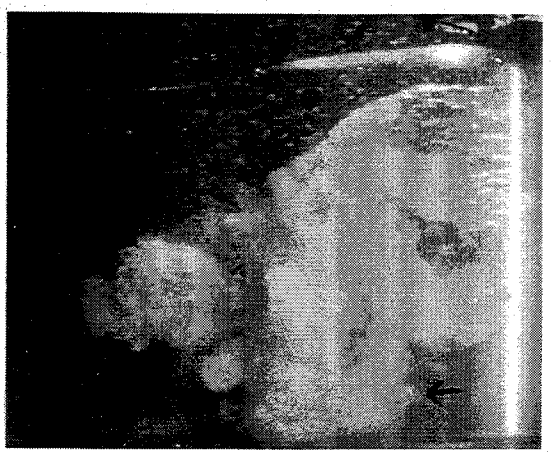

(g)

(h)

(i)

(j)

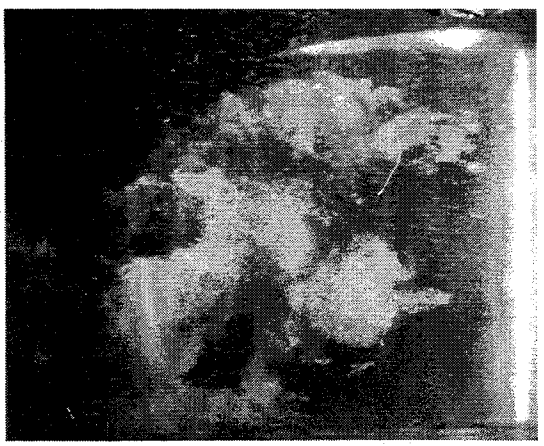

(k)

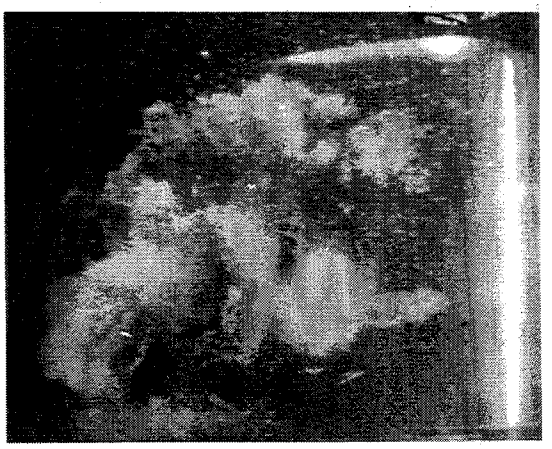

(l)

Cavitation structures observed during a single oscillation cycle with air injection. Selected frames from a high speed motion picture. Frames are successive but not necessarily consecutive. NACA 0021 foil oscillating at $k = 0.76$, $\sigma = 0.95$, $U = 8m/s$ $\overline{\alpha_f} = 5°$.

(m)

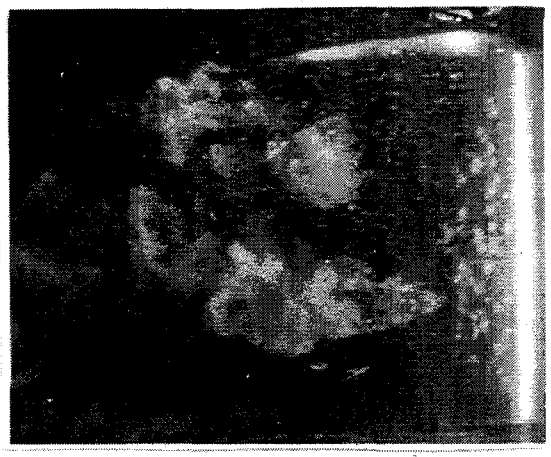

(n)

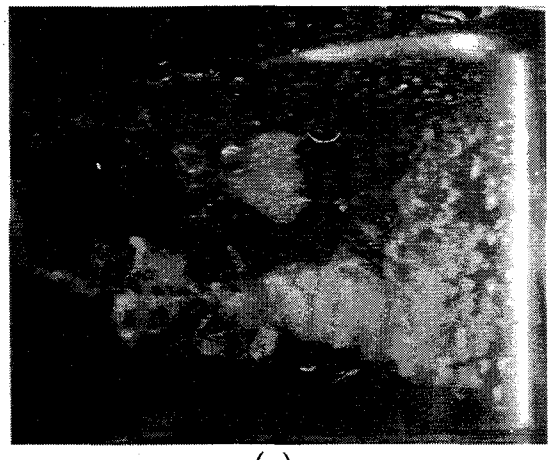

(o)

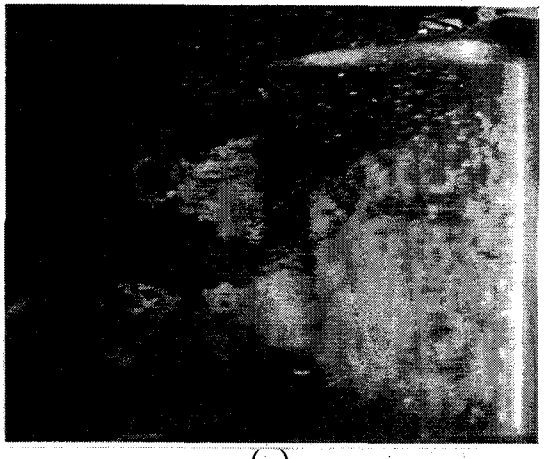

(p)

(q)

(r)

Cavitation structures observed during a single oscillation cycle with air injection. Selected frames from a high speed motion picture. Frames are successive but not necessarily consecutive. NACA 0021 foil oscillating at $k = 0.76$, $\sigma = 0.95$, $U = 8m/s$ $\overline{\alpha_f} = 5°$.

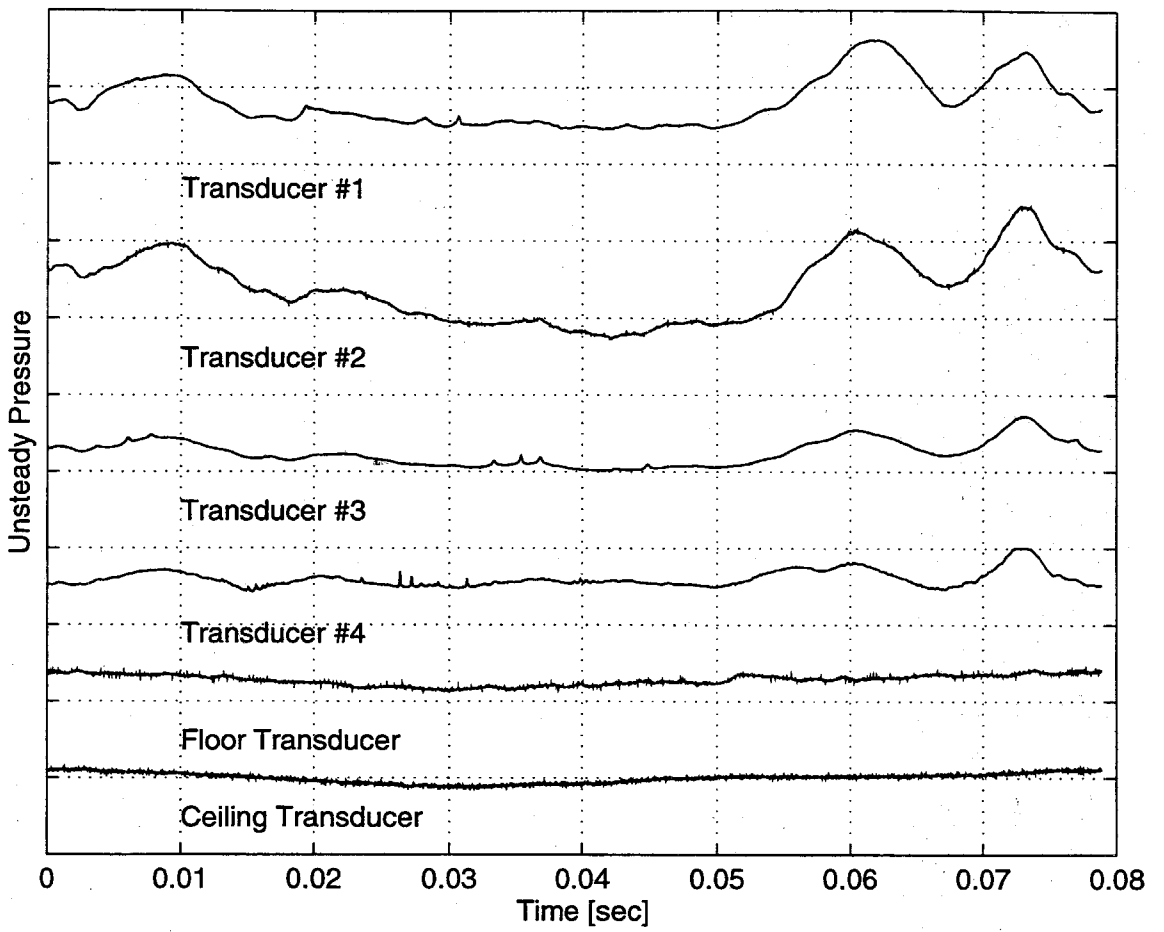

Figure 4.4: Transducer output corresponding to the single oscillation cycle with air injection depicted in figure 4.3. The vertical axis scale is $500kPa$ per division for the foil surface transducers and $50kPa$ per division for the floor and ceiling transducers. Data for $k = 0.76$, $\sigma = 0.95$, $U = 8m/s$, $\overline{\alpha_f} = 5°$.

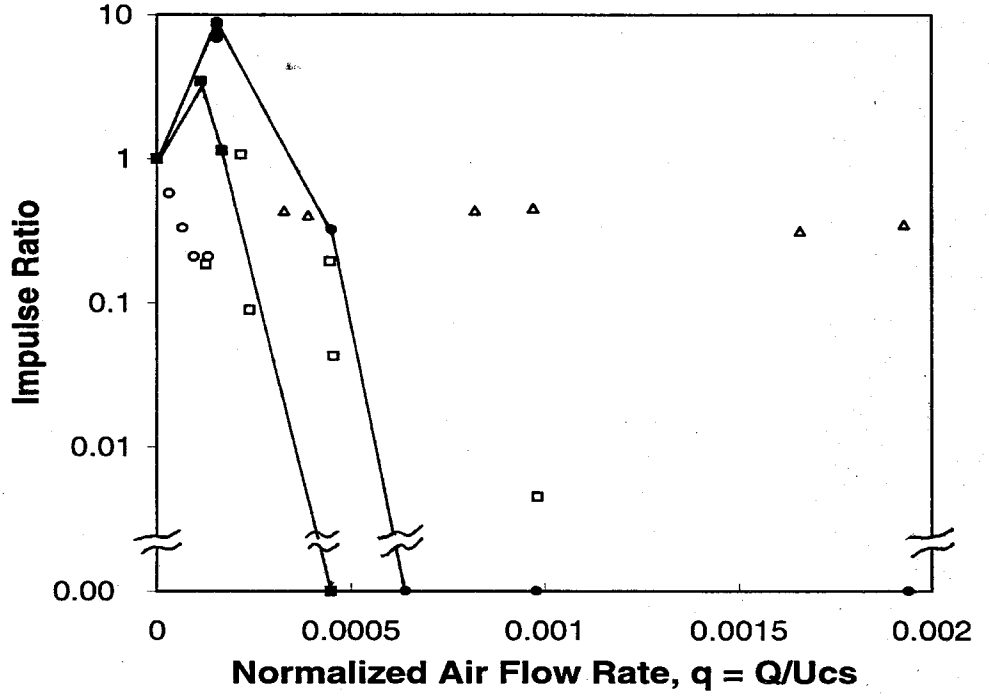

Figure 4.5: Radiated noise, normalized by the noise without air injection, as a function of normalized air flow rate, q, for both pulsed, (■), and continuous, (●), air injection. Data for the NACA 0021 foil experiments at $\sigma = 0.95$, $k = 0.76$, $U = 8m/s$, $TAC = 6 - 10ppm.$ plotted along with data from the NACA 64A309 experiments (□), Ukon (1986) at $\sigma = 0.74$, $\alpha = 6.4°$, $U = 8m/s$ (○) and Arndt *et al.* (1993) at $\sigma = 0.9$, $\alpha = 8°$, $U = 15$ and $7.5m/s$ (△)

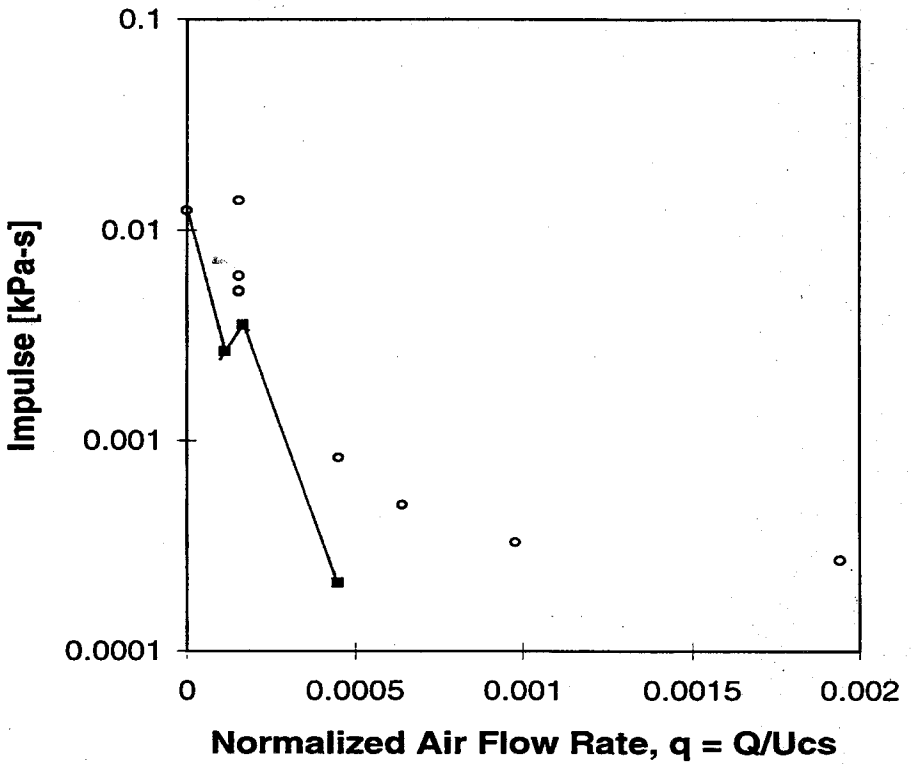

Figure 4.6: Acoustic impulse measured at transducer #1 as a function of normalized flow rate, q. Data for both pulsed, (■), and continuous, (○), air injection on the NACA 0021 foil at $\sigma = 0.95$, $k = 0.76$, $U = 8m/s$, $TAC = 6 - 10ppm$.

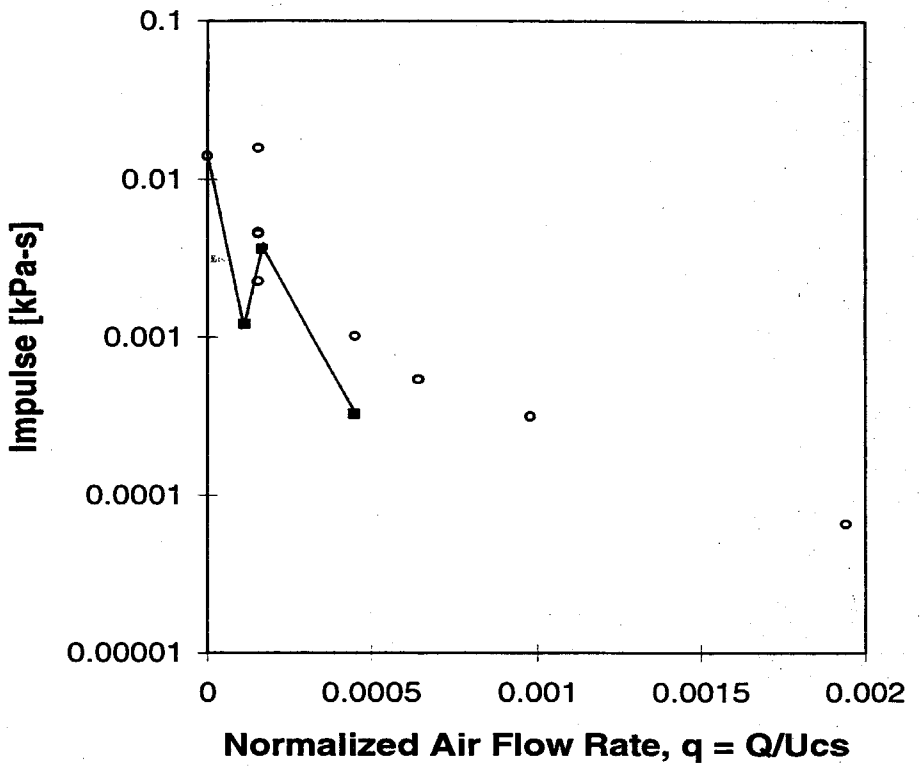

Figure 4.7: Acoustic impulse measured at transducer #2 as a function of normalized flow rate, q. Data for both pulsed, (■), and continuous, (○), air injection on the NACA 0021 foil at $\sigma = 0.95$, $k = 0.76$, $U = 8m/s$, $TAC = 6 - 10ppm$.

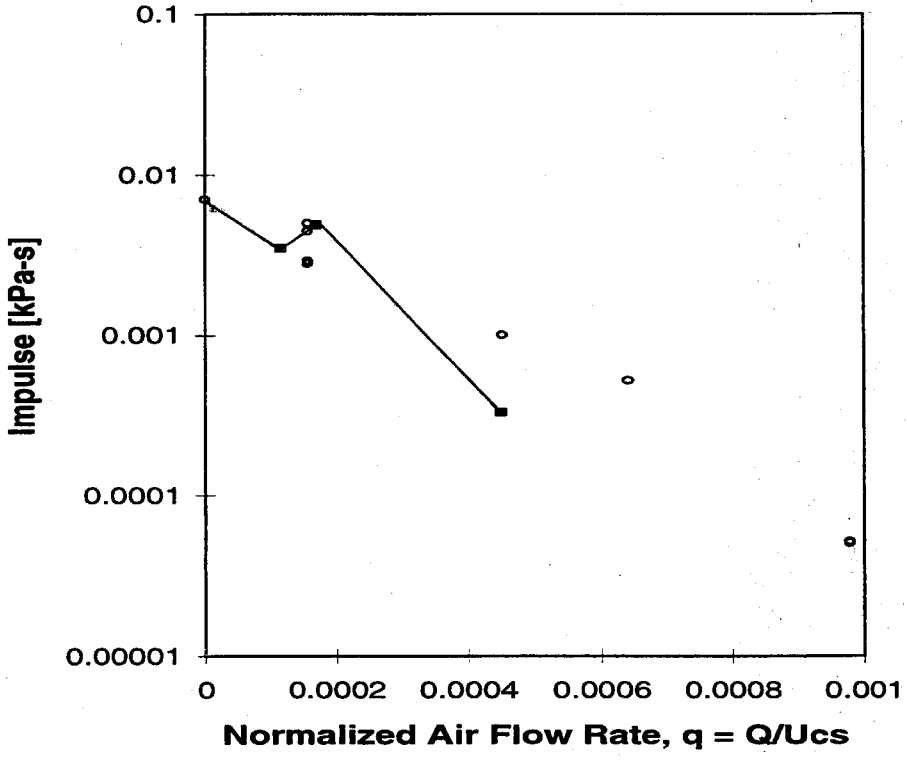

Figure 4.8: Acoustic impulse measured at transducer #3 as a function of normalized flow rate, q. Data for both pulsed, (■), and continuous, (○), air injection on the NACA 0021 foil at $\sigma = 0.95$, $k = 0.76$, $U = 8m/s$, $TAC = 6 - 10ppm$.

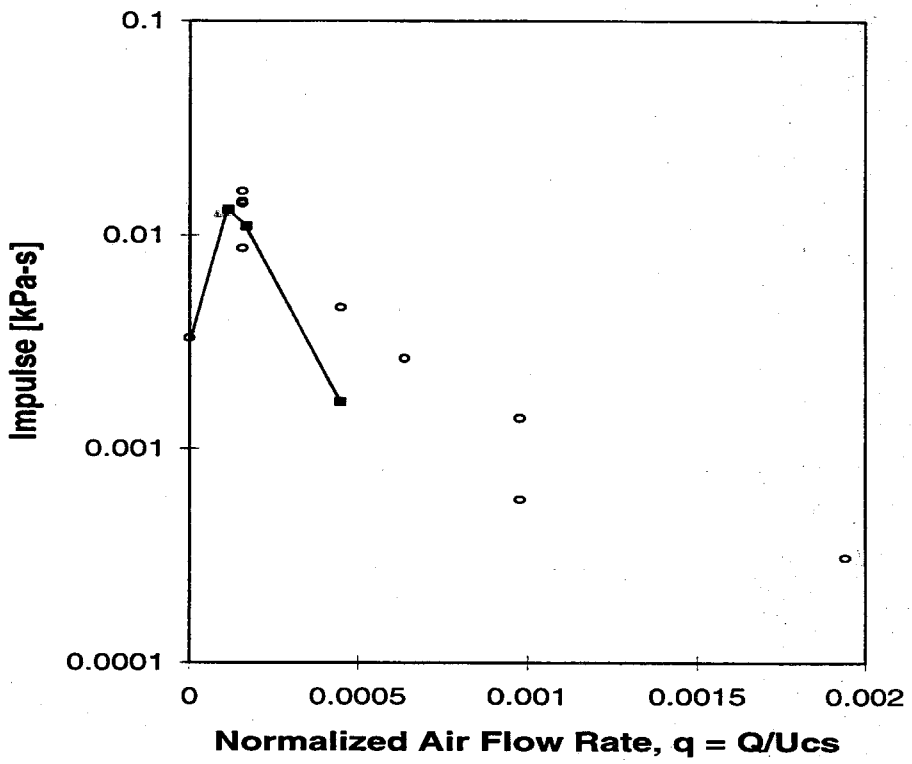

Figure 4.9: Acoustic impulse measured at transducer #4 as a function of normalized flow rate, q. Data for both pulsed, (■), and continuous, (○), air injection on the NACA 0021 foil at $\sigma = 0.95$, $k = 0.76$, $U = 8m/s$, $TAC = 6 - 10ppm$.

Chapter 5 Summary and Discussion: Part 2

In the present experiments, air was injected into the suction side of both the NACA 64A309 hydrofoil and the NACA 0021 hydrofoil over a range of flow rates. The acoustic impulse was measured both at the LTWT test section floor and, in the case of the NACA 0021 foil experiments, at the foil surface. High speed movies of the cloud cavitation structures during air injection were also examined. A preliminary examination of the effectiveness of pulsed air injection in reducing the cloud cavitation noise was also performed.

With air injection, a reduction in the cloud cavitation noise by a factor of two orders of magnitude relative to the noise produced without air injection was achieved. This level of reduction in the acoustic impulse was obtained for measurements made both at the foil surface and at the test section floor. The same maximum level of radiated noise suppression achieved for the continuous air injection experiments was also achieved using air injection pulsed over 30% of the foil oscillation cycle. In all cases, a maximum noise reduction level was approached as the air flow rate increased; air flow rates above a certain level produced no further reduction in the sound level. An initial increase in the acoustic impulse with increasing air flow rate was observed at normalized air flow rates near $q = 0.0002$ during the experiments with the NACA 0021 foil. Conversely, the noise reduction was virtually monotonic with increasing air flow rate in the experiments with the NACA 64A309 hydrofoil.

This cavitation noise suppression is similar to the sound reductions earlier observed by Arndt *et al.* (1993) and Ukon (1986). The data from these previous investigators

also exhibit a critical flow rate level above which no further reduction in cavitation noise was attained. However, the maximum noise reduction achieved in the current experiments is an order of magnitude greater than that achieved by either of these two previous investigations. This difference can be attributed to the fact that the experiments of Arndt *et al.* (1993) and Ukon (1986) were performed with stationary foils with a characteristic noise level much lower than the one produced in the current experiments with an oscillating hydrofoil.

An explanation for the reduction in noise level due to air injection is provided by an analysis of the high speed motion pictures taken during the air injection experiments. The large amount of non-condensible gas present in the cavitation cloud at high air flow rates prevents any rapid or coherent collapse process. Also, the remains of the sheet cavity are fragmented into several bubbly structures that lack the coherence of the clouds observed without air injection. These fragments persist as they are convected downstream into the high pressure stagnation region. Despite the lack of global events, local structures are still observed during air injection, but the magnitude of the local pulses detected by the foil surface transducers is substantially reduced relative to the pulse amplitudes measured without air injection. The injection of air also appears to impede the progress of the re-entrant jet in a manner similar to that observed by Kawanami *et al.* (1996) when obstacles were placed on the suction side of a cavitating hydrofoil.

Finally, the preliminary pulsed air injection experiments were very encouraging. The optimal initiation time corresponded to the moment just prior to the arrival of the downstream edge of the sheet cavity at the injection location. A minimum pulse duration of approximately 30% of the foil oscillation period was established for the NACA 0021 foil; smaller pulse durations led to an increase in the noise level. The same or greater reduction in the unsteady pressure pulse magnitudes was achieved by pulsing the same mass of air which was previously injected continuously throughout

the oscillation cycle. Thus it can be inferred that a significant portion of the air injected continuously has little or no effect on the noise generated by periodic unsteady cavitation, and a larger reduction in the noise level is achieved for a given mass of air by injecting the air over a properly chosen portion of the oscillation cycle.

Conclusions

Large amplitude impulsive pressures were measured during experiments with hydrofoils experiencing cloud cavitation, and these pressure pulses were correlated with the observation of shock waves propagating through the bubbly mixture. The presence of bubbly shock waves in the cloud cavitation structures described in this thesis is indicated by the geometric coherence of the boundaries of these structures and the nearly discrete change in void fraction across these boundaries. Qualitative agreement between these observations and previous bubbly shock wave research also supports this conclusion. The strongest evidence for the existence of shock waves in these structures, however, is the generation of impulsive pressures with amplitudes on the order of tens of atmospheres on the suction surface of the foil. These amplitudes are two orders of magnitude greater than the dynamic pressure of the flow and are generated by the collapse of cavitation bubbles along the shock front.

Two distinct types of bubbly shock wave events were identified. Local pressure pulses were caused by both curved and normal shock waves propagating through the bubbly mixture in the downstream direction. These local pulses were registered by a single transducer and were not repeated at the same location from one foil oscillation cycle to the next. Global pressure pulses were caused by the focusing of a shock wave in the interior of a cloud of cavitation bubbles. The global pulses were detected throughout the flowfield producing substantial radiated noise. The global events were repeatable from cycle to cycle at the same point in the foil oscillation.

Air injection on the suction surface of an oscillating hydrofoil experiencing cloud cavitation resulted in a reduction in the cloud cavitation noise by a factor of two orders of magnitude relative to the noise produced without air injection. Observation

of the high speed motion pictures showed that air injection precludes the rapid or coherent global collapse of the bubble clouds. Local shock structures are still present, but the presence of the non-condensible gas drastically reduces the magnitudes of any resulting pressure pulses.

Bibliography

Arakeri, V.H. and Shanmuganathan, V., "On the evidence for the effect of bubble interference on cavitation noise," *J. Fluid Mech.*, 1985, Vol. 159, pp. 131-150.

Arndt, R. E. A., Ellis, C. R., and Paul, S., "Preliminary investigation of the use of air injection to mitigate cavitation erosion," *Proc. ASME Symp. on Bubble Noise and Cavitation Erosion in Fluid Systems*, 1993, Vol. 176, pp. 105-116.

Avallone, E. A., and Baumeister, T., ed., "Marks' standard handbook for mechanical engineers," *McGraw-Hill*, 1986.

Avellan, F. and Farhat, M. (1989) Shock pressure generated by cavitation vortex collapse. ASME Int. Symp. on Cavitation Noise and Erosion in Fluid Systems, FED-88, 199-125.

Bark, G. and van Berlekom, W.B., "Experimental investigations of cavitation noise," *Proc. 12th ONR Symp. on Naval Hydrodynamics*, 1978, pp. 470–493.

Bark, G., "Developments of distortions in sheet cavitation on hydrofoils," *Proc. ASME Int. Symp. on Jets and Cavities*, 1985, pp. 215–225.

Blake, W. K., "Mechanics of flow-induced sound and vibration," *Academic Press*, 1986.

Blake, W. K., Wolpert, M. J. and Geib, F. E., "Cavitation noise and inception

as influenced by boundary-layer development on a hydrofoil," *J. Fluid Mech.*, 1977, Vol. 80, pp. 617–640.

Brennen, C. E., "Cavitation and bubble dynamics," *Oxford University Press*, 1995.

Brennen, C. E., Reisman, G.E., and Wang, Y.-C., "Shock waves in cloud cavitation," *Proc. 21st ONR Symp. on Naval Hydrodynamics*, 1996.

Ceccio, S.L., "Observations of the dynamics and acoustics of traveling bubble cavitation," Ph.D. thesis, Cal. Inst. of Tech., 1990.

Ceccio, S.L. and Brennen, C.E., "Observations of the dynamics and acoustics of traveling bubble cavitation," *J. Fluid Mech.*, 1991, Vol. 233, pp. 633–660.

Chahine, G.L., Personal communication, 1992.

Chahine, G.L., "Cloud cavitation theory," *Proc. 14th ONR Symp. on Naval Hydrodynamics*, 1982, p. 51.

Chahine, G.L. and Duraiswami, R., "Dynamical interactions in a multibubble cloud," *ASME J. Fluids Eng.*, 1992, Vol. 114, pp. 680-686.

d'Agostino, L. and Brennen, C.E., "On the acoustical dynamics of bubble clouds," *ASME Cavitation and Multiphase Flow Forum*, 1983, pp. 72-75.

d'Agostino, L. and Brennen, C.E., "Acoustical absorption and scattering cross-sections of spherical bubble clouds," *J. Acoust. Soc. of Amer.*, 1988, Vol. 84, No.6, pp. 2126–2134.

d'Agostino, L. and Brennen, C.E., "Linearized dynamics of spherical bubble clouds," *J. Fluid Mech.*, 1989, Vol. 199, pp. 155-176.

de Lange, D.F., de Bruin, G.J. and van Wijngaarden, L., 1994, "On the mechanism of cloud cavitation -experiment and modeling," Proc. 2nd Int. Symp. on Cavitation, Tokyo, Japan, pp. 45-50.

Fitzpatrick, H. M. and Strasberg, M., "Hydrodynamic sources of sound," *Proc. First ONR Symp. on Naval Hydrodynamics*, 1956, pp. 241-280.

Franc, J.P. and Michel, J.M., "Unsteady attached cavitation on an oscillating hydrofoil," *J. Fluid Mech.*, 1988, Vol. 193, pp. 171–189.

Gates, E. M., "The influence of free stream turbulence, free stream nuclei populations, and a drag-reducing polymer on cavitation inception on two axisymmetric bodies," Ph.D. thesis, Cal. Inst. of Tech., 1977.

Hamilton, M.F., Thompson, D.E. and Billet, M.L., "An experimental study of traveling bubble cavitation and noise," *Proc. ASME Int. Symp. on Cavitation Noise*, 1982, pp. 25-33.

Hanson, I., Kedrinskii, V.K. and Mørch, K.A., "On the dynamics of cavity clusters," *J. Appl. Phys.*, 1981, Vol. 15, pp. 1725-1734.

Hart, D.P., "Cavitation and wake structure of unsteady tip vortex flows ," Ph.D. thesis, Cal. Inst. of Tech., 1993.

Hart, D.P., Brennen, C.E. and Acosta, A.J., "Observations of cavitation on a three dimensional oscillating hydrofoil," *ASME Cavitation and Multiphase Flow Forum*, 1990, FED-Vol. 98, pp. 49–52.

Jakobsen, J.K., "On the mechanism of head breakdown in cavitating inducers," *ASME J. Basic Eng.*, 1964, Vol. 86, pp. 291–304.

Kameda, M. and Matsumoto, Y., "Structure of shock waves in a liquid containing gas bubbles," *Proc. IUTAM Symp. on Waves in Liquid/Gas and Liquid/Vapour Two-Phase Systems*, 1995, pp. 117-126.

Kawanami, Y., Kato, H., Yamaguchi, H., Tagaya, Y. and Tanimura, M., "Mechanism and Control of Cloud Cavitation," *Proc. ASME Symp. on Cavitation and Gas-Liquid Flows in Fluid Machinery and Devices*, 1996, FED-Vol. 236, pp. 329-336.

Kubota, A., Kato, H., Yamaguchi, H. and Maeda, M., "Unsteady structure measurement of cloud cavitation on a foil section using conditional sampling," *ASME J. Fluids Eng.*, 1989, Vol. 111, pp. 204–210.

Knapp, R.T., 1955, "Recent investigations of the mechanics of cavitation and cavitation damage," Trans. ASME, Vol. 77, pp. 1045-1054.

Kubota, A., Kato, H., Yamaguchi, H. and Maeda, M., 1989, "Unsteady structure measurement of cloud cavitation on a foil section using conditional sampling," ASME. J. Fluids Eng., Vol. 111, pp. 204-210.

Kubota, A., Kato, H. and Yamaguchi, H., "A new modeling of cavitating flows - a numerical study of unsteady cavitation on a hydrofoil section" *J. Fluid Mech.*, 1992, Vol. 240, pp. 59–96.

Kuhn de Chizelle, Y., Ceccio, S.L., Brennen, C.E. and Gowing, S., "Scaling experiments on the dynamics and acoustics of traveling bubble cavitation,"

Proc. 3rd I.Mech.E. Int. Conf. on Cavitation, Cambridge, England, 1992, pp. 165–170.

Kuhn de Chizelle, Y., Ceccio, S.L., Brennen, C.E. and Shen, Y., "Cavitation scaling experiments with headforms: bubble acoustics," *Proc. 19th Symp. on Naval Hydrodynamics, Seoul, Korea*, 1992, pp. 72–84.

Kuhn de Chizelle, Y., Ceccio, S.L. and Brennen, C.E., "Observations, scaling and modeling of traveling bubble cavitation", *J. Fluid Mech.*, 1995, Vol. 293, pp. 99–126.

Kumar, S., "Some theoretical and experimental studies of cavitation noise," Ph.D. thesis, Cal. Inst. of Tech., 1991.

Kumar, S. and Brennen, C.E., "Non-linear effects in the dynamics of clouds of bubbles," *J. Acoust. Soc. Am.*, 1991, Vol. 89, pp. 707-714.

Kumar, S. and Brennen, C.E., "Harmonic cascading in bubble clouds," *Proc. Int. Symp. on Propulsors and Cavitation, Hamburg*, 1992, pp. 171-179.

Kumar, S. and Brennen, C.E., "A study of pressure pulses generated by traveling bubble cavitation," *J. Fluid Mech.*, 1993a, Vol. 255, pp. 541–564.

Kumar, S. and Brennen, C.E., "Some nonlinear interactive effects in bubbly cavitating clouds," *J. Fluid Mech.*, 1993b, Vol. 253, pp. 565-591.

Le, Q., Franc, J.P. and Michel, J.M., 1993, "Partial cavities: pressure pulse distribution around cavity closure," ASME J. Fluids Eng., Vol. 115, pp. 249-254.

Lush, P.A. and Skipp, S.R., 1986, "High speed cine observations of cavitating flow in a duct," Int. J. Heat Fluid Flow, Vol. 7, No. 4, pp. 283-290.

"MATLAB Reference Guide," *Math Works, Inc.*, 1992.

McKenney, E.A., "A study of tip vortices and cavitation on a propeller in a non-uniform flow field," Ph.D. thesis, Cal. Inst. of Tech., 1995.

McKenney, E.A. and Brennen, C.E., "On the dynamics and acoustics of cloud cavitation on an oscillating hydrofoil," *Proc. ASME Symp. on Cavitation and Gas-Liquid Flows in Fluid Machinery and Devices*, 1994, FED-Vol. 190, pp. 195–202.

Mørch, K.A., "On the collapse of cavity cluster in flow cavitation," *Proc. First Int. Conf. on Cavitation and Inhomogeneities in Underwater Acoustics, Springer Series in Electrophysics*, 1980, Vol. 4, pp. 95-100.

Mørch, K.A., "Cavity cluster dynamics and cavitation erosion," *Proc. ASME Cavitation and Polyphase Flow Forum*, 1981, pp. 1-10.

Mørch, K.A. [1982] Energy considerations on the collapse of cavity cluster. *Appl. Sci. Res.*,, 38, 313.

Morgan, W.B., personal communication, 1995.

Noordzij, L. and van Wijngaarden, L., "Relaxation effects, caused by relative motion, on shock waves in gas-bubble/liquid mixtures," *J. Fluid Mech.*, 1974, Vol. 66, pp. 115-143.

Omta, R., "Oscillations of a cloud of bubbles of small and not so small ampli-

tude," *J. Acoust. Soc. Am.*, 1987, Vol. 82, pp. 1018-1033.

Prosperetti, A., "Bubble-related ambient noise in the ocean," *J. Acoust. Soc. Am.*, 1988, Vol. 84, pp. 1042-1054.

Reisman, G.E., McKenney, E.A. and Brennen, C.E., "Cloud cavitation on an oscillating hydrofoil," *Proc. 20th ONR Symp. on Naval Hydrodynamics*, 1994, pp. 78-89.

Reisman, G.E. and Brennen, C.E., "Pressure pulses generated by cloud cavitation," *Proc. ASME Symp. on Cavitation and Gas-Liquid Flows in Fluid Machinery and Devices*, 1996, FED-Vol. 236, pp. 319-328.

Sharma, S.D., Mani, K. and Arakeri, V.H., "Cavitation noise studies on marine propellers," *J. Sound and Vibration*, 1990, Vol. 138, pp. 255-283.

Shen, Y. and Peterson, F.B., "Unsteady cavitation on an oscillating hydrofoil," *Proc. 12th ONR Symp. on Naval Hydrodynamics*, 1978, pp. 362–384.

Shen, Y. and Peterson, F.B., "The influence of hydrofoil oscillation on boundary layer transition and cavitation noise," *Proc. 13th ONR Symp. on Naval Hydrodynamics*, 1980, pp. 221-241.

Soyama, H., Kato, H. and Oba, R., "Cavitation observations of severely erosive vortex cavitation arising in a centrifugal pump," *Proc. Third I.Mech.E. Int. Conf. on Cavitation*, 1992, pp. 103-110.

Sturtevant, B., and Kulkarny, V. J., "The focusing of weak shock waves," *J. Fluid Mech.*, 1976, Vol. 73, pp. 651-680.

Ukon, Y., "Cavitation characteristics of a finite swept wing and cavitation noise reduction due to air injection," *Proc. of the Int. Symp. on Propeller and Cavitation*, 1986, pp. 383-390.

Van der Meulen, J. H. J., and van Renesse, R. L., "The collapse of bubbles in a flow near a boundary," *Proc. 17th ONR Symp. on Naval Hydrodynamics*, 1989.

van Wijngaarden, L., "On the collective collapse of a large number of gas bubbles in water," *Proc. 11th Int. Conf. Appl. Mech.*, Springer-Verlag, Berlin, 1964, pp. 854-861.

Wade, R.B. and Acosta, A.J., 1966, "Experimental observations on the flow past a plano-convex hydrofoil," ASME J. Basic Eng., Vol. 88, pp. 273-283.

Wang, Y.-C. and Brennen, C.E., "Shock wave development in the collapse of a cloud of bubbles," *ASME Cavitation and Multiphase Flow Forum*, 1994.

Wang, Y.-C. and Brennen, C.E., "The noise generated by the collapse of a cloud of cavitation bubbles," *ASME Symp. on Cavitation and Gas-Liquid Flows in Fluid Machinery and Devices*, 1995, FED-Vol. 226, pp. 17-29.

Zenit, R., personal communication, 1994.

Appendix A In-situ Acoustic Attenuation Measurements

A.1 Apparatus

The dissipation of acoustic energy by the presence of a large number of gas or vapor bubbles in the LTWT test section can result in artificially low measurements of the radiated acoustic pressure in the far field. To monitor the amount of acoustic attenuation during the experiments, a system was created consisting of an ITC 1042 hydrophone used as a transmitter and the floor transducer used as a receiver. This monitoring system is similar to the method used by Blake *et al.* (1977). The hydrophone was mounted in a PVC pipe attached vertically to one of the test section ceiling portholes and the pipe was filled with water. Since the lucite porthole has the same acoustic impedance, ρc, as water, an acoustically transparent transmission path existed between the hydrophone and the floor mounted PCB HS114A21 transducer. The hydrophone was driven by a sinusoidal voltage with an amplitude of approximately $10V$ at a variety of frequencies. The output from the floor transducer was amplified and then passed through two channels of a Krohn-Hite Model 3202 analog filter; the first channel was set to high pass and the second was set to low pass. By using this notch filter to examine the frequency content in the tunnel near the frequency of the input voltage to the hydrophone, an output magnitude could be measured even while the foil was experiencing cloud cavitation. This magnitude was measured using a Tektronix 2213A $60MHz$ oscilloscope.

A variety of input frequencies were used and the results are shown in figure A.1.

The amplitude of the floor transducer output was measured periodically during the air injection experiments with the NACA 0021 foil and the running time of the experiment, t_r, was recorded at the time of the measurement. In figure A.1 this output amplitude is plotted as a function of qt_r, the running time multiplied by the normalized air flow rate, $q = Q/Ucs$. If the acoustic test signal is transmitted at a frequency near the typical resonant frequency of the bubbles present in the test section, one would expect considerable variation in the resulting measurements and it would be difficult to draw meaningful conclusions from the data. For a range of frequencies between 60 and 100 kHz and for typical experimental conditions ($\sigma = 0.95, U = 8m/s$), bubbles with a radius between approximately 10 to 100 μm would be excited (Brennen (1995)). Fortunately, the typical air bubbles present in the tunnel after significant air injection have much larger radii, on the order of $1mm$ and larger. This explains why figure A.1 shows good agreement between the data taken at different frequencies. The data taken at $60kHz$ differs somewhat from the higher frequencies but this is explained by the fact that this frequency is the closest to the natural frequency of the air bubbles observed in the tunnel. After some preliminary runs, only the $102kHz$ input voltage frequency was used since it resulted in the clearest output signal.

A.2 Results

In order to evaluate the acoustic attenuation between the floor and ceiling of the LTWT test section due to the presence of air bubbles, the monitoring system described above was operated during all of the continuous air injection experiments with the NACA 0021 foil. Figure A.2 displays the voltage (peak-to-peak) of the $102kHz$ signal as measured by the floor transducer as a function of qt_r, the running time multiplied by the normalized air flow rate, $q = Q/Ucs$. The inverse of the TAC which was measured at selected points during the experiments is also presented on this figure.

The order of the continuous air injection experiments was as follows. Data was taken at flow rates of $q = 1.6(10)^{-4}$, $6.4(10)^{-4}$ and $9.8(10)^{-4}$, in that order. The beginning of the experiment at each of these flow rates is marked on figure A.2 by the letters A, B and C, respectively. During this time, the TAC increased from an initial value of $6.6ppm$ to a final value of $9.2ppm$. The LTWT was then deaerated to a new initial TAC value of $8.2ppm$. Data was taken at flow rates of $q = 9.8(10)^{-4}$, $4.5(10)^{-4}$, $1.6(10)^{-4}$ and $1.9(10)^{-3}$, and the beginning of each of these experimental runs is marked on figure A.2 by the letters D, E, F and G, respectively. The final value of TAC for this set of experiments was $8.9ppm$. Approximately four acoustic attenuation measurements were made at each flow condition.

For the first set of experiments, the acoustic attenuation increased rapidly and virtually monotonically, but the second set of experiments resulted in a cyclical and less steep variation in the signal magnitude. The cyclical variations evident in the second set of experiments can be attributed to the injection of a large volume of air in a relatively short period of time since these experiments were performed much more quickly than the first set. Unlike the first set of data, the air did not have sufficient time to dissolve during the experiments and the subsequent rapid accumulation of air bubbles in the test section caused a rapid drop in signal amplitude. Between these experiments, a significant amount of air would either separate out or dissolve and a recovery in the signal amplitude would be observed at the beginning of the next run. In both cases, the long term trend in the acoustic attenuation data is represented reasonably well by the plot of the inverse of the TAC.

Despite this correlation between the acoustic attenuation and the inverse of the total air content, it remains uncertain what conclusions, if any, can be applied to the acoustic impulse measurements made using the floor transducer. The transmission path and bubble size and number distribution between the ceiling of the test section and the floor transducer is considerably different from those corresponding to

the transmission path between the cloud cavitation region and the floor transducer. During the experiments, a concentration of air near the top of the test section was observed. While this layer of air would have a severe attenuating effect on the acoustic transmission from the ceiling to the floor, the radiation of noise from the foil surface to the floor transducer would not be affected. The lack of relevance between the results of this appendix and the acoustic impulses measured by the floor transducer is supported by the fact that the trends depicted in figure A.2 were not observed when the 40 acoustic impulses obtained during a single experiment were plotted as a function of running time. Also, as mentioned in chapter 4, the average impulses measured at $q = 1.6(10)^{-4}$ were quite repeatable despite the fact that the TAC varied from 6.6 to 9.1 ppm during these experiments.

Nonetheless, both the TAC and the running time of the experiment have a significant attenuating effect on the amplitudes of acoustic waves transmitted between the ceiling and floor of the test section. This attenuating effect must be taken into consideration when interpreting the results of measurements performed using the ceiling transducer or any similar measurements of noise produced far outside of the cavitating region consisting of the suction side of the foil and the immediate downstream area.

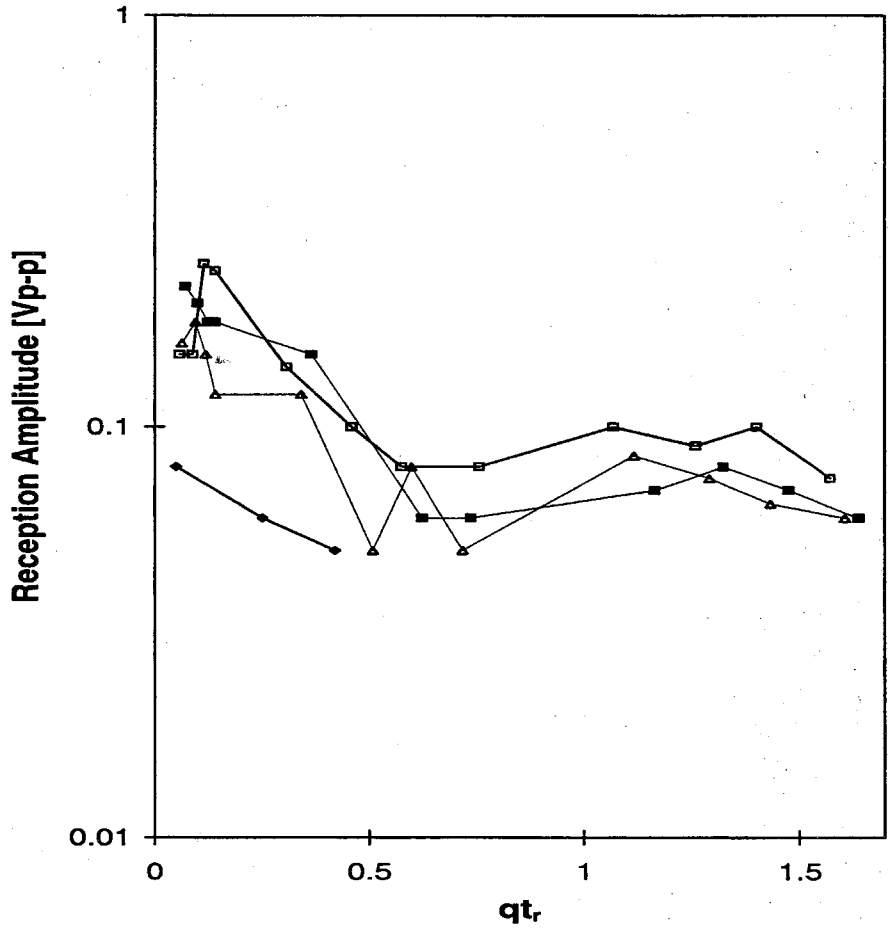

Figure A.1: Amplitude of the reference signal as measured by the floor transducer as a function of running time, t_r, multiplied by the normalized air flow rate,$q = Q/Ucs$ for four different input frequencies: $60kHz$ (♦), $80kHz$ (□), $96kHz$ (△) and $102kHz$ (■).

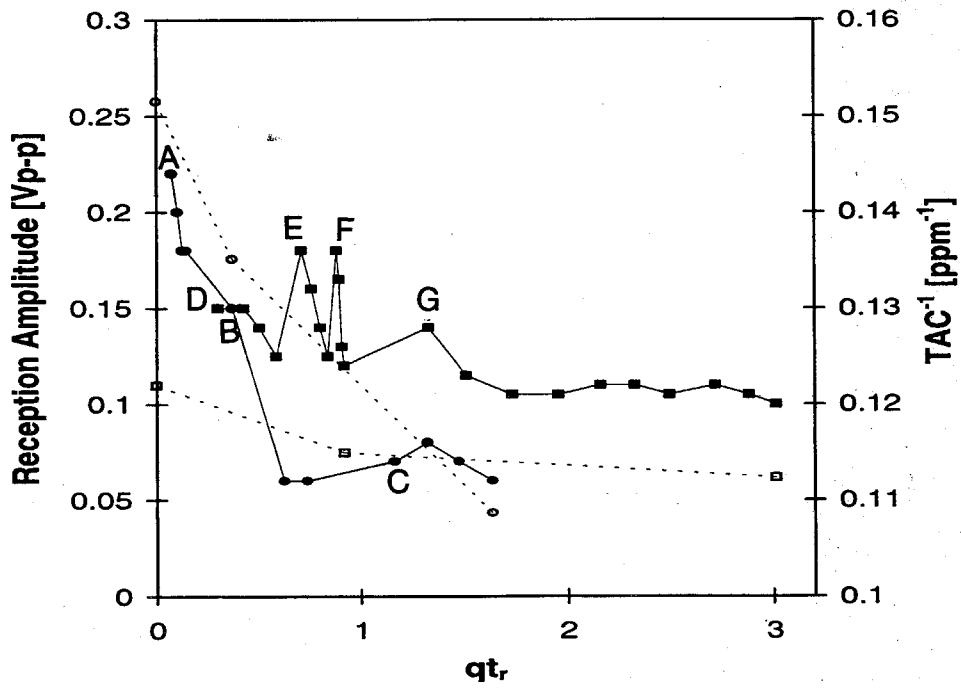

Figure A.2: Amplitude of the reference signal as measured by the floor transducer as a function of running time, t_r, multiplied by the normalized air flow rate,$q = Q/Ucs$ Amplitude data shown for two different sets of experiments(solid lines). The tunnel was deaerated between the two sets. The inverse of the TAC measured between the experiments during each run is also presented (dotted lines).

Appendix B Data Processing Algorithms

```
% M-file newimp2.m, Garrett Reisman 9-10-95
% This M-file calculates the acoustic impulse, I, for a list of input files.

% First the data file is passed through an
% Nth order high-pass Butterworth Filter
% fn is the Nyquist freq. of the sampled data [Hz]
% fc is the cut-off freq. [Hz]
% The lag can be reduced by reducing the order of the Butterworth Filter,
%   but the rolloff will be less steep.

% th is the threshold crossing in volts
% num is the number of peaks above the treshold
% dt is the sampling period


% INPUT PARAMETERS

th = 20; %kPa
dt = 0.000007;
fc = 50; %Hz
fn = (1/0.000007)*0.5;
N = 4;
VtokPa  = 277.79;  % AS113A21 S/N 8120
ampgain = 1;

% GET INPUT FILE

datfil = input('Enter the name of the file containing the data file list />');
setstr(datfil);
outfil = input('Enter the desired name for the output data file />');
setstr(outfil);
%filnum = input('Enter the number of files in this list />');
fid = fopen(datfil,'r');
fid2  = fopen(outfil,'w');

filnum = 0;
fseek(fid,0,1);
enof = ftell(fid);
fseek(fid,0,-1);
while ftell(fid) <  enof,
 filnum = filnum + 1;
 fil = fread(fid,13,'char');
end
filnum

fseek(fid,0,-1);

% MAIN LOOP

for k = 1:filnum,

fil = fread(fid,13,'char');
```

```
fil = fil';
fil = setstr(fil);


eval(['load ',fil])
eval(['x = ',fil(1:8),';'])
eval(['clear ',fil(1:8)])

% TRUNCATE DATA FILE TO INCLUDE ONLY 1 CYCLE

n = 0;
i = 1;
old  = 4;
while n < 1024,
 new = x(i,4);
 if old < 2.5
   dummy = 1;
 elseif new < 2.5
   n = n + 1;
 end
 old = new;
 i = i + 1;
 if i > length(x)
   n = 1024;
   i = length(x);
 end
end

freq = 1/(dt*i);
if i == length(x)
  freq = 99;
end
x = x(1:i,:);


% MAIN PROGRAM

% Mean is subtracted and Volts converted to Pa before filtering

x3 = detrend(x(:,1));
x3 = x3*VtokPa/ampgain;

[b,a] = butter(N,fc/fn,'high');
y = filter(b,a,x3);

% IMPULSE CALCULATION

num = 0;
j = 1;
old = 0;
I = 0;
thnum = max(y)/3;   % This is the threshold used to count the number of peaks
bursts = 0;         % This is the number of integrations
```

```
while j <= i,
 new = y(j);
  if new < th
    j  = j + 1;
    old = new;
  elseif old < th
     bursts = bursts + 1;
     lim1(bursts) = (j/i)*360;
     if thnum < th
        num = num + 1;
     end  %IF
     while new >= th,
      I = I + new;
      if old > thnum   % This if loop checks for a peak as defined by thnum
         dummy = 1;
      elseif new > thnum
         num = num + 1;
      end  %IF
      old = new;
      if j < i         % This if loop increments j and makes sure the end
        j = j + 1;     % of the file has not been reached
        new = y(j);
      elseif j >= i
        j = j + 1;
        new = -1;
      end  %IF
     end   %WHILE
     lim2(bursts) = (j/i)*360;
  end    %IF
end     %WHILE

I = I*dt;

% OUTPUT

fprintf(fid2,'%s %g %g %g',fil(1:8),freq,I,num);
fprintf(fid2,' %g %g',std(y),bursts);
%if bursts ~= 0
%  for j = 1:bursts,
%    fprintf(fid2,' %g %g',lim1(j),lim2(j));
%  end
%end
fprintf(fid2,'\n');


fprintf(1,'%s %g','Calculations are finished for file number ',k)
fprintf(1,'\n');

end  %MAIN FOR LOOP

fclose(fid);
fclose(fid2);
```

```
% M-file spec2.m, Garrett Reisman 1-31-95
% This M-file calculates the average Fourier Spectrum
%   for a list of input files.

% The original file spec.m had an error in the calculation of the frequency
% vector, f, and this program corrects that error.

% dt is the sampling period


% INPUT PARAMETERS


dt = 0.000007;
fn = (1/0.000007)*0.5;
VtokPa  = 353.5773;
fc = 3000;  % [Hz]

%  There is an error here due to the truncation of the data file to one
%  oscillation cycle, instead of N=16384 used in the line below, it is
%  appropriate to use length(x) which will depend on fosc.
%  See the new calculation of f below.

%  f = (1/(16384*dt))*(0:8191);  % (Fs/N)*(0...(N/2)-1)

% GET INPUT FILE

datfil = input('Enter the name of the file containing the data file list />');
setstr(datfil);
outfil = input('Enter the desired 7 character output name without a .  />');
setstr(outfil);

fid = fopen(datfil,'r');
%fid2  = fopen(outfil,'w');

filnum = 0;
fseek(fid,0,1);
enof = ftell(fid);
fseek(fid,0,-1);
while ftell(fid) <  enof,
 filnum = filnum + 1;
 fil = fread(fid,13,'char');
end
filnum

fseek(fid,0,-1);

% MAIN LOOP

A = zeros(filnum,8192);
F = zeros(filnum,8192);
N = zeros(filnum,1);
```

```
for k = 1:filnum,

fil = fread(fid,13,'char');
fil = fil';
fil = setstr(fil);


eval(['load ',fil])
eval(['x = ',fil(1:8),';'])
eval(['clear ',fil(1:8)])

% TRUNCATE DATA FILE TO INCLUDE ONLY 1 CYCLE

n = 0;
i = 1;
old  = 4;
while n < 1024,
 new = x(i,2);
 if old < 2.5
   dummy = 1;
 elseif new < 2.5
   n = n + 1;
 end
 old = new;
 i = i + 1;
end

freq = 1/(dt*i);
x = x(1:i,:);


% MAIN PROGRAM

% Volts converted to Pa before FFT

x3 = x(:,3)*VtokPa;

% ***************  THIS IS NEW ************************
% Time domain signal low-passed filtered at fc = 3 khz to remove
% tunnel resonance effects

%[b,a] = butter(4,fc/fn);
%x3 = filter(b,a,x3);
% plot(x3)

% Hamming window the signal before fft

x3 = x3.*hamming(length(x3));

% **************   END OF NEW STUFF  *******************

for l = 0:((length(x3)/2)-1),
```

```
F(k,l+1) = (1/(length(x3)*dt))*l;  % (Fs/N)*(0...(N/2)-1)
end  % l

x3 = abs(fft(x3));
x3 = x3(1:(length(x3))/2);
N(k) = length(x3);
x3 = x3';


% Normalization a la Kumar (p.94-95)

den = sum(x3)-0.5*(x3(1)+x3(length(x3)));

for l = 1:N(k),
A(k,l) = x3(l)/den;
end  % l


fprintf(1,'%s %g','Calculations are finished for file number ',k)
fprintf(1,'\n');

end  %MAIN FOR LOOP

% This while loop plots and saves some of the individual spectras
% prior to the averaging of the whole bunch

% k = 1;
% while k < filnum,
% loglog(F(k,:),A(k,:))
% xlabel('Frequency [Hz]')
% ylabel('Nondimensional Fourier Magnitude')
% title('Normalized Spectra from a Single Oscillation Cycle')
% eval(['print ',outfil,'.1cycle',k])
% k = k + 5;
% end  % while

f = (1/(2*min(N)*dt))*(0:(min(N)-2));  % (Fs/N)*(0...(N/2)-2
B = zeros(min(N)-1,filnum);

for k = 1:filnum,

tab = zeros(N(k),2);

for l = 1:N(k),
tab(l,1) = F(k,l);
tab(l,2) = A(k,l);
end  % l

B(:,k) = table1(tab,f);

fprintf(1,'%s %g','Calculations are finished for file number ',k)
fprintf(1,'\n');
```

```
end  % k

B = B';

if k == 1
   a = B;
else
   a = mean(B);
end  % if

out = [f' a'];


eval(['save ',outfil,'.spc out -ascii']);

% PLOT GENERATION

loglog(f,a)
ylabel('Average Nondimensional Fourier Magnitude')
xlabel('Frequency [Hz]')
title('Sigma = 1.5 k = 0.7, With Hamming Window')
eval(['print ',outfil,'.plt'])

fclose(fid);

save Ahammss15.mat A
save Fhammss15.mat F
```

```
% M-file shockimp, Garrett Reisman 9-10-95
% This M-file calculates the acoustic impulse, I, for an input file and
% plots it.

% First the data file is passed through an
% Nth order high-pass Butterworth Filter
% fn is the Nyquist freq. of the sampled data [Hz]
% fc is the cut-off freq. [Hz]
% The lag can be reduced by reducing the order of the Butterworth Filter,
%   but the rolloff will be less steep.

% th is the threshold crossing in volts
% num is the number of peaks above the treshold
% dt is the sampling period

%   CHANNEL              DESCRIPTION Analog Filter
%     fc [kHz]

%     1                    Sensor #1 from L.E 45
%     2                  Sensor #2 from L.E. 45
%     3                    Sensor #3 from L.E. 45
%     4                    Sensor #4 from L.E. 45
%     5                    PCB in Floor  S/N 8120 30
%     6 Zero Pulse (Max. alpha now) NA
%     7 Shaft Encoder NA
%     8 PCB in Cieling S/N 8119 NA


% INPUT PARAMETERS
% Trig. Point = 00000

dt = 0.00001;
fn = (1/dt)*0.5;
th = 20; %kPa - Threshold for floor and porthole impulse measurement
th2 = 200; %kPa - Threshold for foil mounted impulse measurement
fc = 50; %Hz - floor and porthole data filtering
fc2 = 600; %Hz - foil mounted data filtering
N = 4;

VtokPa1 = 389.5;
VtokPa2 = 420.4;
VtokPa3 = 156;
VtokPa4 = 233.9;
VtokPa5 = 277.79;
VtokPa8 = 284.33;

gain1 = 1;
gain2 = 1;
gain3 = 1;
gain4 = 1;
gain5 = 10;
gain6 = 1;
```

```
gain7 = 1;
gain8 = 49.107;

% GET INPUT FILE

datfil = input('Enter the name of the file containing the data file list />');
setstr(datfil);
outfil = input('Enter the desired name for the output data file />');
setstr(outfil);
fid = fopen(datfil,'r');
fid2  = fopen(outfil,'w');

filnum = 0;
fseek(fid,0,1);
enof = ftell(fid);
fseek(fid,0,-1);
while ftell(fid) <  enof,
 filnum = filnum + 1;
 fil = fread(fid,13,'char');
end
filnum

fseek(fid,0,-1);

% MAIN LOOP

for k = 1:filnum,

fil = fread(fid,13,'char');
fil = fil';
fil = setstr(fil);


eval(['load ',fil])
eval(['x = ',fil(1:8),';'])
eval(['clear ',fil(1:8)])

% TRUNCATE DATA FILE TO INCLUDE ONLY 1 CYCLE

n = 0;
i = 1;
old  = 4;
while n < 1024,
 new = x(i,7);
 if old < 2.5
   dummy = 1;
 elseif new < 2.5
   n = n + 1;
 end
 old = new;
 i = i + 1;
 if i > length(x)
   n = 1024;
```

```
   i = length(x);
 end
end

numcycles = 1;
n2 = 0;
if i < length(x)/2
 numcycles = 2;
 while n2 < 1024,
   new = x(i,7);
   if old < 2.5
     dummy = 1;
   elseif new < 2.5
     n2 = n2 + 1;
   end
   old = new;
   i = i + 1;
 end % while
end % if

freq = 1/(dt*i/numcycles);
if i == length(x)
  freq = 999;
end
x = x(1:i,:);
freq

% MAIN PROGRAM

%  Mean is subtracted, amp gain is accounted for,
%  and Volts converted to kPa

x8 = (x(:,8)-mean(x(:,8)))*VtokPa8/gain8;
x5 = (x(:,5)-mean(x(:,5)))*VtokPa5/gain5;
x4 = (x(:,4)-mean(x(:,4)))*VtokPa4/gain4;
x3 = (x(:,3)-mean(x(:,3)))*VtokPa3/gain3;
x2 = (x(:,2)-mean(x(:,2)))*VtokPa2/gain2;
x1 = (x(:,1)-mean(x(:,1)))*VtokPa1/gain1;

t = (0:length(x1)-1)*dt;

% Recessed Transducers Low-pass filtered at 20 kHz
% to remove resonance effects

[b,a] = butter(4,20000/fn);
x1 = filter(b,a,x1);
x2 = filter(b,a,x2);
x3 = filter(b,a,x3);
x4 = filter(b,a,x4);

% Data high pass filtered at fc and fc2 to prepare for impulse algorithm

[b,a] = butter(N,fc/fn,'high');
```

```
[c,d] = butter(N,fc2/fn,'high');
y1 = filter(c,d,x1);
y2 = filter(c,d,x2);
y3 = filter(c,d,x3);
y4 = filter(c,d,x4);
y5 = filter(b,a,x5);
y8 = filter(b,a,x8);

% Plot Data

% Arbitrary DC offsets added to separate data
% Channels 5,8 multiplied x10 to make them visible on the same scale

figure(1)

y8p = y8*10;
y5offset =  max(y8p) - min(y5);
y5p = y5*10 + y5offset;
y4offset =  max(y5p) - min(y4);
y4p = y4 + y4offset;
y3offset =  max(y4p) - min(y3);
y3p = y3 + y3offset;
y2offset =  max(y3p) - min(y2);
y2p = y2 + y2offset;
y1offset =  max(y2p) - min(y1);
y1p = y1 + y1offset;

plot(t,y1p,t,y2p,t,y3p,t,y4p,t,y5p,t,y8p)
xlabel('Time [sec]')
ylabel('Unsteady Pressure [kPa]')
axis([0 max(t) min(y8p) max(y1p)])

line([0 max(t)],[mean(y1p)+th2 mean(y1p)+th2])
line([0 max(t)],[mean(y2p)+th2 mean(y2p)+th2])
line([0 max(t)],[mean(y3p)+th2 mean(y3p)+th2])
line([0 max(t)],[mean(y4p)+th2 mean(y4p)+th2])
line([0 max(t)],[mean(y5p)+10*th mean(y5p)+10*th])
line([0 max(t)],[mean(y8p)+10*th mean(y8p)+10*th])

grid

%figure(2)

%x8p = x8*10;
%x5p = x5*10 + max(x8p) - min(x5);
%x4p = x4 + max(x5p) - min(x4);
%x3p = x3 + max(x4p) - min(x3);
%x2p = x2 + max(x3p) - min(x2);
%x1p = x1 + max(x2p) - min(x1);

%plot(t,x1p,t,x2p,t,x3p,t,x4p,t,x5p,t,x8p)
%xlabel('Time [sec]')
%ylabel('Unsteady Pressure [kPa]')
```

```
%axis([0 max(t) min(x8p) max(x1p)])
%grid

figure(1)
hold

% IMPULSE CALCULATION

% PROMPT USER FOR GLOBAL SHOCK WINDOW

t1 = input('Enter the starting time of the global shock window/>');
t2 = input('Enter the end time of the global shock window/>');
t1 = t1*i*dt;
t2 = t2*i*dt;
j1 = t1/dt;
j2 = t2/dt;

% Channel #1

num = 0;
j = 1;
old = 0;
I = 0;
thnum = max(y1)/3;   % This is the threshold used to count the number of peaks
bursts = 0;          % This is the number of integrations

while j <= i,
 new = y1(j);
  if new < th2
    j  = j + 1;
    old = new;
  elseif old < th2
    if (j >= j1) & (j <= j2)       % IF #2
     j = j + 1;
     old = new;
    else
     bursts = bursts + 1;
     lim1(bursts) = (j/i)*360;
     if thnum < th2
        num = num + 1;
     end  %IF
     while new >= th2,
      I = I + new;
      plot(j*dt,new+y1offset,'o')
      if old > thnum   % This if loop checks for a peak as defined by thnum
         dummy = 1;
      elseif new > thnum
         num = num + 1;
      end  %IF
      old = new;
      if j < i         % This if loop increments j and makes sure the end
        j = j + 1;     % of the file has not been reached
        new = y1(j);
```

```
      elseif j >= i
        j = j + 1;
        new = -1;
      end  %IF
     end   %WHILE
     lim2(bursts) = (j/i)*360;
    end % IF #2
  else
    j  = j + 1;
    old = new;
  end    %IF
end     %WHILE

I1 = I*dt;
num1 = num;
bursts1 = bursts;
lim11 = lim1;
lim21 = lim2;


% Channel #2

num = 0;
j = 1;
old = 0;
I = 0;
thnum = max(y2)/3;   % This is the threshold used to count the number of peaks
bursts = 0;          % This is the number of integrations

while j <= i,
 new = y2(j);
  if new < th2
    j  = j + 1;
    old = new;
  elseif old < th2
    if (j >= j1) & (j <= j2)       % IF #2
     j  = j + 1;
     old = new;
    else
     bursts = bursts + 1;
     lim1(bursts) = (j/i)*360;
     if thnum < th2
        num = num + 1;
     end  %IF
     while new >= th2,
      I = I + new;
      plot(j*dt,new+y2offset,'o')
      if old > thnum   % This if loop checks for a peak as defined by thnum
         dummy = 1;
      elseif new > thnum
         num = num + 1;
      end  %IF
      old = new;
```

```
      if j < i          % This if loop increments j and makes sure the end
        j = j + 1;      % of the file has not been reached
        new = y2(j);
      elseif j >= i
        j = j + 1;
        new = -1;
      end  %IF
     end   %WHILE
     lim2(bursts) = (j/i)*360;
    end   %IF #2
  else
    j  = j + 1;
    old = new;
  end    %IF
end     %WHILE

I2 = I*dt;
num2 = num;
bursts2 = bursts;
lim12 = lim1;
lim22 = lim2;


% Channel #3

num = 0;
j = 1;
old = 0;
I = 0;
thnum = max(y3)/3;   % This is the threshold used to count the number of peaks
bursts = 0;          % This is the number of integrations

while j <= i,
 new = y3(j);
  if new < th2
    j  = j + 1;
    old = new;
  elseif old < th2
    if (j >= j1) & (j <= j2)       % IF #2
     j  = j + 1;
     old = new;
    else
     bursts = bursts + 1;
     lim1(bursts) = (j/i)*360;
     if thnum < th2
        num = num + 1;
     end  %IF
     while new >= th2,
      I = I + new;
      plot(j*dt,new+y3offset,'o')
      if old > thnum   % This if loop checks for a peak as defined by thnum
         dummy = 1;
      elseif new > thnum
```

```
        num = num + 1;
      end  %IF
      old = new;
      if j < i          % This if loop increments j and makes sure the end
        j = j + 1;      % of the file has not been reached
        new = y3(j);
      elseif j >= i
        j = j + 1;
        new = -1;
      end  %IF
     end   %WHILE
     lim2(bursts) = (j/i)*360;
    end   % IF #2
  else
    j  = j + 1;
    old = new;
  end    %IF
end     %WHILE

I3 = I*dt;
num3 = num;
bursts3 = bursts;
lim13 = lim1;
lim23 = lim2;

% Channel #4

num = 0;
j = 1;
old = 0;
I = 0;
thnum = max(y4)/3;   % This is the threshold used to count the number of peaks
bursts = 0;          % This is the number of integrations

while j <= i,
 new = y4(j);
  if new < th2
    j  = j + 1;
    old = new;
  elseif old < th2
    if (j >= j1) & (j <= j2)       % IF #2
     j  = j + 1;
     old = new;
    else
     bursts = bursts + 1;
     lim1(bursts) = (j/i)*360;
     if thnum < th2
        num = num + 1;
     end  %IF
     while new >= th2,
      I = I + new;
      plot(j*dt,new+y4offset,'o')
      if old > thnum   % This if loop checks for a peak as defined by thnum
```

```
        dummy = 1;
      elseif new > thnum
        num = num + 1;
      end  %IF
      old = new;
      if j < i          % This if loop increments j and makes sure the end
        j = j + 1;      % of the file has not been reached
        new = y4(j);
      elseif j >= i
        j = j + 1;
        new = -1;
      end  %IF
     end   %WHILE
     lim2(bursts) = (j/i)*360;
    end   % IF #2
  else
    j  = j + 1;
    old = new;
  end    %IF
end     %WHILE

I4 = I*dt;
num4 = num;
bursts4 = bursts;
lim14 = lim1;
lim24 = lim2;

% Channel #5

num = 0;
j = 1;
old = 0;
I = 0;
thnum = max(y5)/3;   % This is the threshold used to count the number of peaks
bursts = 0;          % This is the number of integrations

while j <= i,
 new = y5(j);
  if new < th
    j  = j + 1;
    old = new;
  elseif old < th
    if (j >= j1) & (j <= j2)       % IF #2
     j  = j + 1;
     old = new;
    else
     bursts = bursts + 1;
     lim1(bursts) = (j/i)*360;
     if thnum < th
        num = num + 1;
     end  %IF
     while new >= th,
      I = I + new;
```

```
      plot(j*dt,new+y5offset,'o')
      if old > thnum   % This if loop checks for a peak as defined by thnum
         dummy = 1;
      elseif new > thnum
         num = num + 1;
      end  %IF
      old = new;
      if j < i         % This if loop increments j and makes sure the end
        j = j + 1;     % of the file has not been reached
        new = y5(j);
      elseif j >= i
        j = j + 1;
        new = -1;
      end  %IF
     end   %WHILE
     lim2(bursts) = (j/i)*360;
    end   %IF #2
  else
    j  = j + 1;
    old = new;
  end    %IF
end     %WHILE

I5 = I*dt;
num5 = num;
bursts5 = bursts;
lim15 = lim1;
lim25 = lim2;

Ip = [I1 I2 I3 I4 I5]
nump = [num1 num2 num3 num4 num5]
burstsp = [bursts1 bursts2 bursts3 bursts4 bursts5]
winstart = t1/(i*dt)
winend = t2/(i*dt)

pause(1/2)
hold

% OUTPUT

fprintf(fid2,'%s %g %g %g %g %g %g',fil(1:8),freq,I1,I2,I3,I4,I5);
fprintf(fid2,' %g %g %g %g %g',num1,num2,num3,num4,num5);
fprintf(fid2,' %g %g %g %g %g',bursts1,bursts2,bursts3,bursts4,bursts5);
fprintf(fid2,' %g %g',winstart,winend);
%if bursts ~= 0
%  for j = 1:bursts,
%    fprintf(fid2,' %g %g',lim1(j),lim2(j));
%  end
%end
fprintf(fid2,'\n');


fprintf(1,'%s %g','Calculations are finished for file number ',k)
```

```
fprintf(1,'\n');

end  %MAIN FOR LOOP

fclose(fid);
fclose(fid2);
```